T H E U N I V E R S I T Y O F T U L S A

THE GRADUATE SCHOOL

EXPERIMENTS, CFD SIMULATION AND MODELING OF OIL VISCOSITY AND EMULSION EFFECTS ON ESP PERFORMANCE

by
Hattan M. Banjar

A dissertation submitted in partial fulfillment of

the requirements for the degree of Doctor of Philosophy

in the Discipline of Petroleum Engineering

The Graduate School

The University of Tulsa

2018

T H E U N I V E R S I T Y O F T U L S A

THE GRADUATE SCHOOL

EXPERIMENTS, CFD SIMULATION AND MODELING OF OIL VISCOSITY AND EMULSION EFFECTS ON ESP PERFORMANCE

by
Hattan M. Banjar

A DISSERTATION

APPROVED FOR THE DISCIPLINE OF

PETROLEUM ENGINEERING

By Dissertation Committee

Holden Zhang, Chair
Mauricio Prado
Siamack Shirazi
Ruben Cuamatzi

ABSTRACT

Hattan M. Banjar (Doctor of Philosophy in Petroleum Engineering)

Experiments, CFD Simulation and Modeling of Oil Viscosity and Emulsion Effects on ESP Performance

Directed by Dr. Holden Zhang

149 pp., Chapter 5: Conclusions and Recommendations

(257 words)

Oil-water emulsion effects on a seven-stage electric submersible pump (ESP) performance is studied experimentally and numerically with Computational Fluid Dynamics (CFD) simulation. A mechanistic model for ESP head prediction is developed based on physics. Emulsion rheology inside the ESP is also studied and modeled. At different oil-water fractions, rotational speeds, temperatures the performance of the third stage was measured. Density and mass flowrate were monitored using the mass flowmeter, while the emulsion effective viscosity was derived from the pipe viscometer (PV) measurement.

CFD simulations were carried out with estimated droplet size of the dispersed phase for oil-water flows, and the results were compared with the experiments. Due to the extended use of the ESP, a higher wall roughness was used. Results show a considerable difference compared to the experiment. The difference may be partially due to neglecting leakage losses in CFD simulations. The solver takes the two phases as dispersion instead of emulsion so that the emulsion rheological behavior is not reflected. Therefore, a new liquid mixture is defined based on the combination of oil and water fractions and properties.

The mechanistic model is based on Euler's centrifugal pump equations and includes all possible losses. The model predictions agree with the experimental results at high rotation speeds but need to be improved for low rotation speeds. Emulsion rheology was modeled by considering the droplet size, turbulence, shear and stage number effects with the correspondent dimensionless numbers. Results showed a good match to the experiments, but more data are required to further validate the generality of the model.

ACKNOWLEDGEMENTS

I would like to thank Saudi Aramco for sponsoring me and giving me the honor to pursue PhD degree. I thank the Tulsa University Artificial Lift Projects (TUALP) members for their support of this project. I am very thankful to Dr. Zhang for being my advisor, for providing limitless support, and for always being available to answer inquiries or to discuss issues. I am also grateful to Dr. Prado, Dr. Shirazi, and Dr. Cuamatzi for serving on my dissertation committee.

I thank Mr. Bryan Sams for helping me run experiments and Ms. Donna Trankley for offering great administrative assistance. I would also like to thank Dr. Xia Zhenyan who helped me at the early stages of the project. I extend special thanks to my colleagues: Jianjun Zhu, Fahad Al-Mudairis, Haiwen Zhu and Daniel Croce; I enjoyed discussing technical matters with all of you and I benefited a lot.

I would like to dedicate this work to my parents, Mohammed Banjar and Baiqam Fathi; my lovely wife, Taghreed Ba Wazir, and my brother and sisters. They always give me the support and always pray for me. Special dedication to my children: Qusai, Yamin, and Jumanah. You are priceless gifts from God. My life is brightened because of you all and you always bring joy to my heart.

TABLE OF CONTENTS

LIST OF FIGURES

LIST OF TABLES

INTRODUCTION

Electric submersible pumps (ESPs) are more suitable for high flowrates compared to other artificial lift methods. They are mainly used to overcome the pressure losses between the downhole and the wellhead or even the processing facilities. ESPs are not the best choice for heavy oil reservoirs due to the high oil viscosity. A well may flow naturally for a certain time before an ESP is installed. When water is produced with oil, the effective viscosity of the produced water-in-oil emulsion can rise much higher than that of the single phase oil.

An ESP is installed downhole just below the tubing using a workover rig. A drilling rig may be used for the installation if the ESP is used from the beginning. Hence, replacing the pump is not an easy decision. An accurate prediction of the ESP performance is very important in the design stage. If the performance is over-predicted or under-predicted, then the ESP may not run around the Best Efficiency Point (BEP), and the operation will not be optimized.

Performance of an ESP is affected by different factors, such as the rotational speed, the pump geometry, flowrates and fluid physical properties including viscosity, density and interfacial tension in case of more than one phase exists. In this study, the effects of oil viscosity and oil-water emulsion rheology will be investigated.

Chapter 1 presents a literature review on the topic of this study. Chapter 2 describes the facility on which the experiments are conducted, the fluid properties used in the tests, explanation of the experimental matrix and experimental results. In Chapter 3, CFD simulation setup and simulation results are discussed. In Chapter 4, development of the mechanistic model and

comparison with the experiments are presented. Lastly, in Chapter 5, conclusions and recommendations are given.

CHAPTER 1

LITERATURE REVIEW

Many studies have been conducted on the ESP performance under different flow conditions. Some of these studies focus on the effect of gas existence with oil or water. The selected studies related to viscosity effect are discussed in this chapter. Since oil-water emulsion is the main focus of this study, literature review related to emulsion rheology is also discussed.

1.1 Hydraulic Institute (1955) and Turzo (2000)

Hydraulic Institute (HI) method is the most widely used empirical correlation to correct ESPs performance with viscous flow. It is based on large data sets obtained on a conventional ESP with petroleum fluids at different viscosities. It uses the water performance as the base which is always available from the manufacturer. Using the produced charts, correction factors can be found for capacity, head and efficiency for four flowrate values which are 60%, 80%, 100% and 120% of q_{water} at the BEP. Then, the performance parameters for the viscous fluid can be calculated as follows:

$$q_{vis} = C_q q_{water} \tag{1.1}$$

$$H_{vis} = C_H H_{water} \tag{1.2}$$

and $$\eta_{vis} = C_\eta \eta_{water} \tag{1.3}$$

Later, Turzo et al. (2000) digitized the HI curves so that a set of equations can be used instead of using the HI charts for computer programing. Details on Turzo's procedure to calculate the ESP viscous performance is explained in Solano (2009) thesis.

1.2 Stepanoff (1949)

Stepanoff (1949) conducted experiments with different fluids from water viscosity to 2020 cSt oil, using several ESPs. He found that the head decreases as result of viscosity increase, in such a way that the specific speed at the BEP remains constant:

$$N_s = \frac{\sqrt{q_{bep}^{water}}}{\left(H_{bep}^{water}\right)^{0.75}} = \frac{\sqrt{q_{bep}^{vis}}}{\left(H_{bep}^{vis}\right)^{0.75}} \quad . \tag{1.4}$$

In another form,

$$\frac{q_{bep}^{vis}}{q_{bep}^{water}} = \left(\frac{H_{bep}^{vis}}{H_{bep}^{water}}\right)^{1.5} . \tag{1.5}$$

Therefore, only one correction factor (capacity or head) is needed from his chart, and the other correction factors are dependent. In order to obtain the correction factor, water head must be known at the BEP as well as the viscous oil flowrate at the BEP. Then, the dimensionless Stepanoff Reynolds number can be calculated:

$$Re_{Stepanoff} = 6.0345 \frac{N q_{bep}^{vis}}{\sqrt{H_{bep}^{water}}\nu} , \tag{1.6}$$

where ν is the kinematic viscosity of the oil and N is the pump rotational speed. To achieve the right value of q_{bep}^{vis}, it is first guessed to calculate $R_{Stepanoff}$; then, the first correction factor is obtained from the chart. The specific speed with viscous oil should match that for water. Otherwise a new value is guessed until this condition is satisfied.

1.3 Ippen (1946)

Ippen (1946) conducted over 200 performance tests for fluid viscosities up to 10,000 SSU, with four different single stage centrifugal pumps (not ESPs). He defined Reynolds number as

$$R_D = 2620 \frac{N d_2^2}{\nu . 10^5} \ , \qquad (1.7)$$

where d_2 is the impeller diameter in ft. A plot of head correction factor $\frac{H_o}{H_w}$ versus R_D was created. Then, the flowrate correction factor can be obtained from the relationship

$$\frac{Q_o}{Q_w} = \sqrt{\frac{H_o}{H_w}} \qquad . \qquad (1.8)$$

Based on his experiments, the author indicated that his plots are not applicable for $R_D < 1000$.

1.4 Li et al. (2002)

According to Li et al. (2002), early empirical models developed before 1960 to correct for viscosity effect are less applicable for the currently used pumps, since those correlations were based on different ESP designs. The authors conducted many experiments on a commercial centrifugal pump for a viscosity range from 1 cSt to 250 cSt and showed large deviations in the HI correction factors from the measured values, as high as 10%, especially for viscosities higher than 50 cP.

1.5 Amaral et al. (2009)

Amaral et al. (2009) conducted experiments on a radial centrifugal pump and a semi-axial ESP, with viscosity range from 67 to 1020 cP using clear glycerin by changing temperature from 60 to 20°C. The authors concluded that affinity laws can be used for lower viscosities (below 60 cP) with a maximum deviation of 5%. However, at higher viscosities the deviation is much higher but the value was not reported in the paper.

1.6 Solano (2009)

Solano (2009) at the Tulsa University Artificial Lift Projects (TUALP) conducted a dimensionless analysis on the conservation equations of mass and momentum to calculate the ESP viscous performance, for viscosities ranging between 50 and 700 cP. From his experiments, a number of fitting parameters were obtained in order to predict the viscous performance of his specific pump (DN-1750). The author also showed that Stepanoff (1949) correlation can be extended to flowrates different than the BEP, by testing the performance at the lower and the upper recommended operating limits. His experimental results matched Stepanoff's correlation for all three points. As a result, Stepanoff's correlation can be applied for any specific speed value.

CHAPTER 2

EXPERIMENTAL SETUP AND RESULTS

This chapter presents experimental details for testing ESP performance under both oil and water-in-oil flow conditions, including experimental facility, data acquisition system (DAQ), the experimental procedure as well as experimental results. Multiple hydraulic variables and their effects on ESP stage pressure increment are demonstrated and analyzed in this chapter.

2.1 Experimental Facility

The experimental facility was rebuilt from a previous viscous flow loop used by Croce (2014) to conduct performance tests with the DN-1750 ESP under viscous fluid and emulsion conditions. The original flow loop at TUALP was built by Solano (2009) and was upgraded later by Banjar (2012) and Croce (2014). The experimental facility consists of a fully-closed liquid flow loop. The schematic of the facility layout is shown in Figure 2.1. The flow loop overall capacity is about 2,600 bpd of water flowrate. The detailed specifications and configurations of the major components in this loop are listed in Appendix A.

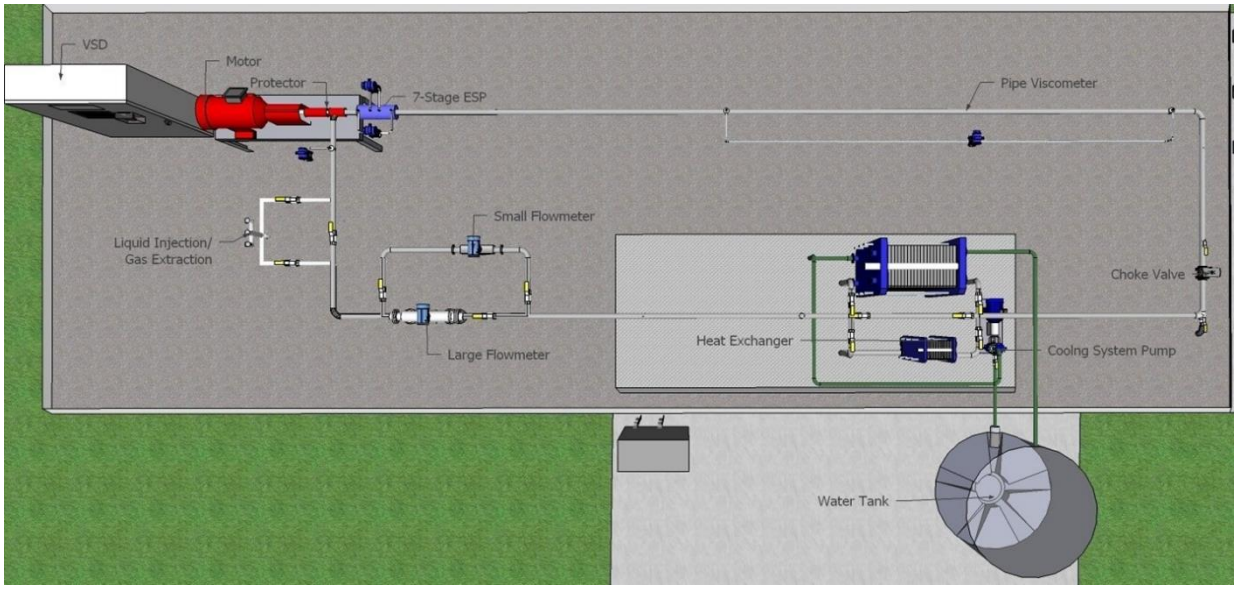

Figure 2.1 Schematic of TUALP viscous fluid ESP loop

2.1.1 Viscous Flow Loop

As shown in Figure 2.2, the loop is filled manually with liquid at the desired fractions of oil and water, from the 2" Polyvinyl Chloride (PVC) pipe injection port. The floating piece in the vertical transparent tube was used to minimize the entrainment of compressed air into the system. A compressor is used to pressurize the loop. The injection section is isolated by ball valves, and the pressurized air is released and replaced with liquid, which is then pressurized and connected to the already-pressurized section. In this study, the ESP intake pressure was set at 50 psig. Once the motor is switched on to a relatively low speed (2000 rpm), air pockets and dispersed large air bubbles can be clearly observed flowing in the horizontal transparent section, and traveling upward in the vertical transparent section. This process takes about 30 minutes to ensure that lowest possible volume of air is inside the loop. If pressure decreases to lower than the target value, the loop is re-pressurized until the desired intake pressure is achieved. A Coriolis flowmeter (Micro Motion DS300) mounted 6 ft upstream of the ESP is used to measure the single-phase or two-

phase flowrate and density. At downstream of the ESP, a PV section is installed including the development section. A flow control valve is installed to regulate the liquid flowrate. A heat exchanger is used to control the fluid temperature.

Figure 2.2 Fluid injection section

The pneumatic choke valve was originally located immediately downstream of the ESP. According to Zande et al. (1999), having an emulsion that passes through a choke valve can affect the emulsion rheology by altering the dispersed phase droplet size significantly as shown in Figure 2.3. Consequently, the measured emulsion viscosity in the PV can be very different from that corresponds to the ESP conditions.

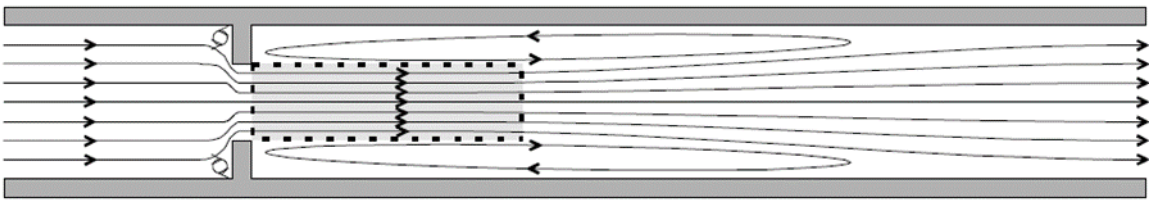

Figure 2.3 Schematic of emulsion flow through a choke valve (Zande et al. 1999)

Therefore, the valve was later relocated to the downstream of the PV. Repositioning the valve also provided additional space for the hydraulic development section and for the PV, which is the pipe length for the mixture velocity profile to be fully developed before the first port of the differential pressure measurement.

2.1.1.1 Pipe Viscometer: Initially, the PV consisted of short pipes (nipples), couplings, a long pipe where the pressure drop was measured and two tees. These tees were directed upward and were connected to several reducers to the quarter inch tubes. An issue with the initial setup is that the temperature probes were inserted in the same tubes used as the pressure ports so that the temperature probes were not inserted into the fluid flow. The interference between the temperature probes and pressure fluid path would cause inaccurate measurement of the differential pressure. Two quarter-inch tubes were connected between the differential pressure sensor and the reducers. This setup can cause local turbulence due to the sudden changes in the cross sectional area at the pipe connections. Therefore, the PV is significantly modified on several aspects. First, the whole PV uses a single standard pipe (20 ft), so that the disturbance is eliminated by avoiding the use of couplings. Secondly, the two differential pressure ports are 3/8-inch holes and on the same level of the flow center (0 degrees), to minimize the effect of gas entering the tubing connected to the pressure transmitter. Thirdly, temperature probes are positioned more than 8 ft upstream of the first pressure port, and 6 inches downstream of the second one, so that the probes do not interfere. Temperature probe tips are adjusted to be exactly at the middle of the flow, i.e. 1 inch from the inner pipe wall. Fourthly, no tees or crosses are installed downstream of the PV, only a 90-degree elbow, to minimize the stagnant region which may affect the differential pressure reading. Finally, although the distance between the two differential pressure ports is shortened from 13.5 ft to 10.5

ft, the hydraulic development section is extended from 2.5 ft to 8.5 ft, based on the minimum required entrance length.

In order to measure the viscosity for Newtonian fluids or the effective viscosity for non-Newtonian fluids accurately, there should be a minimum distance for the mixture velocity profile to fully develop after the ESP and before the first port for the differential pressure measurement. Two correlations dependent on Reynolds number and the pipe hydraulic diameter were proposed by White (1998), one for laminar and the other for turbulent flow as follows:

$$Le_{Laminar} \approx 0.06ReD \tag{2.1}$$

$$Le_{Turbulent} \approx 4.4Re^{1/6}D \tag{2.2}$$

where *Re* is the Reynolds number and *D* is the pipe diameter. A sensitivity analysis was performed in order to design the optimum entrance length and the distance over which the pressure difference is measured. With respect to different anticipated dynamic viscosity values and corresponding densities, and with different flowrates, Reynolds numbers are calculated. Then, the minimum entrance length is estimated based on White's correlations. The results are presented in Figure 2.4

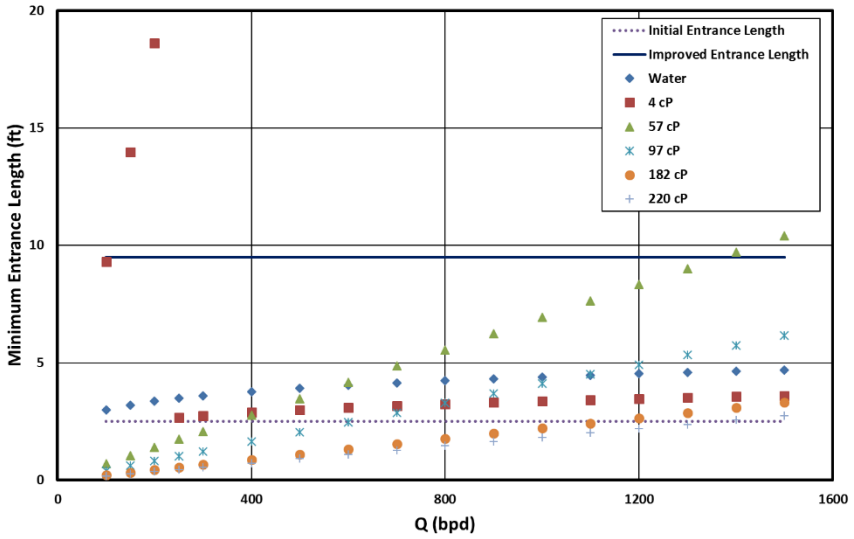

Figure 2.4 Minimum entrance length

The Moody relationship between the friction factor and the pressure drop across the pipe can be expressed as

$$f_M = \frac{2D}{\rho v^2}\frac{dP}{dL} \quad , \tag{2.3}$$

where ρ is the fluid density, v is the average velocity of the fluid, *dL* is the distance between the two pressure ports, and *dP* is the measured differential pressure. For laminar flow, Moody friction factor can be calculated as

$$f_M = \frac{64}{Re} \quad . \tag{2.4}$$

Equating Equation (2.3) to Equation (2.4) yields

$$\frac{2D}{\rho v^2}\frac{dP}{dL} = \frac{64}{Re} \Rightarrow \frac{2D}{\rho v^2}\frac{dP}{dL} = \frac{64\mu}{\rho v D} \quad ; \tag{2.5}$$

therefore,

$$\mu = \frac{D^2}{32v}\frac{dP}{dL} = \frac{D^2}{32\frac{Q}{A}}\frac{dP}{dL} = \frac{\pi}{4}\frac{D^4}{32Q}\frac{dP}{dL} = \frac{\pi D^4}{128Q}\frac{dP}{dL} \quad , \tag{2.6}$$

where μ is dynamic viscosity, *Q* is the volumetric flowrate, and *A* is the cross-sectional area. In our case, the diameter of the PV is exactly 2 inches. The distance between the differential pressure ports is 10.5 ft. Replacing these values and applying the suitable unit conversion factors in Equation (2.5) yields Equation (2.6) which is the apparent viscosity estimation from the PV:

$$\mu(cP) = 27.755\frac{dP(Pa)}{Q(bpd)} \quad , \tag{2.7}$$

For turbulent flow, friction factor is not calculated straightforward. Different correlations exist but the most well-known one is proposed by Colebrook in Equation (2.7). This correlation is based on a set of experiments conducted for turbulent flow in smooth and rough pipes. It shows that the friction factor is a function of not only Reynolds number, but also the absolute pipe roughness which is approximated to be 0.0006 inches for stainless steel pipe. The transition from

laminar to turbulent flow occurs at Reynolds number of 3000. Thus, Equation (2.3) is first solved to find the Moody friction factor, then Equation (2.9) is solved to obtain viscosity.

$$\frac{1}{\sqrt{f_D}} = -2\log\left(\frac{\varepsilon}{3.7D} + \frac{2.51\mu}{\rho v D\sqrt{f_D}}\right) \tag{2.8}$$

$$\therefore \mu = \frac{\rho v D\sqrt{f_D}}{2.51}\left(10^{\frac{1}{-2\sqrt{f_D}}} - \frac{\varepsilon}{3.7D}\right) \tag{2.9}$$

Based on the viscosity calculation approach, a sensitivity analysis was conducted to have confidence in the pressure drop measurement. For different viscosities, densities, and flowrates, with a pressure sensor resolution of 100 Pa (Croce, 2014), the minimum required spacing is calculated for each case and results are shown in Figure 2.5. Clearly, at low viscosity and low flowrates, a very long distance between the differential pressure ports is required. However, for most viscosities and flowrates, differential pressure can be measured if the spacing between the two ports is 10.5 ft.

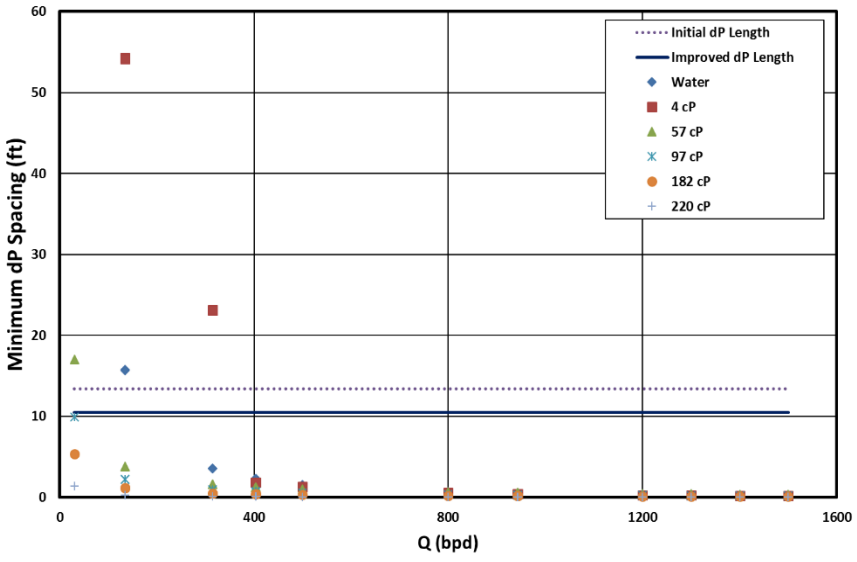

Figure 2.5 Minimum required dP spacing

The maximum required entrance length corresponds to the higher end of Reynolds number in the laminar flow regime that can happen at 4 cP viscosity for our case. Moreover, this viscosity requires a very long spacing between the differential pressure ports, which is beyond the available space in the facility. A very long PV creates high frictional pressure drop across the flow loop at high oil viscosity and the ESP may not be able to achieve even medium flowrates. Therefore, the PV was chosen to be a single piece section which is 20 ft long, with a hydraulic development section of 9.5 ft and a differential pressure measurement section of 10.5 ft.

2.1.2 ESP Test Bench

The ESP test bench consists of the ESP, motor, thrust chamber, and other equipment that are needed for ESP operation. The studied ESP is a 7-stage DN-1750 series 400 (REDA). The best efficiency point (BEP) is 1750 bpd at 3500 rpm with a stage pressure increment of 8.3 psi, based on which the estimated N_S is 2731. The water performance curves at different rotational speeds are shown below, including head curves (Figure 2.6) and efficiency curves (Figure 2.7). The pump head curve moves toward the left-bottom corner when the pump rotational speed is reduced. The efficiency curve moves to the left-side on the chart. The maximum open flowrate at N = 3500 rpm is 2500 bpd, while the maximum shut-in pump head is 13.1 psi. In Figure 2.7, the asymptotic value of the hydraulic efficiency for DN-1750 ESP under varying rotational speeds is below 70%. For a centrifugal pump the affinity law can be used to predict the pump head, efficiency, and brake-horse-power at different rotational speeds for water flow if the performance curve at a fixed rotational speed is known. Stepanoff (1957) derived the affinity laws as follows:

$$\frac{Q_1}{Q_2} = \frac{N_1}{N_2} \tag{2.10}$$

$$\frac{H_1}{H_2} = \left(\frac{N_1}{N_2}\right)^2 \tag{2.11}$$

$$\frac{BHP_1}{BHP_2} = \left(\frac{N_1}{N_2}\right)^3 \tag{2.12}$$

where *Q*, *H*, *BHP* are flowrate, hydraulic head, and brake-horse-power, respectively.

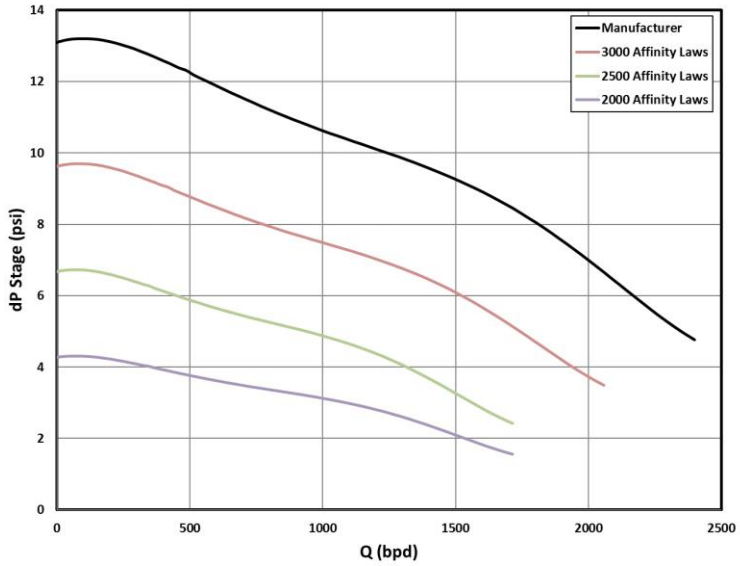

Figure 2.6 DN-1750 ESP water performance curves

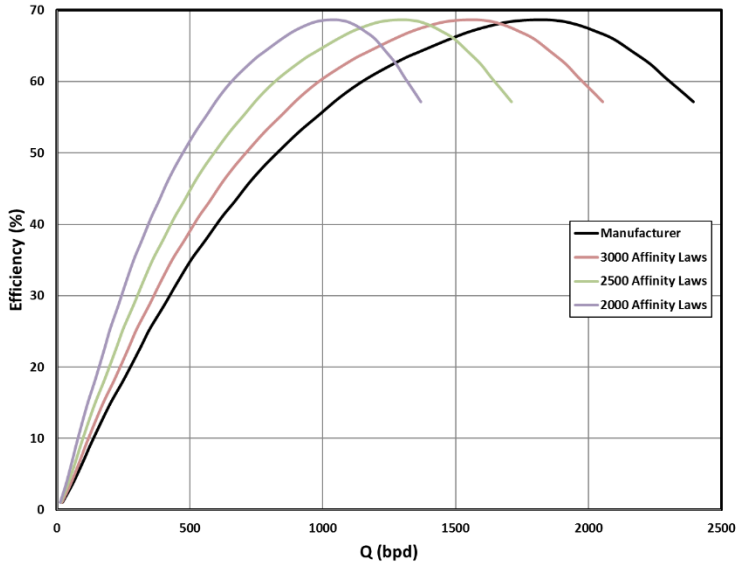

Figure 2.7 DN-1750 ESP efficiency curves

Quarter-inch holes are drilled on the pump housing at stage 3 upstream and downstream, as well as upstream of stage 1 and downstream of stage 7 to allow the communication between the pressure transmitters and the working fluids. The pressure port is located between the upstream diffuser and downstream impeller. Figure 2.8 shows the actual view of the ESP testing bench.

The pressure increments over stage 3 and stage 0~7 are measured using the differential pressure transducers (Rosemount 3051SD). The temperatures at the ESP intake and at the ESP downstream are measured with three-wire platinum RTDs (resistance temperature detector).

The ESP testing bench consists of the multistage ESP, motor, variable speed drive (VSD), thrust chamber and auxiliary electrical equipment for pump operations. ESP is driven by a four-pole 100 hp electric motor (Baldor Reliance) via VSD (Centrilift 2250-3VT). After the PV section, a 1.75-inch pneumatic control valve is installed to control the liquid flowrate. ESP and electric motor are connected through the thrust chamber which holds thrust force and allows the shaft rotating. The rotational speed and shaft torque are measured by the torque cell, including a sensor (Lebow 1805-5K) and a monitor (Lebow 7541). However, torque cell has some issues and only rotation speeds are recorded for all experiments.

Figure 2.8 Top view of pressure measurement ports

2.1.3 Data Acquisition System

The data acquisition system is based on compact FieldPoint module from National Instrument (NI), which is an expandable and programmable automation controller consisting of a series of analog signal input/output modules and intelligent communication interfaces. All analog signals (4~20 mA) from field terminals (pressure transducers, temperature transmitters, flowmeters, etc.) are connected to the NI input modules (cFP-AI-111), where the sensor electric current signals are scaled up into engineering units. Similarly, the internal control signals (4~20 mA) from NI output module (cFP-AO-200) are sent to field terminals (control valves and VSD) for the control purpose. The NI modules transmit all signals and communicate to the data processing computer through RS-485 interface and Ethernet cable. A Dell computer equipped with Intel® core processor (3.2 GHz), 4 GB RAM and 500 GB hard disk serves as the data processing center.

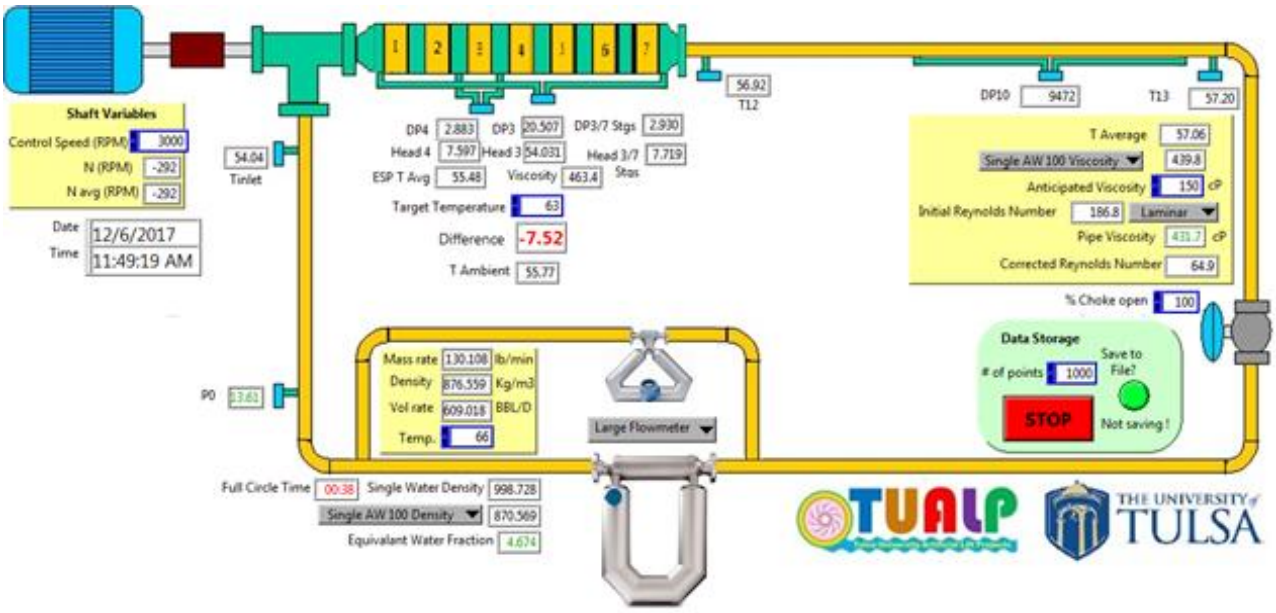

Figure 2.9 Data acquisition system of TUALP viscous ESP loop

As shown in Figure 2.9, the DAQ program is written in a graphic-programing language LabVIEW 2013 for the data acquisition and control of flow loop. Meanwhile, the LabVIEW-based

DAQ program is able to monitor data in the experiments. The raw data recorded by DAQ are exported into text file for further processing.

2.2 Experimental Program

2.2.1 Test Fluids

Tap water and mineral oils are used in this study as the working fluids. The in-situ single-phase or mixture density is measured by Coriolis flowmeter (Micro Motion DS300). The first mineral oil used is Non Detergent-20 (ND20) which is considered to have an intermediate viscosity. Across the tested temperature range in the lab from 120 °F to 60 °F, its viscosity changes from 37 cP to 370 cP. Lab test results match the PV results and both methods show that this oil behaves as a Newtonian fluid when tested at different shear rates. There are two batches of this oil, an old batch and a new batch. The old one was used by two students before this study, and possibly the high temperature caused it to change color to brown while the new batch of ND20 oil is clear yellow. Physical properties for both batches are tested and confirmed that both batches are almost identical. Viscosity is the same for both oils while density is only 5% different. The second oil is Isopar V, which has a low viscosity, ranging from 6 cP to 20 cP corresponding to temperatures between 120 °F and 60 °F, with Newtonian behavior. Both are much lighter than water but Isopar V is much lighter. To correct the effective viscosity of emulsion at the ESP condition, AW100 hydraulic oil is used to run as the last set of experiments, by matching the head created by the stage using this oil to the head created by the emulsion. Similar to the other oils, it shows Newtonian behavior when it is tested at different shear rates. Lab results from the rotational viscometer (Anton Paar RheolabQC) as well as the densitometer (Anton Paar DMA 4500 M) are

shown in Figure 2.10 and Figure 2.11, respectively, for all three oils and tap water. Additionally, oil and water viscosity and density correlations for these oils are listed in Equations 2.13 through 2.20.

$$\mu_{AW100} = 2890.7e^{-0.033T} \quad (2.13)$$

$$\mu_{ND20} = 1686.15e^{-0.0323T} \quad (2.14)$$

$$\mu_{Isopar\,V} = 64.85e^{-0.0204T} \quad (2.15)$$

$$\mu_{Tap\,Water} = 16.255T^{-0.594} \quad (2.16)$$

$$\rho_{AW100} = -0.3438T + 893.26 \quad (2.17)$$

$$\rho_{Old\,ND20} = -0.3474T + 894.28 \quad (2.18)$$

$$\rho_{New\,ND20} = -0.3674T + 890.27 \quad (2.19)$$

$$\rho_{Isopar\,V} = -0.3276T + 830.59 \quad (2.20)$$

$$\rho_{Tap\,Water} = -0.1739T + 1010.1 \quad (2.21)$$

where μ is the fluid dynamic viscosity in cP, ρ is the density in kg/m^3 and T is the temperature in °F.

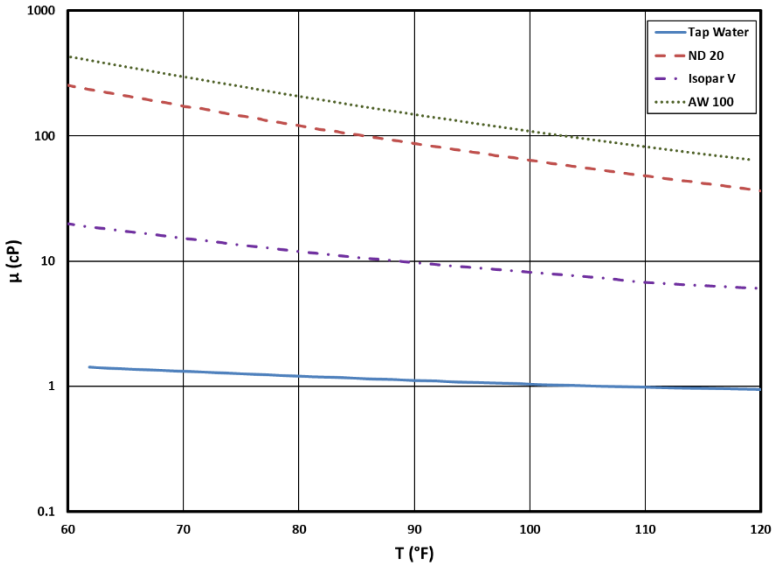

Figure 2.10 Fluids dynamic viscosity curves

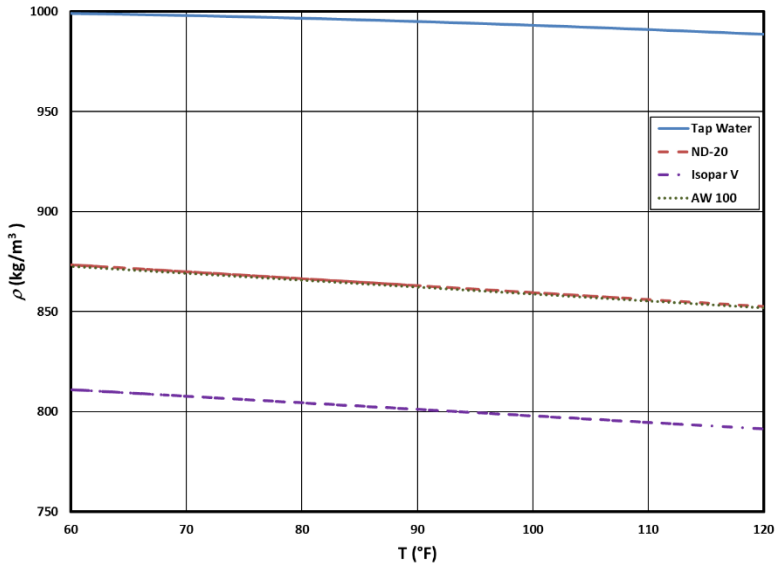

Figure 2.11 Fluids density curves

2.2.1.1 Interfacial Tension: The air-oil interfacial tension may play a role in the difference between the old and the new ND20 emulsion effective viscosities. Both oils have the same viscosity and almost same density. Thus, it is suspected that interfacial tension is one of the reasons of the variation of the inversion point from 20% to 59% water fraction for the old ND20 oil. We conducted a set of measurements of air-oil interfacial tension using the capillary rise method shown in Appendix A and the results are displayed in Figure 2.12. It is shown that the interfacial tension for the old ND20 is close to the value reported in Brito (2014) report. For the new ND20 oil, the value is slightly higher. The interfacial tension was not reported in the ND20 Material Safety Data Sheet (MSDS). In addition, air and Isopar V interfacial tension values are close to the reported values in the Isopar V MSDS.

Later, another set of interfacial tension measurements were conducted by using Du Noüy ring method with an instrument named BZY 202 and a thermostatic bath as shown in Appendix A. We can notice acceptable results for air-tap water interfacial tension in Figure 2.12. In addition,

air-new ND20 and air-Isopar V interfacial tensions results match the capillary rise method very well. For air-old ND20 interfacial tension, the result is reasonable, although it is higher than the value reported by Brito (2014), where it should be lower as temperature increases.

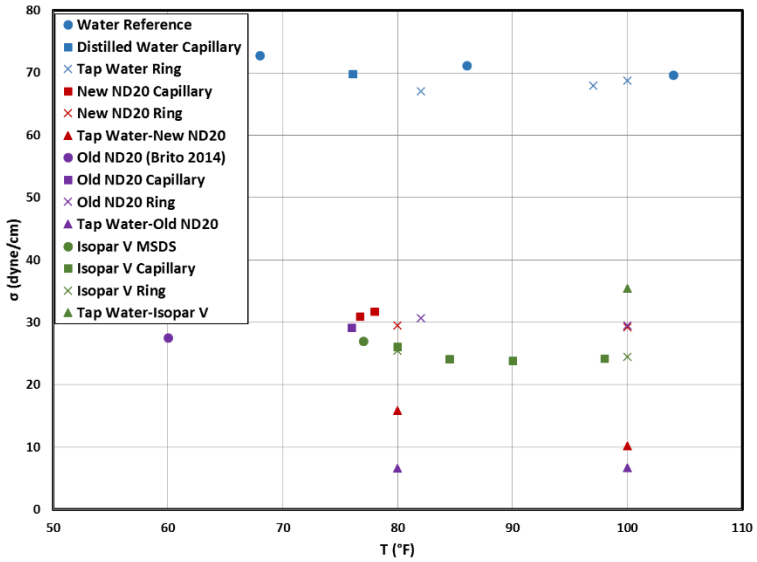

Figure 2.12 Air-oil interfacial tension for different oils

Figure 2.12 also shows that water-Isopar V interfacial tension is in agreement with Peters (2013) trend, which suggests that the water-oil interfacial tension value is between the air-water interfacial tension and the air-oil interfacial tension. In contrast, water-old ND20 and water-new ND20 interfacial tensions are much lower than air-old ND20 and air-new ND20, respectively. This is possibly due to the presence of impurities in the flow loop, which may come from ambient, or from the ESP stages metal wearing, or the contamination from the previous experiment by the previous oil. These impurities can act like a surfactant, lower the water-oil interfacial tension and may change the inversion point.

The working fluid is sampled from a ball valve downstream of the choke valve while fluid is flowing at the highest achievable flowrate to confirm the sample is representative. Samples are left to segregate by gravity to identify and correct the estimated factor of each liquid if needed and

to ensure that no other liquid contaminating the flow loop in the case of single phase. In order to achieve the desired oil and water fractions in two-phase tests, the flow loop total volume needs to be estimated. Then, oil and water with the calculated quantities are injected. However, due to the stagnant spots and dead volume areas throughout the loop, this approach may not be accurate. Therefore, density reading from the flowmeter is used as a reference. Since we know the density of each phase as a function of temperature and the density measurements are reliable as detailed in Appendix B, we can estimate the fraction of each phase by the no-slip mixture density definition:

$$\rho_m|_T = \rho_w|_T \times f_w + \rho_o|_T \times (1 - f_w) \tag{2.22}$$

where *T* is the temperature at the mass flowmeter, ρ_m is the mixture density, $\rho_w$is the water density corresponding to that temperature, ρ_o is the oil density corresponding to that temperature, and $f_w$is the water fraction. This procedure requires the loop to run long enough after pressurizing, so that the oil and water fractions are evenly distributed along the flow loop sections. Then, if the desired fraction needs to be adjusted, the oil or water needs to be replaced by water or oil, respectively, if possible. Otherwise, the mixture is extracted from the loop and the single phase is added to obtain the desired fraction. Once the desired fraction is achieved, the rest of the experiment is similar to that for single phase.

2.2.2 Experiment Procedure

The experimental procedure adopted in this study is similar to Croce (2014).

2.2.2.1 Single Liquid Testing Procedure: Each performance curve is obtained under constant intake pressure, constant average ESP temperature, and constant rotational speed. By changing the control valve opening, the liquid flowrate is regulated. The differential pressures at stage 3 as well as for the entire ESP are recorded then exported to data files, with other parameters. Experimental measurements is stepwise which is more stable compared to continuous measurement, easier to process and requires less data space. The stepwise measurements require that the experimental system to reach a stable working condition, at which the intake pressure, average temperature, and rotational speed are kept constant. Then, the hydraulic data including stage pressure increment and flowrate are recorded for a certain period (50 sec in this study) with data rate of 20 Hz. An arithmetic averaging is applied to each dataset so that the average value for each flow condition is obtained.

2.2.2.2 Oil-Water Testing Procedure: In this study, emulsion experiments are performed similar as the single-phase liquid testing, except two major differences. First, density measurement from the mass flowmeter is observed while the loop is running until no major fluctuation is detected. Second, emulsion is expected to become thicker as it takes longer time to circulate through the ESP stages, as a result of shearing. Therefore, within the first few minutes, differential pressure values in the PV increase until a certain value, at which the emulsion reaches its most stable condition.

The total volume of working fluid, V_{tot} , in the flow loop measured by drainage is about

0.48 barrels, i.e. V_{tot} = 20 gallons. Due to some stagnant points and the bypass section, the actual liquid volume that flows continuously during the experiment is around 0.33 barrels, i.e. $V_{actual} \approx$ 14 gallons.

2.2.3 Test Matrix

The test matrix is listed in Table 2.1 for all liquids. During experiments, it was realized that conducting more experiments at different temperature values were more important than running experiments at low rotational speed. Therefore, no further experiments were conducted for 2000 rpm ESP rotational speed. Water continuous emulsion was unstable which made it difficult to maintain the same oil and water fractions throughout the loop due to slippage between the phases. Therefore, it is not feasible to run experiments with water continuous emulsion in the current setup.

Table 2.1 Experimental matrix

Fluid	**Water Fraction (%)**	**Temperature (°F)**	**ESP Rotational Speed (rpm)**	**Choke Opening (%)**
Tap Water	100	90	3500, 3000, 2500	100, 95, 90, 85, 80, 75, 70, 67, 63, 60, 57, 53, 50, 47, 43, 40, 37, 33, 30
Old ND20	0, 10, 20, 30, 40, 50, 60	88		
New ND20	0, 10, 15, 20, 25, 30	80, 88, 100		
Isopar V	5, 10, 15, 20, 25, 30, 35, 40	95		
AW100	0	65 to 80		

2.3 Experimental Results

This section presents the experimental results under both single-phase liquid and oil-water flow conditions.

2.3.1 Single-Phase Liquid Results

Results shown here include single-phase water and oil results. First, the experimental results for ESP performance are presented. Then, PV results are explained in the second part.

2.3.1.1 Performance Curves: The measured head curves with water flow at stage 3 are shown in Figure 2.13. The horizontal and vertical coordinates are liquid flowrate Q (in bpd) and pump head H (in psi), respectively. Each color corresponds to a different pump rotational speed. The black solid curve at N = 3500 rpm is obtained directly from catalog and the other catalog curves are calculated with the affinity law. Data points are experimental measurements after modification of the flow loop.

As can be seen, a considerable degradation in the performance, as a result of the ESP wear out after many years usage. Figure 2.13 also shows results obtained from the previous experiment performed on the pump by Croce (2014). He ran a water test, but he did not use the data acquisition system unfortunately. The fluctuation in the pressure sensor and in the mass flowmeter readings cannot be captured easily which makes the average reading difficult to obtain in a timely manner and the human error is more likely. Stage head curves from previous measurements are omitted since data is inconsistent and the repeated water experiments are only shown from this study in Figure 2.14. Banjar (2012) conducted experiments with mineral oil of viscosity close to water. It

can be seen that there is a close match for most of the data of Banjar (2012) to this study, except for flowrates higher than 1400 bpd. One possible reason is that friction losses for water is lower, assuming flow is turbulent but close to the transition to laminar flow regime. Still Croce (2014) data are shifted but they are much better than the pressure increment comparison. Measured boosting pressure is inconsistent with the average data. At high flowrates, the ESP average performance is better while it matches the stage performance at medium flowrates and it is lower at low flowrates.

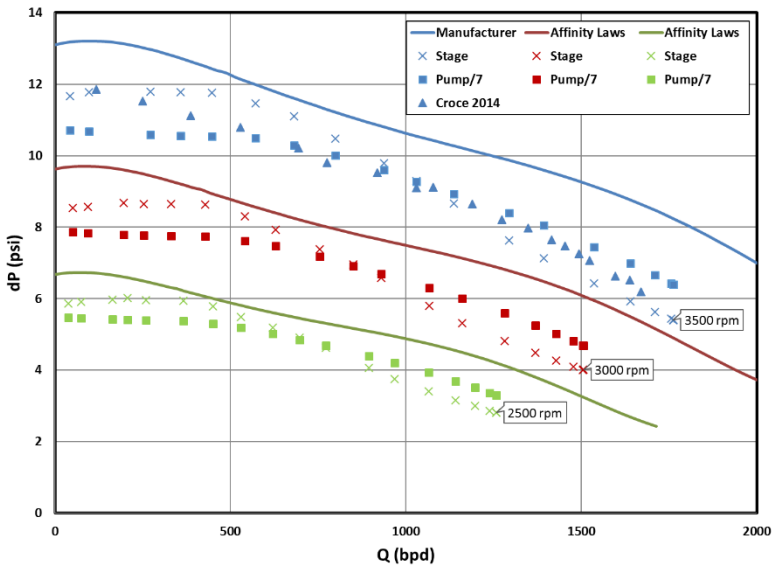

Figure 2.13 Experimental performance curves comparison

Single-phase oil test results for different viscosities at different rotational speeds are shown in Figure 2.15, in which we can see that the performance becomes worse with viscosity increase, as expected. As viscosity increases, friction losses throughout the loop increase and some of the kinetic energy is dissipated into heat and the pump gives lower flowrate at the maximum choke opening. The same principle applies within the stage itself which results in lower boosting pressure. There are some unexpected overlaps which can be a result of gas intrusion into the pressure measurement lines although we tried to bleed the trapped gas before each experiment.

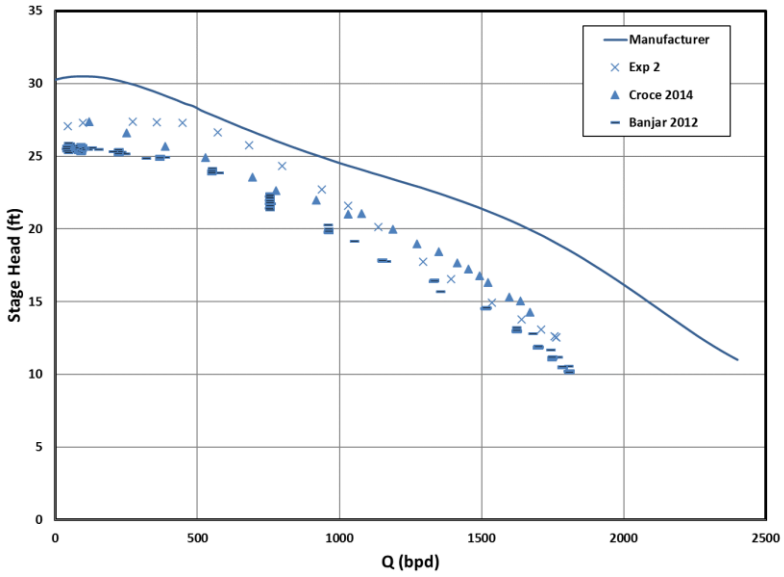

Figure 2.14 ESP head curves comparison

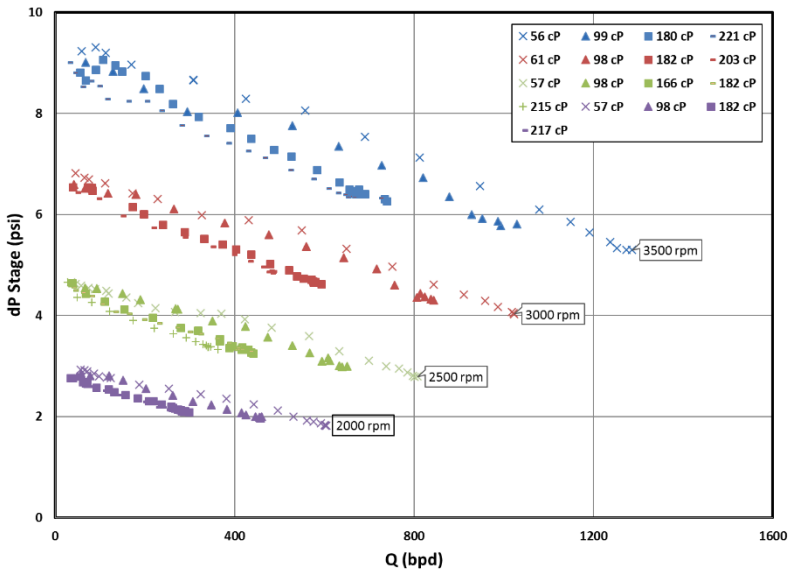

Figure 2.15 Stage performance for different oil viscosities at different rpm

As mentioned earlier, the new batch of ND20 oil was tested at 88 °F and 104 °F to confirm the ESP stage performance with the old batch results as shown in Figure 2.16. The match is excellent for most of the data.

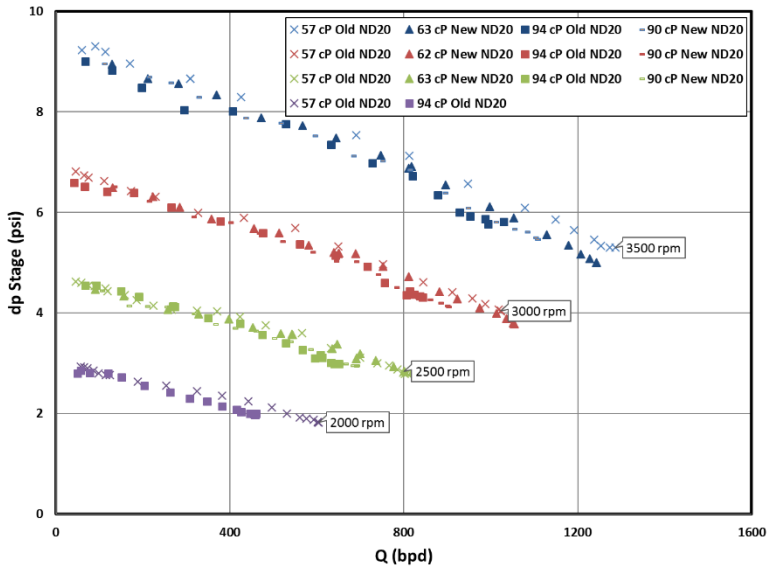

Figure 2.16 New and old ND20 oil comparisons at 94 and 57 cP

2.3.1.2 Pipe Viscometer: Single phase tests are water tests, as well as oil tests at different temperatures, at different rotational speeds. Since water has a low viscosity and high density, its Reynolds number is always high. For flowrates higher than 50 bpd the flow is turbulent in the flow loop. The independent variables *dP* and *Q* can be transferred linearly into τ and $\dot{\gamma}$, respectively, as follows:

$$\tau_w = \frac{D}{4}\frac{dP}{dL} \tag{2.23}$$

$$\dot{\gamma} = \frac{8v}{D} = \frac{8Q}{DA} = \frac{32Q}{\pi D^3} \tag{2.24}$$

Therefore, we can consider the *dP* vs. *Q* curve as a flow curve for the fluid in order to analyze the flow behavior. For water, results from the old PV are very scattered so they are not used. When the loop was upgraded, water results show a perfect match to the ideal curve using Colebrook correlation for turbulent flow as shown in Figure 2.17 with instrument accuracy of ±0.25%. For tests with ND20 oil, Figure 2.18 shows acceptable trends of Newtonian fluid, since viscosity is independent on the shear rate, which agrees with the rotational rheometer test results.

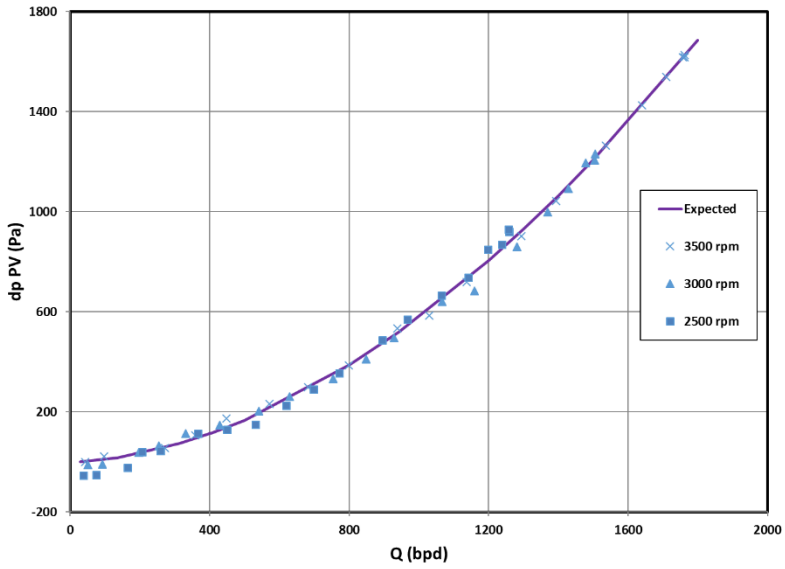

Figure 2.17 New PV results for water

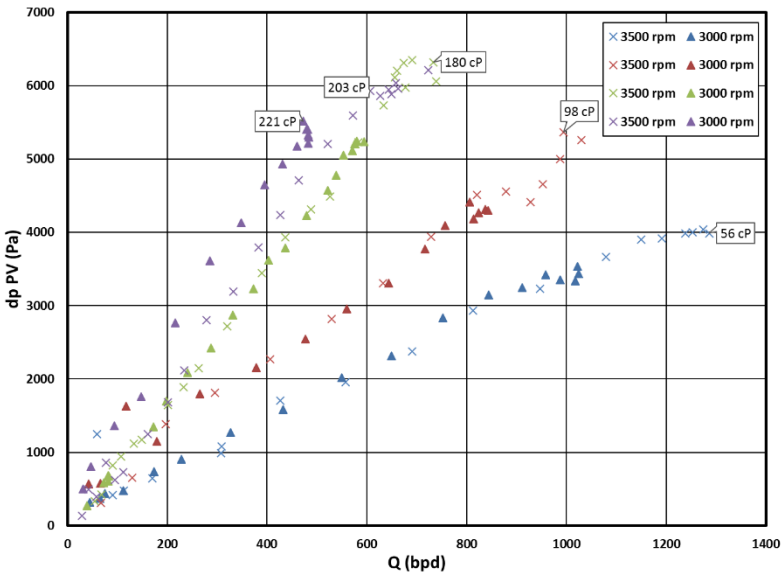

Figure 2.18 dP across PV for 3000 and 3500 rpm

With the new batch of ND20 oil, two cases of single-phase oil experiments were revisited, specifically 57 cP and 94 cP, and the new PV results are shown in Figure 2.19. Compared to the old setup results, the new setup results show a more organized data with less noise, giving us the confidence that the PV measurements are reasonable.

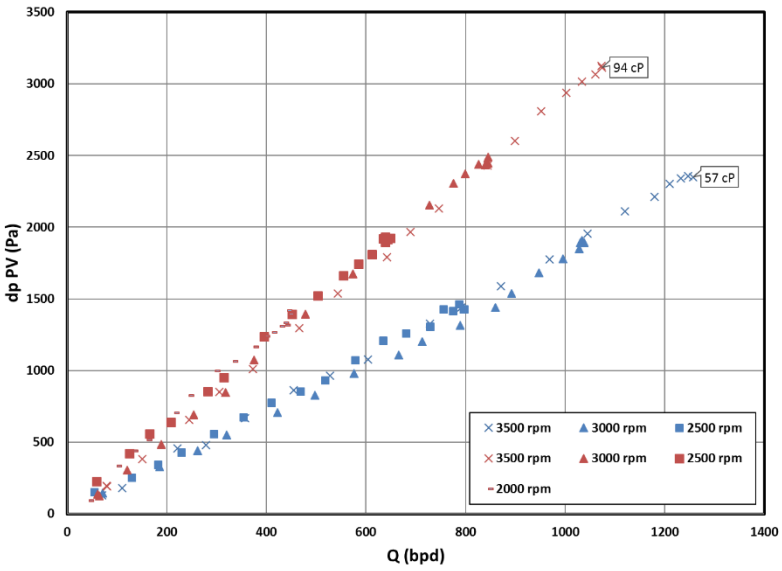

Figure 2.19 dP across new PV

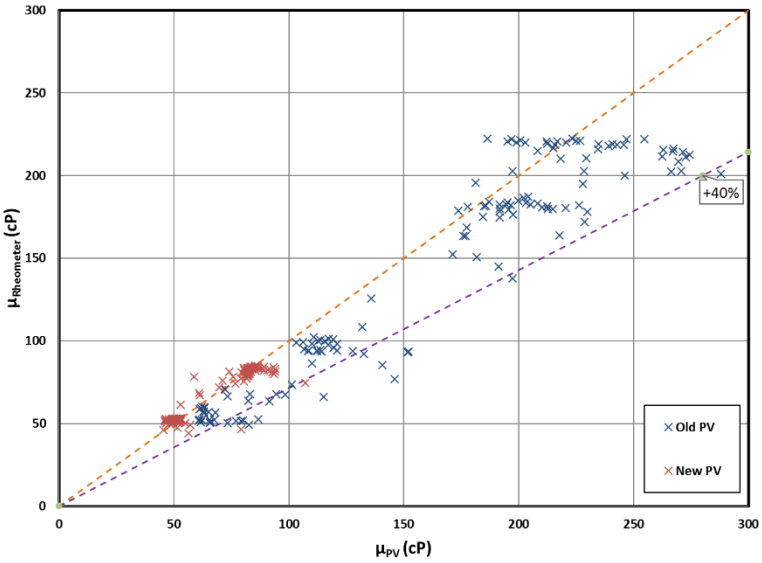

Figure 2.20 Old and new PV validation

Another approach to validate PV measurements is to plot PV results against rotational viscometer results before and after PV upgrade as shown in Figure 2.20. For the old PV, there is a significant deviation to the right of the line of equity. It was initially thought that a small amount of residual water in the loop (<2%) created emulsion with higher viscosity compared to oil. However, later two-phase experiments showed that water fraction would increase the viscosity by

10 cP at most. Therefore, it is believed that the old setup had some major issues that highly affected the pipe differential pressure readings. On the other hand, the new PV results show significant improvement compared to the results obtained from the previous setup.

2.3.2 Oil-Water Results

The first part presents the experimental results for ESP performance curves while the second is dedicated for PV results.

2.3.2.1 Performance Curves: One of the challenges in oil/water tests is that emulsion is mostly transient. The emulsion rheological properties change with time and location such as the effective viscosity and the dispersed droplet size. Performance curve results are shown in Figure 2.21 for different water fractions at different rotational speeds. All experiments were conducted at 88 °F as the average temperature.

When the water fraction increases, emulsion effective viscosity increases and the ESP performance drops, until the inversion point is passed where water becomes the continuous phase. At 50% water fraction for 3500 rpm, the stage boosting pressure is better compared to 40% water fraction, which is not expected and that can be a measurement error from the differential pressure transducer. Beyond 50% water fraction, effective viscosity drops sharply and the ESP performance improves. As shown later in this section, emulsion at 61% water is not stable in the flow loop which makes the ESP performance results unreliable, especially for flowrates lower than 1000 bpd. This explains the sudden drop in the performance of 61% water emulsion as flow being choked for all rotational speeds. It is also noticed that as viscosity increases, Reynolds number decreases, flow becomes more laminar and the curve becomes linear.

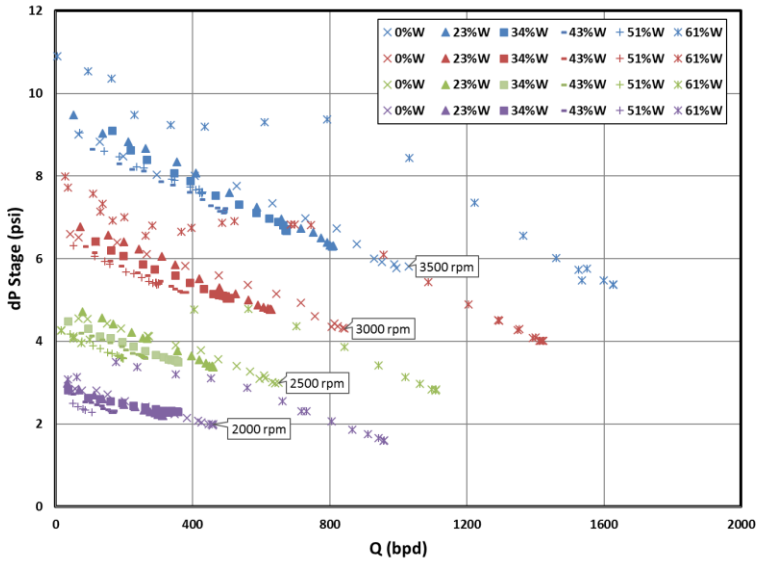

Figure 2.21 Stage performance for different water fractions with old ND20

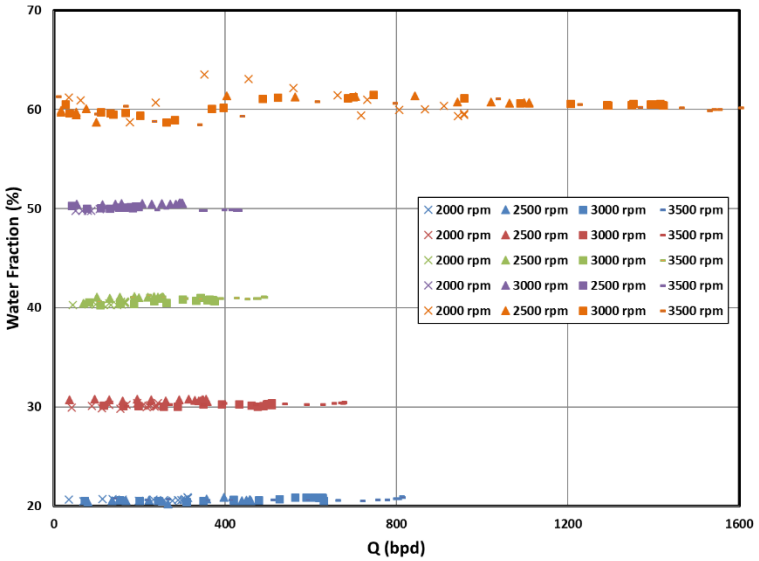

Figure 2.22 Water fractions from flowmeter

As shown in Figure 2.22, for all experiments from 12% to 51% water, the water fraction derived from the measured mixture density with the flowmeter, is almost constant throughout the experiment. However, it is seen that, for 61% water experiments, significant fluctuations in the water fraction take place. It was also noticed that, when the sample was collected, large portion of the water was segregated immediately, indicating that the emulsion stability is weak. Therefore,

the strange behavior in the PV results is caused by partial separation of water from the emulsion along the pipeline. The separated water may accumulate at the lower section of the heat exchanger as shown in Figure 2.23.

Figure 2.23 Flow path through heat exchanger

Since the emulsion is unstable at 61% water fraction the data cannot be used to investigate the pump performance. The rheology may vary significantly along the loop. Beyond the inversion point, high water fractions result in high emulsion instability. It is very difficult to control emulsion in those cases with the current facility heat exchanger setup, and without the heat exchanger the experiment temperature cannot be controlled. Therefore, no further oil in water emulsion experiments is conducted with water fraction higher than 51%.

The initial plan was to test emulsion with the new batch of ND20 oil at 80 °F in order to confirm the inversion point, as some references suggest that there is a slight change in the inversion point when temperature changes. Then, the inversion point was observed to be around 20% of water fraction which is much lower compared to the emulsion with the old batch of ND20 oil. Therefore, the emulsion was tested again at 88 °F and at 100 °F.

Performance curve results are shown in Figure 2.24, Figure 2.25, and Figure 2.26 at 80 °F, 88 °F and at 100 °F, respectively. From these figures for water fractions equal to 20% or lower, we can observe that the maximum achievable boosting pressure becomes lower as water fraction increases as a result of effective viscosity increase. The performance curves overlap indicating that the slight change in viscosity does not significantly affect the stage performance.

For water fractions higher than 20% at high flowrates, significant jump is observed which clearly indicates that water became the continuous phase and the inversion point is already passed. Therefore, inversion point for emulsion with the new batch of ND20 oil is somewhere between 20 and 25% of water fraction. The sudden drop in the performance for flowrates lower than 600 bpd is due to the instability of emulsion because there is a natural tendency for a liquid/liquid system to separate and reduce its interfacial area and hence, its interfacial energy (Kokal 2005). This instability affects the in-situ water fraction at the mass flowmeter and at the stage, and the collected data proved this by the fluctuation in the volume flowrate, density, and the stage boosting pressure.

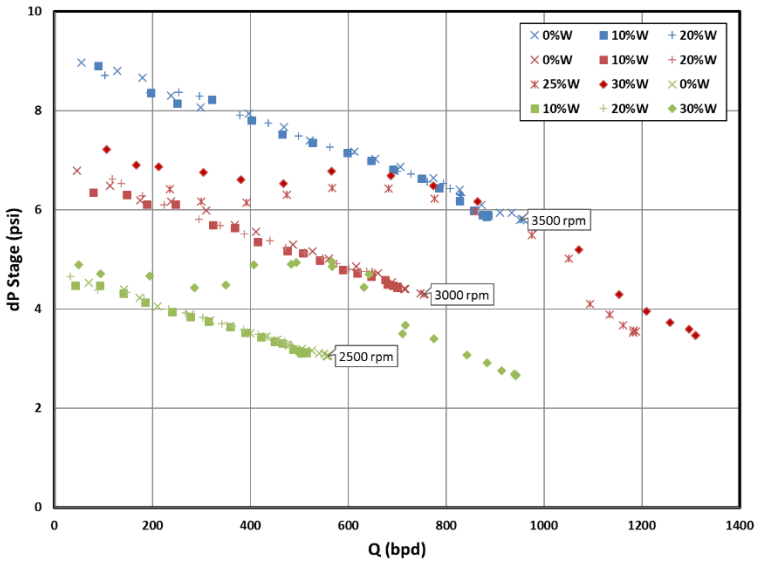

Figure 2.24 Stage performance for different water fractions with new ND20 at 80 °F

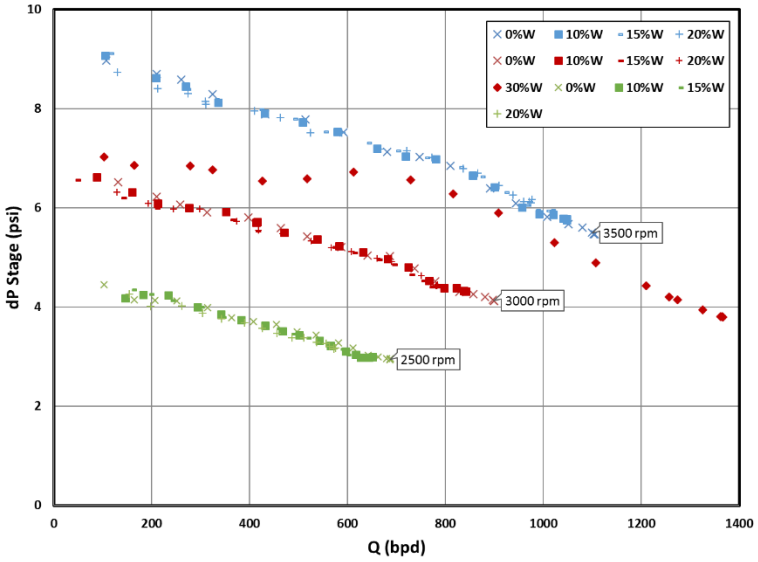

Figure 2.25 Stage performance for different water fractions with new ND20 at 88 °F

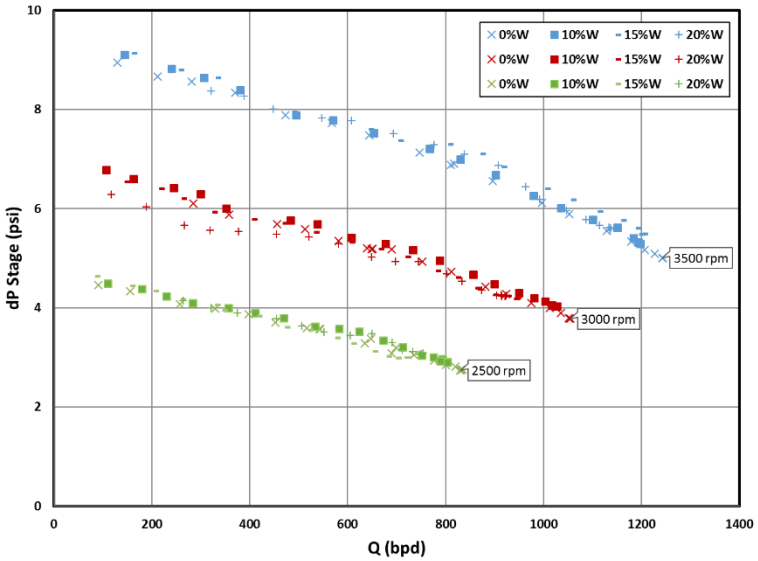

Figure 2.26 Stage performance for different water fractions with new ND20 at 100 °F

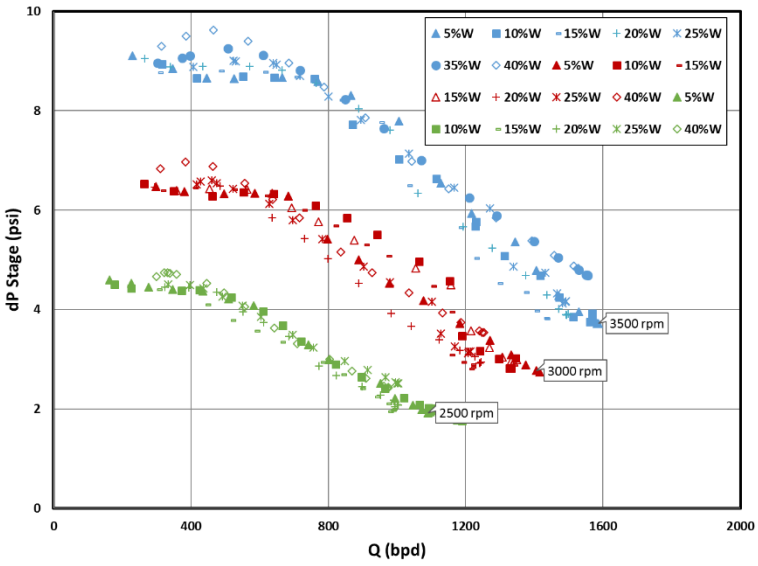

Figure 2.27 Stage performance for different water fractions with Isopar V

Emulsion with Isopar V oil tests conducted at a single average ESP temperature, which is 95 °F since it is easy to control at this value. From Figure 2.27 we can see many unique observations. First, there is more scatterings in the performance, although the effective viscosity varies within a small range compared to ND20 emulsion which we can see later under the PV section. In addition, it seems the 15% water fraction's curve is the lowest among the other water fractions for all three rotation speeds, which can indicate the inversion point takes place around this fraction. However, further observation on the density readings indicates that the inversion point is around 30% of water fraction. Figure 2.28 shows the fluctuation in the density reading at the maximum achievable flowrate at 3500 rpm. The fluctuation is minimal over the recording time (50 sec) except for 30% water, at which the fluctuation is obvious in all 3 tests even when we waited for 250 seconds for the fluctuation to be minimized but that did not occur. Moreover, the 30% water experiment was revisited by bypassing the heat exchanger (in red) to eliminate the effect of the oil-water segregation through the vertical sections. This minimized the fluctuation but still a considerable fluctuation is observed. Therefore, 30% is the least stable point among the

different water fractions and hence, it should be close to the inversion point. The severe fluctuation originates from the fact that oil continuous changes into water continuous which strongly affecting the emulsion rheology. In terms of the low performance at 15% water fraction, we can refer that to the tightness of the emulsion. When the water fraction is 20% or higher which causes the effective viscosity of emulsion to appear lower.

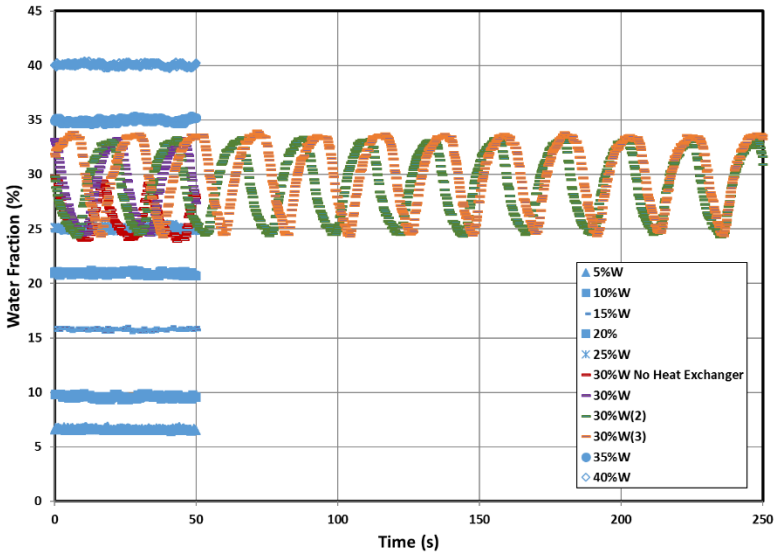

Figure 2.28 Water fractions at maximum flowrate at 3500 rpm

In Figure 2.29 it is shown that emulsion is mostly stable at high flowrates for water-in-oil emulsions. As flowrate decreases, water segregates partially and accumulates in the lower section of the heat exchanger. This should result in lower water fraction reading in the mass flowmeter as shown when flowrate drops below 1200 bpd. Further decreasing of flowrate (below 600 bpd) causes some water to separate and accumulate at the bottom of the mass flowmeter. This should lead to lower water fraction reading in the mass flowmeter. Once the inversion point is passed, oil-in-water emulsion seems to be more stable until flowrate 400 bpd, below which water segregates further and accumulates at the mass flowmeter.

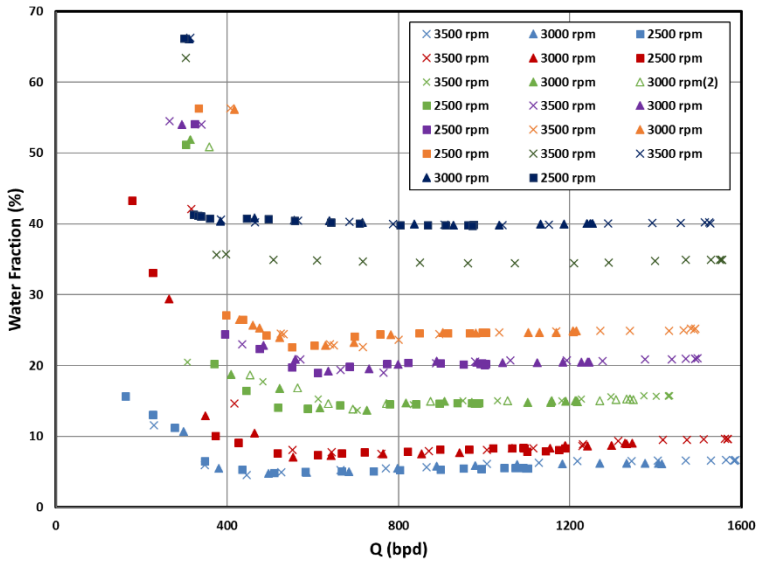

Figure 2.29 Water fractions from density readings

2.3.2.2 Pipe Viscometer: Results shown in Figure 2.30 are for two-phase tests with different water fractions, conducted after the loop modifications at ESP average temperature of 88 °F with ±0.5 °F range of uncertainty. Except 61% water results, most of the curves behave linearly with intercept at the origin and with coefficients of determination close to 1, indicating that emulsion follows Newtonian behavior. For 10% water experiments, results show curves shifting from the origin, so those measurements are not reliable especially for the mass flowmeter calibration error and these data are omitted. Effective viscosity for each water fraction is calculated by multiplying the slope of the best fitting line with the factor 27.8, as expressed in Equation (3.6).

At 61% water fraction, as flowrate decreases, effective viscosity increases significantly. The emulsion is most likely oil in water, i.e. oil is the dispersed phase while water is the continuous phase and the effective viscosity is around 30 cP. One could argue that the transition from laminar to turbulent flow causes the irregularities, but for flowrates lower than 1000 bpd, the Reynolds number is less than 1200, which is far from the transition boundary to the turbulent regime. The

nonlinearity of the flow curve is due to the emulsion instability as discussed in Figure 2.22. As a result, we believe the inversion point to be lower than 60% water fraction.

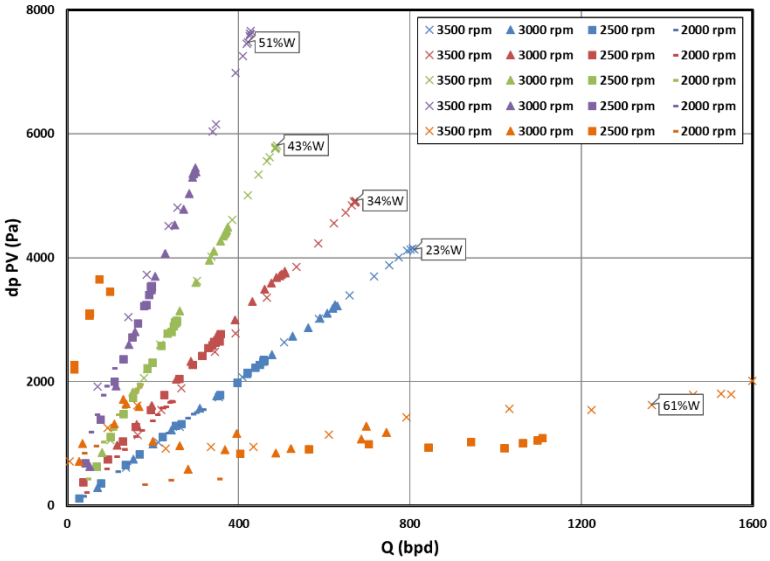

Figure 2.30 dP across PV for old ND20 oil emulsion

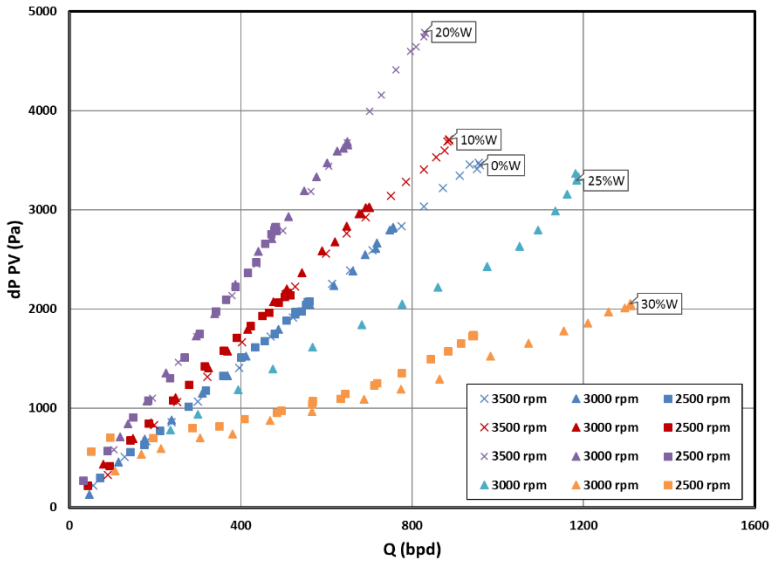

Figure 2.31 dP across PV for new ND20 oil emulsion at 80 °F

Starting from 100% oil in Figure 2.31, the pressure drop increases as water fraction increases which is a result of viscosity increase until 20% water fraction, after which the viscosity drops as water fraction increases. Therefore, we can say that the inversion point is between 20%

and 25% water. A slight difference in the value of the inversion point is anticipated due to contamination. However, compared to the inversion point for the old ND20 emulsion which is close to 60%, this result was absolutely unexpected. Therefore we retested the new ND20 emulsion at 88 °F to compare with the old ND20 emulsion. The same trend was found for this set of experiments as shown in Figure 2.32 as well as the other set on Figure 2.33. An observation is that as temperature increases, curves deviate from the best fit straight line. A clear observation for all PV results is that the curves, which can be translated into effective viscosities, are independent on the rotational speed. This contradicts our understanding that increasing rotational speed can increase the shearing at the stage impeller, which will decrease the effective viscosity. Since there is about 10 ft of distance between the ESP discharge and the first pressure port of the PV, it is suspected that this observation does not apply at the ESP condition.

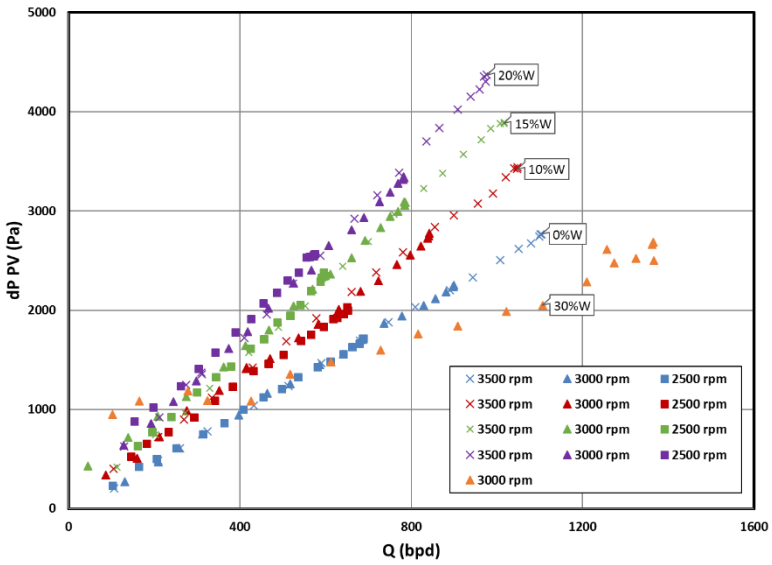

Figure 2.32 dP across PV for new ND20 oil emulsion at 88 °F

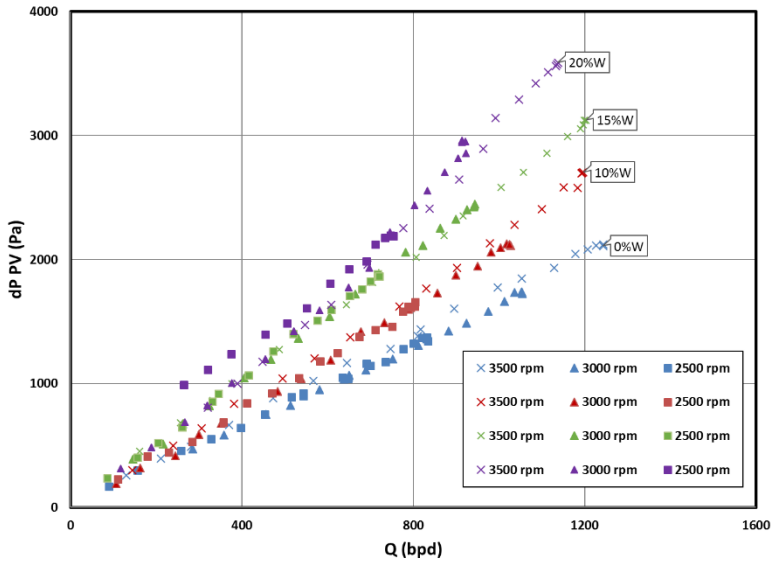

Figure 2.33 dP across PV for new ND20 oil emulsion at 100 °F

In Figure 2.34, solid curves are the ideal curves for the corresponding viscosity, with transition from turbulent to laminar flow regime at Reynolds number of 1000. From here we can confirm that flow is clearly turbulent for Reynolds number values higher than 1000, despite the critical point suggested by Colebrook in Equation (2.7) which is 3000. This can be a result of the high turbulence caused by the ESP overall. At 25% of water fraction, effective viscosity reaches to around 33 cP and flow appears to be laminar. Further increase in the water fraction leads to lower viscosity as a result of crossing the inversion point, and the emulsion is in turbulent flow regime. Since the emulsion is unstable at 30% water fraction as shown in Figure 2.28, PV results are omitted for this fraction. We can also conclude that the emulsion is Newtonian and the Isopar V emulsion inversion point is around 30% water fraction.

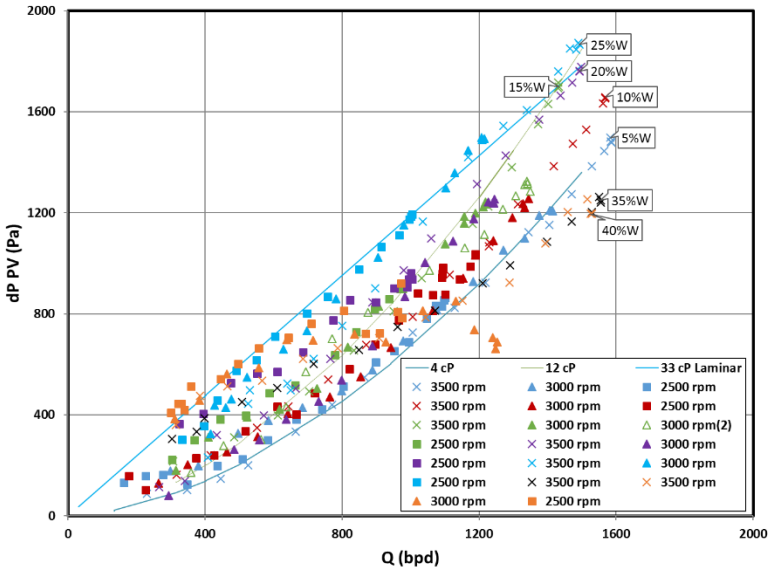

Figure 2.34 dP across PV for Isopar V emulsion

2.3.2.3 Effective Viscosity Validation with Single Phase Oil: It is suspected that the emulsion effective viscosity at the stage condition is comparable to that in the PV. The main drive to validate the effective viscosity is that PV shows viscosity as independent on the ESP rotational speed. Therefore, we came up with the idea that we match the performance of a single phase oil, with known viscosity, with emulsion. Hence, the correct way is to use pump head if we want to compare different fluids since their densities are different. By tuning the head-flowrate pair to match that for the emulsion, the average ESP temperature was chosen and was set for the rest of the matching experiment as shown in Figure 2.35. It is worth mentioning that 3% of water was not extractable during the AW100 oil tests, which was supposedly trapped inside the mass flowmeter.

Results shown in Figure 2.36 indicate that PV measurements are very close to stage measurements of 20%w and 30%w emulsion with slight deviation at 2500 rpm with 30%w (+15%). When water fraction increases to 40% however, the corrected viscosity appears to be much lower than the measured effective viscosity and the difference is higher as the ESP rotational

speed increases. From the figure we can also observe that the effective viscosity sometimes increases or decreases as mass flowrate increase. However, low flowrates data should not be relied much on, since the flow loop most likely have a wide range of temperature which leads to uneven physical properties throughout the flow loop. Although Figure 2.35 shows that the effective viscosity is independent of mass flowrate, this may not be the case due 2 possible reasons. First, a slight change in viscosity cannot be captured by the stage boosting pressure. Second, the ESP average temperature may not represent the stage temperature, and hence, oil viscosity at the stage might be inaccurately correlated.

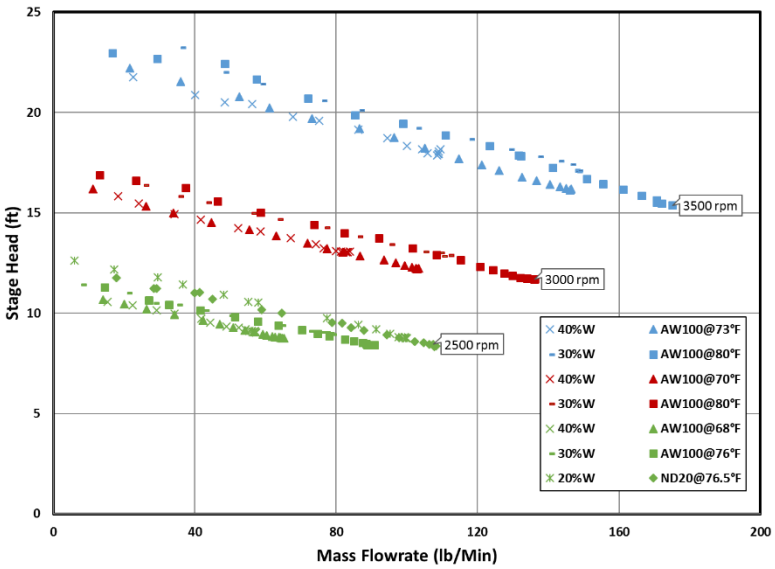

Figure 2.35 Matching pump head of single phase oil to emulsion

With AW100 oil at around freezing ambient temperatures, high viscosity values were not controllable since the ESP heating rate is higher than the heat exchanger cooling rate for all 3 rotational speeds, in order to match the head at 50%w emulsion. Few points were successfully captured that matched the two-phase head as shown in Figure 2.37. The matched viscosity for 3500 rpm is around 241 cP which is expected since the performance of 50% water fraction is better than that for 40% water fraction as discussed in Figure 2.21.

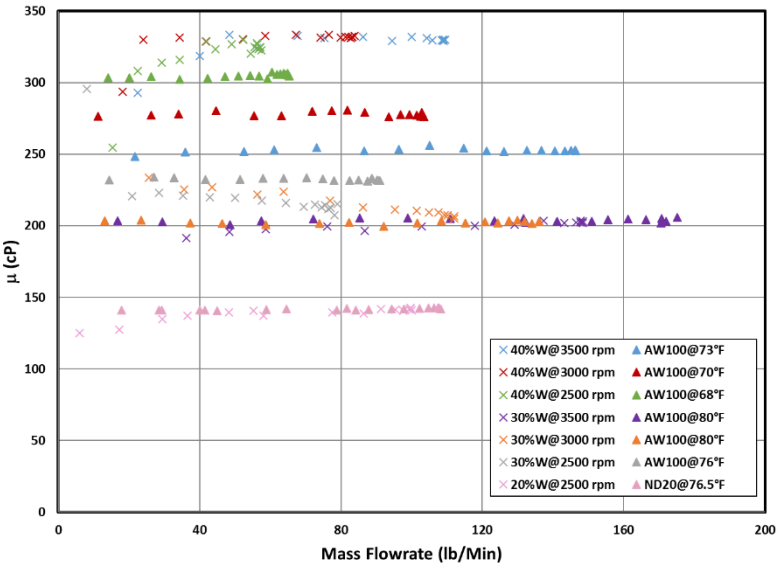

Figure 2.36 Emulsion effective viscosity and single oil viscosity

However, this value is more than 50% lower than that derived for emulsion as shown in Figure 2.38 and much lower compared to the matched viscosities for the other rotational speeds. The figure also shows when water fraction is higher than 30% or whenever the corrected viscosity is higher than 250 cP, the effective viscosity difference between the PV and the ESP stage conditions becomes significant and it is worse with rotational speed increase.

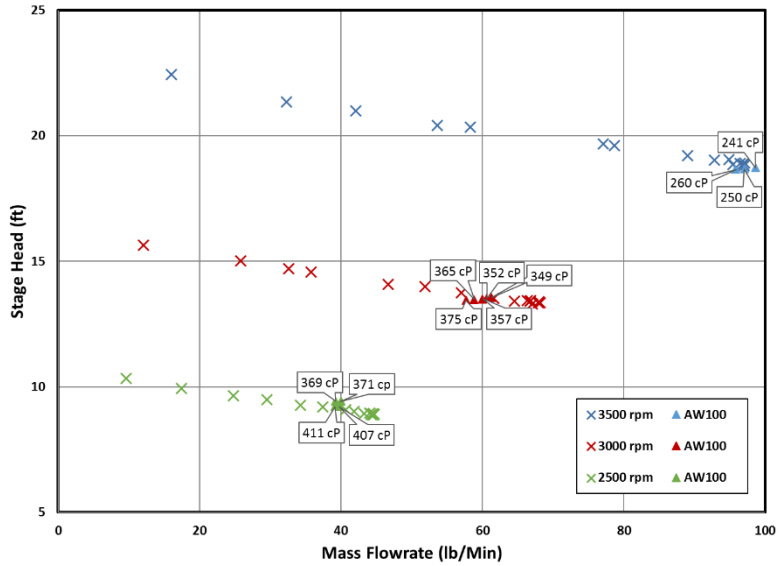

Figure 2.37 Matching head of single phase oil to head of 50%w emulsion

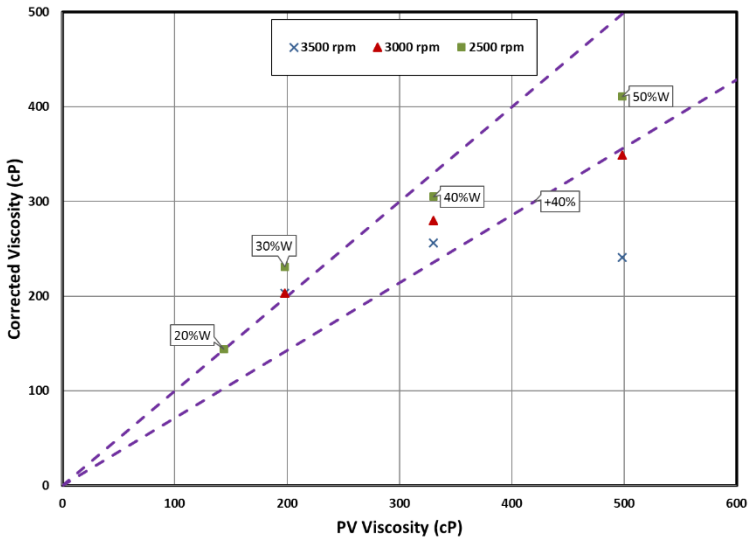

Figure 2.38 Corrected emulsion viscosity

2.3.2.4 FBRM and PVM Probes Feasibility Test: Focused Beam Reflectance Measurement (FBRM) and Particle Video Microscope (PVM) are the two options considered to monitor dispersed droplet size. The objective was to investigate the droplet size distribution and find its relationship with other parameters such as viscosity, rotational speed, flowrate, and temperature. The FBRM probe functions by sending and receiving laser beams to measure the droplet chord length as shown in Figure 2.39. It can detect droplets between 0.5 and 2000 μm. The PVM consists of six-near IR lasers which illuminate a small area in front of the probe face. Similar to Figure 2.40, the probe records the images even in dark and concentrated suspensions or emulsions in real-time and droplets between 2 and 1000 μm can be detected.

In order to assess the feasibility of these probes for our experiments, a two-day test is conducted. FBRM and PVM probes are installed in series 1 ft downstream of the ESP with 1 ft spacing, positioned against the flow direction at 45° as shown in Figure 2.41, for four sets of experiments. The purpose for the feasibility test was to compare results from both probes and

decide which one can be used for our need. From fluid mechanics prospective, as rotational speed increases, shear rate increases, and therefore dispersed droplets become smaller and emulsion apparent viscosity becomes higher. At the same time, higher shear rate reduces the emulsion effective viscosity, especially for water fraction close to the inversion point. As flowrate decreases, the coalescence time becomes longer for the dispersed droplets between the ESP and the probes, which causes larger droplets to form.

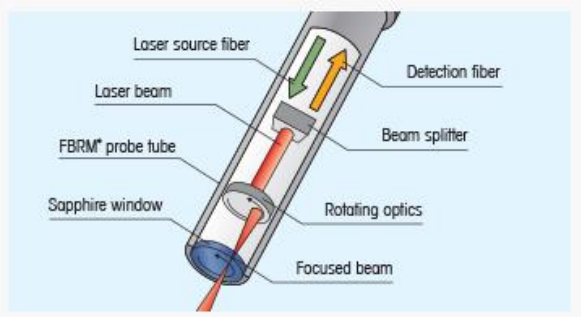

Figure 2.39 FBRM principle

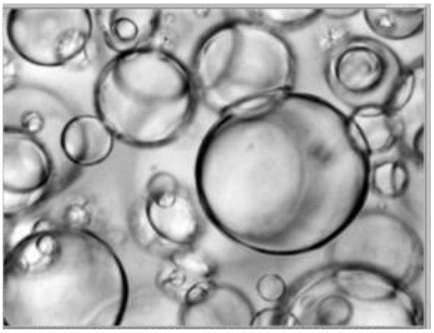

Figure 2.40 Typical PVM image

Figure 2.41 FBRM and PVM probe setup

Unfortunately, the PVM probe cannot handle high viscous fluid (>400 cP) since it sticks on the probe surface and prevents the probe from capturing clear images after a short time of circulation. Hence, only FBRM test results are analyzed as shown in Figure 2.42. Data for 45% water show that droplets become smaller as rotational speed increases, which is physically meaningful, but the effective viscosity kept almost constant which is unexpected. For 55% water, different rotational speeds did not affect droplet size neither the effective viscosity, which is also unexpected. These experiments correspond to continuous oil and dispersed water, close to the inversion point. Due to the vague results, we decided not to invest in these probes for this study, but there is a possibility for other studies in the future to use these probes at different flow conditions.

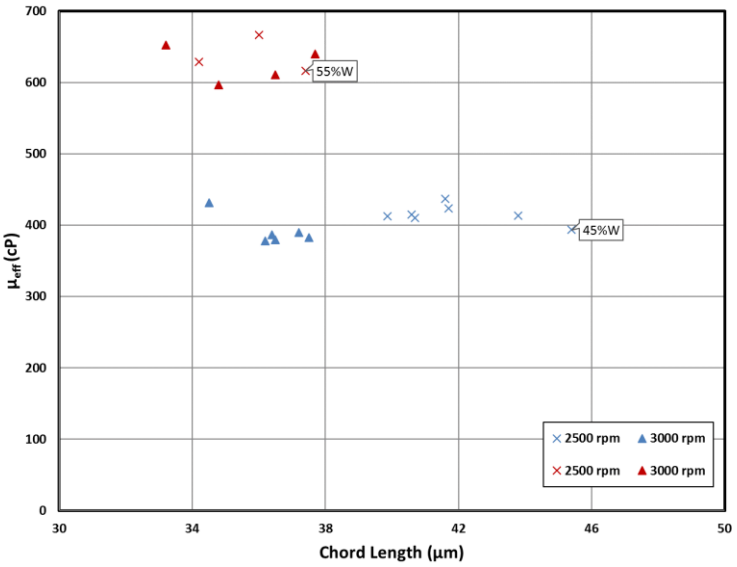

Figure 2.42 FBRM feasibility test results

Most of the available correlations in the literature are for stirrers or Rushton turbines, in which usually the rotation speed does not exceed 500 rpm. A model for estimation of the droplet size of the dispersed phase is evaluated, hoping that it can be extended to other untested cases. Kolmogorov (1949) presented a model for droplet size in turbulent flow based on the balance

between stress and interfacial tension. He proposed that stresses can be balanced by either inertial or viscous stresses present in turbulent flow. For high Reynolds numbers, "inertial subrange" presents where inertial stresses dominate over viscous stresses. As Reynolds number decreases, viscous effects become dominant in the "viscous subrange" as shown in Figure 2.43. As a result, maximum stable droplet size can be either in the inertial subrange or the viscous subrange (Boxall et al. 2012). Sensitivity analysis for our case shows that with the oil we have, the viscous forces dominates the stress so that only the equations used for the viscous subrange will be used to obtain the average droplet size.

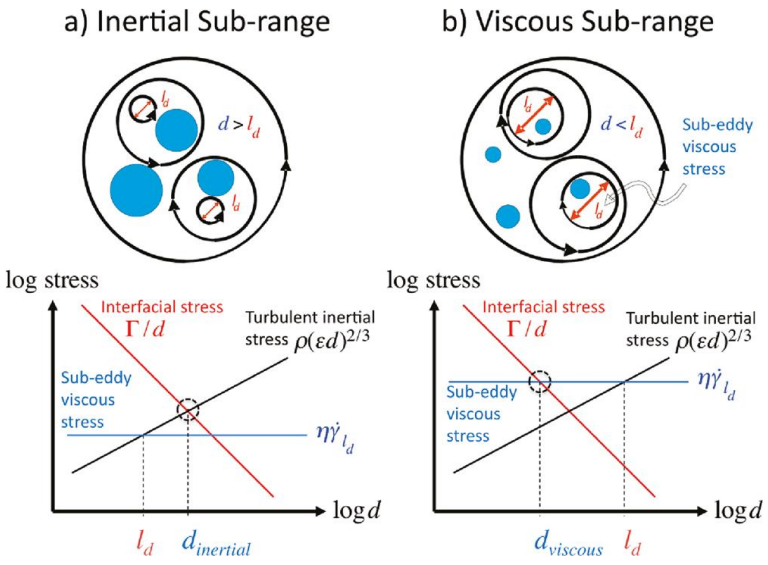

Figure 2.43 Inertial subrange and viscous subrange (Boxall et al. 2012)

Conventionally, dimensionless numbers: Weber number and Reynolds number have been used in order to estimate the droplet size. The definition for each parameter in case of "stirred tank" is as follows:

$$Re_{Tank} = \frac{\rho N D^2}{\mu} \tag{2.25}$$

$$We_{Tank} = \frac{\rho N^2 D^2}{\sigma} \tag{2.26}$$

where ρ is the continuous phase density (kg/m^3), N is the rotational speed (1/s), D is the blade length (m), μ is the continuous phase viscosity (Pa·s), and σ is the interfacial tension (N/m). The author conducted experiments on different crude oils with different viscosities and one crude happens to have viscosity close to the oil viscosity used for the FBRM feasibility test in this work. Therefore, we used this correlation to estimate the droplet size in our case, specifically to the conditions which we have measured values for droplet sizes from the FBRM results discussed earlier. The correlation for the subrange of our interest is:

$$\frac{\bar{d}}{D} = 0.016 Re^{1/2} We^{-1} \tag{2.27}$$

Given: Oil viscosity = 0.097 Pa·s, Oil density = 879 kg/m^3, Blade length = 0.039 m, Interfacial tension ≃ 0.0367 N/m, results are in the following table:

Table 2.2 Correlation vs. FBRM results for mean droplet diameter

Rotation Speed (Hz)	**We**	**Re**	**$\bar{d}$ (μm)**	**PVM Measured Diameter (μm)**
41.67	2467	574	6.06	37.4
50	3552	689	4.61	37.5

We can see significant discrepancy in the estimated values compared to the measured values. Clearly, this model has some limitations and differences from our application. First, flowrate is not considered since this model is for mixer tanks where flow is stagnant. Second, rotation speed did not exceed 500 rpm in the mixer tank study while in our case it is at least 2000 rpm. Third, the volumetric fraction of each phase is not considered, which is a drawback in this model. Lastly, the geometry in the mixer tank compared to the ESP stage seems to be similar but there are a lot of differences, such as the blade shapes and angles and not having a diffuser in the mixer tank. Thus, this model has to be improved to consider these factors.

2.4 Sampling

Sampling is critical in order to verify the oil and water fractions and to ensure the least possible gas entrapment in the flow loop. At the end of each experiment, a sample is collected while the flow is running so that the sample is representative. In Croce (2014) study, the sampling point was located under the filling point. In order to minimize pressure loss, control temperature easier and achieve high flowrates, the PVC section is bypassed once the desired water fractions and intake pressure are achieved. On the other hand, sample is extracted right after the choke valve at the elbow, after discarding some volume so that the collected fluid is from the flowing part.

Once the sample is collected, the total volume is recorded. Segregation sometimes starts immediately but we wait for a certain period of time (at least 1 day) until each phase is fully separated depending on the tightness of the emulsion. Figure 2.44 shows the phase segregation after 24 hours, but clearly the time was not sufficient for the phases to be fully separated. It is also observed that the total volume decreased from 188 ml to 161 ml due to gas entrainment in the loop and gas dispersion during sampling. The change in the air-liquid interface level is due to the rising of the gas bubbles through the emulsion. Estimating the entrained Gas Volume Fraction (GVF) is unreliable by sampling at the atmospheric pressure, since there might be some gas escapes from the sample or entrains the sample during the sampling process. For single phase oil or water, it is almost impossible to drain all the previous liquid since some liquid volume stay inside the U-shaped mass flowmeter. Impurities can also affect the accuracy of the density measurements. Therefore, GVF cannot be estimated from the density measurement at the mass flowmeter, since there are 3 phases, or 4 phases in case of impurities exist.

Figure 2.44 A sample 1 minute after collecting (left) and 1 day (right)

Gravity separation sometimes does not work very well, so the sample is transferred to a beaker without the water (only the oil and the emulsion) then the beaker is heated so that water evaporates out of the emulsion and the remaining volume is 100% oil. We noticed that while heating the emulsion and oil up, the color changes from light brown to dark brown, indicating that water is being separated by evaporating from the emulsion. Figure 2.45 shows the heated sample has almost the same color compared to pure ND20 color, small difference in color may be due to contamination in the flow loop. Finally, the resulted values of oil and water fractions should replace the estimated values from the flowmeter density measurement.

Figure 2.45 Pure oil (left) and remaining used oil after heating (right)

2.5 Experiment Summary

Once the loop starts to run, emulsion starts to form and temperature increases as a result of mechanical energy loss which is converted into dissipated heat. After the desired temperature is reached, the heat exchanger is used to stabilize the ESP average temperature. In that case, it is always observed that there is no change in any of the parameters such as differential pressure, mass flowrate, and density. The steady differential pressure indicates that the emulsion has reached its most equilibrium state in the loop. Figure 2.46 is the experiment summary of effective viscosity values for emulsion with the old batch of ND20, which are obtained from the highest flowrates since that should have the most stable conditions in terms of mass flowrate, pressure drop, and temperature. The figure also shows the validated viscosities using AW100 oil when the ESP stage performance was matched with the ND20 emulsion stage performance. While the PV shows the effective viscosity independence on the rotational speed as discussed earlier in Figure 2.30, we can clearly observe that rotational speed causes the effective viscosity to be lower when it increases, with clear observation when getting closer to the inversion point, i.e. at 51% of water fraction.

Many models in the literature were developed to predict the effective viscosity of two phase mixture with different limitations and the selected ones in this study are listed in Table 2.3. Einstein (1911) relationship is based on suspension behavior in the dilute system so it is applied up to 25% of the dispersed phase. Compared to our experimental data, all models over predict the new ND20 emulsion effective viscosities except Yaron and Gal-Or (1972) which at first matches the experiment viscosities but then deviated, as shown in Figure 2.46. Data from the FBRM probe feasibility test are also shown in the figure. We can also estimate the inversion point to be between 55% and 60% of water with an effective viscosity about 6 times higher than oil viscosity.

Table 2.3 Mixture effective viscosity models

Author	Model
Einstein (1911)	$\mu_m = (1 + 2.5\phi)\mu_o$
Guth and Simba (1936)	$\mu_m = (1 + 2.5\phi + 14.1\phi^2)\mu_o$
Vand (1948)	$\mu_m = e^{\left(\frac{2.5\phi}{1-0.609\phi}\right)}\mu_o$
Brinkman (1952)	$\mu_m = (1-\phi)^{-2.5}\mu_o$
Krieger (1972)	$\mu_m = \left(1 - \frac{\phi}{\phi_{max}}\right)^{-2.5\phi_{max}} \mu_o$
Yaron and Gal-Or (1972)	$\mu_m = \left\{1 + \phi \frac{5.5\left[4\phi^{\frac{7}{3}} + 10 - \left(\frac{84}{11}\right)\phi^{\frac{2}{3}} + \left(\frac{4}{K}\right)\left(1-\phi^{\frac{7}{3}}\right)\right]}{10\left(1-\phi^{\frac{10}{3}}\right) - 25\phi\left(1-\phi^{\frac{4}{3}}\right) + \left(\frac{10}{K}\right)(1-\phi)\left(1-\phi^{\frac{10}{3}}\right)}\right\}\mu_o$

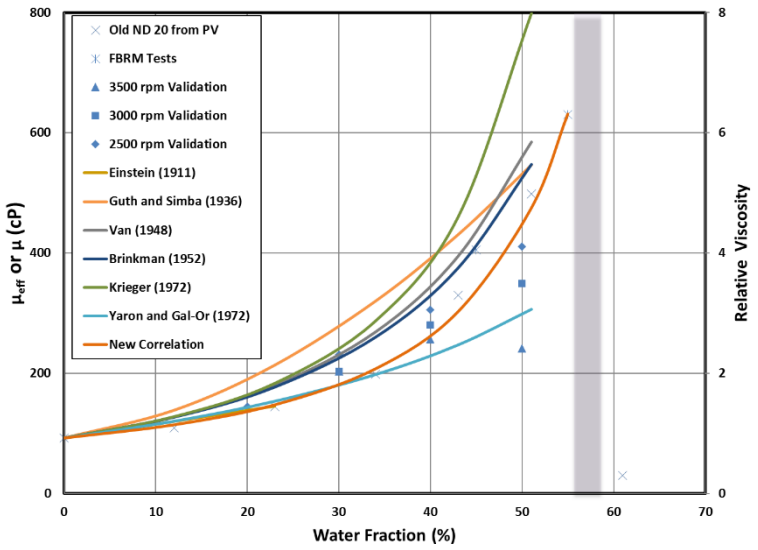

Figure 2.46 Emulsion effective viscosity for old ND20 oil at 88 °F

Figure 2.47 shows the summary of experiments conducted for the new batch of ND20 oil emulsion at three different temperatures with a combined error of ±0.1871%. For all cases, the inversion point is around 20% of water fraction, with effective viscosity about two times higher than oil viscosity, which is lower compared to the old ND20 emulsion effective viscosity around

inversion point. The inversion point at a much higher water fraction for the old ND20 oil may be caused by contamination of the oil. Since water becomes the continuous phase at 25% of water fraction for 80 °F and 88 °F, there is no need to conduct experiments at that water fraction for 100 °F, since instability is expected similar to that shown earlier in the PV results in Figure 2.31. Viscosity validation experiments were not conducted for this set of results, since the deviation between the PV and stage viscosities is negligible for viscosities lower than 200 cP as shown in Figure 2.38.

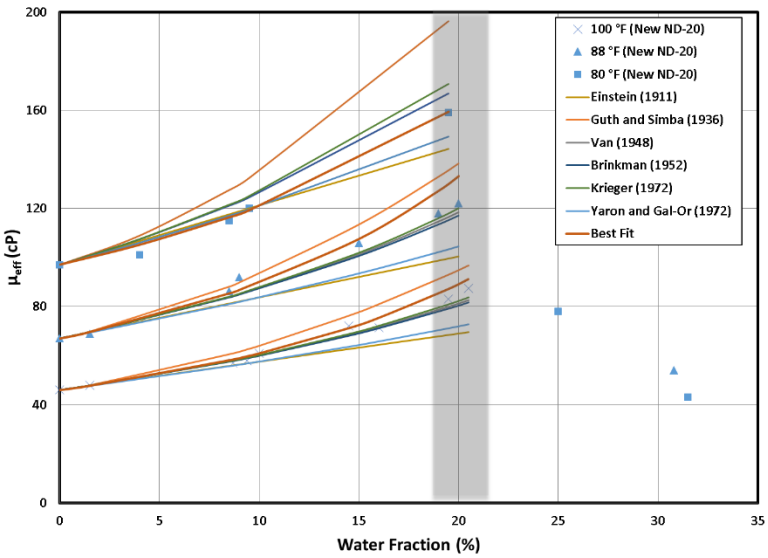

Figure 2.47 Emulsion effective viscosity for new ND20 oil

Results for emulsion with the low viscosity oil Isopar V are shown in Figure 2.48. Clearly, we can notice the narrow range of viscosity change as water fraction increases. However, considerable deviations in the prediction models from measurements are observed and all of them under predicts the effective viscosity values.

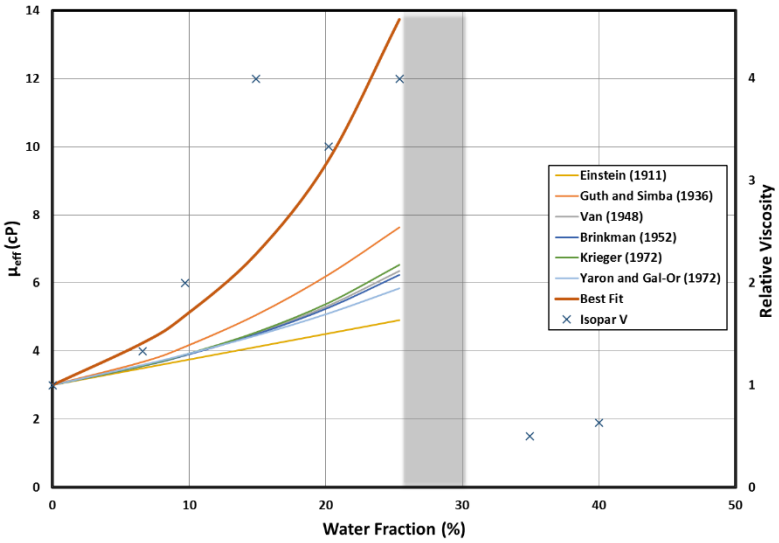

Figure 2.48 Emulsion effective viscosity for Isopar V

A thorough experimental investigation of DN-1750 ESP performance under viscous flows of both single-phase liquid and oil-water flows has been conducted. Effects on ESP boosting pressure with emulsion are studied, including oil and water fractions, rotational speed with two different mineral oils of medium and low viscosities. Experimental results of ESP stage pressure increment under tap water flow deviates from catalog head curves but reasonably matches previous studies, which validated the experimental setup used in this study.

CHAPTER 3

THREE-DIMENSIONAL CFD SIMULATION

In this study, the 3D numerical simulations are conducted for single-phase water or viscous oils and water-in-oil flows through a rotating ESP. The commercial software package ANSYS CFX 15 is used to perform the CFD simulations. The numerical configurations including computational domain, grids, mathematical models, and boundary conditions are set in CFX-pre. The Navier-Stokes (N-S) equations are solved iteratively by CFX-solver until the convergence is achieved. Finally, the simulation results are presented in CFX-post, including fields of velocity and pressure. Viscosity effect simulations are conducted with two different approaches. The first is by simulating single channels for 7 consecutive stages then results are compared with the experimental ESP average pressure increment. The second approach is simulating 3 full stages then compare the results of the third stage to the third stage performance in experiment.

3.1 CFD Simulation of Viscous Fluid Flow

For 3D numerical simulations of viscosity effects on ESP boosting pressure, the steady-state Reynolds-Averaged-Navier-Stokes (RANS) equations with standard SST (shear stress transport) turbulence models are solved by employing the frozen-rotor technique. The simulated geometry includes 7 stages, exactly the same configuration used in experiments. Each stage comprises of a channelwise-sliced impeller and diffuser, on which the structured hexahedral grids are generated with Turbogrid 15.

3.1.1 DN-1750 ESP Geometry and Mesh

DN-1750 is a mixed-type ESP with N_S = 2738 at the beginning of its life. There are 6 blades and 8 vanes in impeller and diffuser, respectively. The geometrical specifications are listed in Table 3.1. At the best efficiency point (BEP), the operation parameters are as follows: rotational speed N = 3500 rpm, mass flowrate Q = 3.3 *kg/s* (1795 bpd), hydraulic head H = 5.7 *m* (8.11 psi), and efficiency η = 68.5 %.

Table 3.1 Geometrical specifications of DN-1750 ESP

Component	Description	Parameter	Values
Impeller	Blade number	Z_i	6
	Tangential blade angle at inlet (deg)	β_1	20.3
	Tangential blade angle at outlet (deg)	β_2	36.2
	Blade thickness (mm)	b_i	1.7
	Channel length (mm)	l_i	39
	Inlet channel height (mm)	h_1	13.5
	Outlet channel height (mm)	h_2	7.13
	Inner radius (mm)	r_1	19.9
	Outer radius (mm)	r_2	33.7
Diffuser	Vane number	Z_d	8
	Channel length (mm)	l_d	51.9
	Partition wall thickness (mm)	b_d	3.1

Figure 3.1 displays the DN-1750 ESP 3D model, including impeller blades (Figure 3.1a), diffuser vanes (Figure 3.1b), and the entire single-stage assembly (Figure 3.1c). Since the flow fields inside centrifugal pump are axisymmetric (Zhu and Zhang, 2014), a single channel is used to save computational cost (Caridad et al., 2008). Thus, the computational domains of impeller and diffuser can be streamwisely sliced into 1/6 and 1/8 as shown in Figure 3.2(b) and (c), respectively. Similar configurations were numerically implemented on a three stage radial-type ESP to study pump two-phase performance under gas-liquid flow conditions (Zhu and Zhang, 2014 and 2017). In this study, the ESP flow domain comprises of 7 stages which are assembled in

series (see Figure 3.2a). The single-stage pressure increment is obtained by calculating the pressure difference between the inlet and outlet of stage 3, while the simulated overall boosting pressure of the ESP is obtained by subtracting total pressure at the inlet of stage 1 from total pressure at the outlet of stage 7.

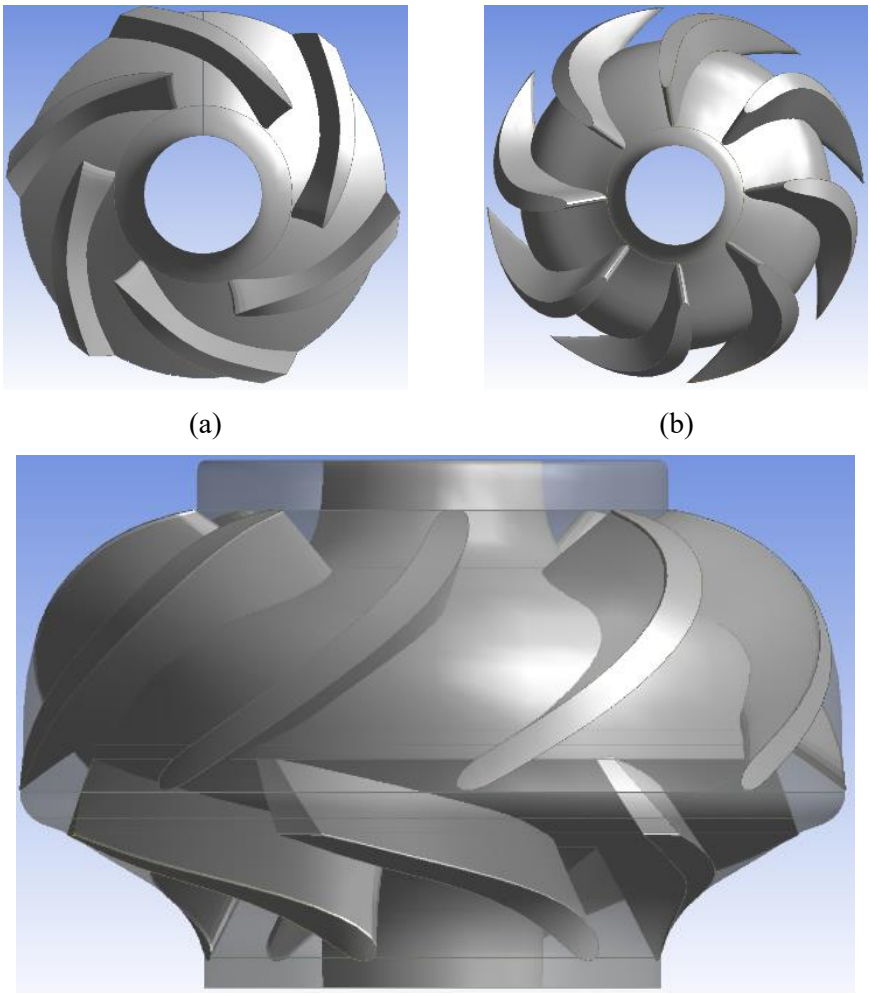

(a) (b)

(c)

Figure 3.1 Geometries of a single stage DN-1750, (a) impeller blades, (b) diffuser partitions, (c) entire 3D assembly

Due to complex pump geometry, the generation of 3D unstructured mesh of tetrahedrons is easier compared to structured mesh comprising of hexahedrons. It is a trade-off when selecting the proper mesh type to conduct CFD simulations. The unstructured mesh is mostly composed of

non-orthogonal grids and jeopardizes the regularity of data structure, which in turn compromises algorithmic accuracy and reliability. Therefore, the high-quality structured mesh generated with ANSYS Turbogrid 15 is adopted in this study. The structured hexahedral grids for simplified multistage geometry are shown in Figure 3.2, including a single flow passage of impeller (Figure 3.2) and diffuser (Figure 3.2c). Each domain is meshed with hexahedrons with the refinement near blade surfaces. The frozen-rotor technique is used to calculate interactions between impeller and diffuser within each stage. Impeller domains are set on a rotating frame of reference while diffuser domains are set on a stationary one. This approach is categorized as steady state simulation, which does not account for instantaneous effects in the flow field such as pump start up.

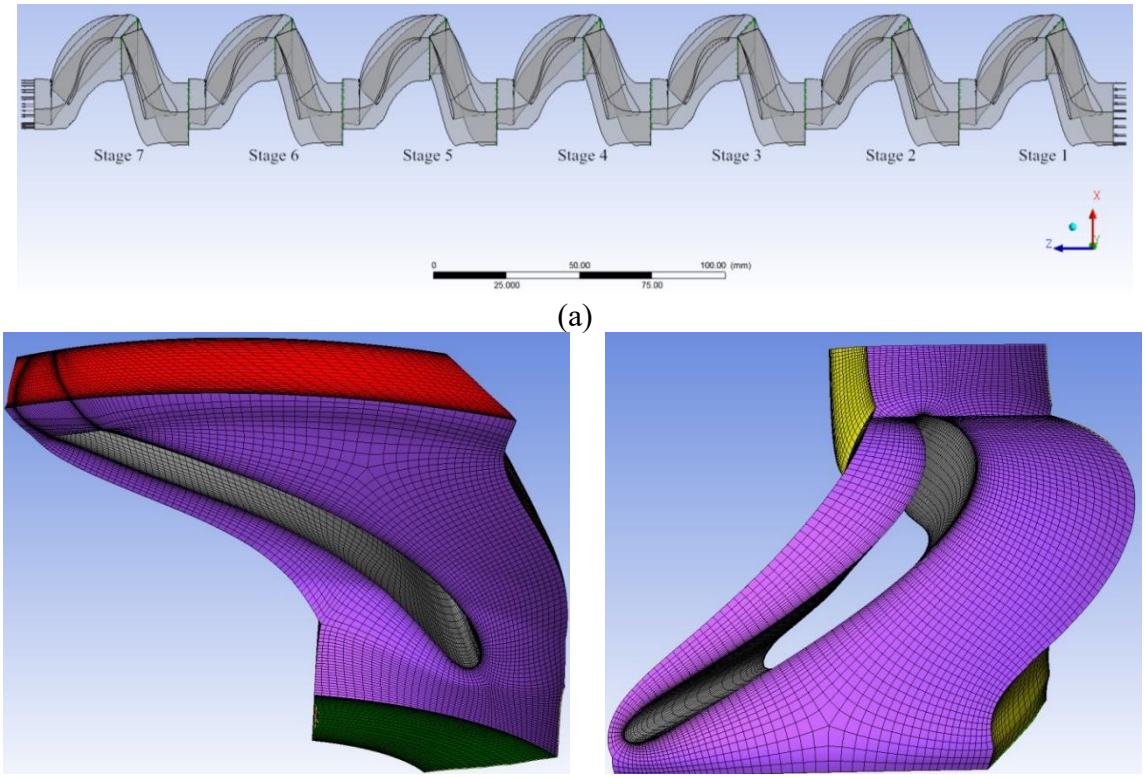

(a)

(b) (c)

Figure 3.2 Grid generation, (a) entire seven-stage assembly, (b) impeller channel mesh, (c) diffuser channel mesh

3.1.2 Governing Equations and Turbulence Model

In CFD simulation, a set of conservation equations are solved based on the continuous medium assumption, a fundamental hypothesis that treats fluid medium and motion infinitely differentiable in both time and space domains. In this study, the isothermal condition is applied to the fluid flow domain. Therefore, the conservation equation of energy can be omitted. The mass conservation equation is given by:

$$\frac{\partial \rho}{\partial t} + \nabla \cdot (\rho \vec{u}) = 0 \tag{3.1}$$

where ρ, $\vec{u}$ are the liquid density and velocity vector, respectively. The sink/source in mass conservation equation is not taken into account in this study. The momentum conservation equation, known as N-S equation, is written as:

$$\frac{\partial (\rho \vec{u})}{\partial t} + \nabla \cdot (\rho \vec{u}\vec{u}) = -\nabla P + \nabla \cdot (\bar{\bar{\tau}}) + \rho \vec{g} + S \tag{3.2}$$

where $\bar{\bar{\tau}}$ is the stress-strain tensor given in Equation (3.3), $\vec{g}$ is the gravity acceleration vector, S is external forces. For fluid flow in centrifugal pump, $S = S_{Cor} + S_{cfg}$. S_{Cor} and S_{cfg} represent the Coriolis force and centrifugal force effects. In stationary reference frame, $S_{Cor} = S_{cfg} = 0$. In a reference frame rotating with constant angular velocity (Ω), $S_{Cor} = -2\rho\vec{\Omega} \times \vec{V}$ and $S_{cfg} = -\rho\vec{\Omega} \times (\vec{\Omega} \times \vec{r})$, where $\vec{\Omega}$ and $\vec{r}$ are angular velocity vector and position vector, respectively.

$$\bar{\bar{\tau}} = \mu(\nabla \vec{u} + (\nabla \vec{u})^T) + \left(\lambda - \frac{2}{3}\mu\right) \nabla \cdot \vec{u}\bar{\bar{I}} \tag{3.3}$$

Equation (3.3) describes the shear stress tensor for Newtonian fluids. In this study, the working fluid is mineral oil, which is a Newtonian fluid. μ is fluid viscosity, λ is a second coefficient of viscosity, $\bar{\bar{I}}$ is the identity matrix. For turbulent flow, the instantaneous fluid velocity $\vec{u}$ can be decoupled as:

$$\vec{u} = \bar{u} + u' \tag{3.4}$$

where $\bar{u}$ and u' are time-averaged velocity and time-varying velocity fluctuation. Substituting Equation (3.4) into Equations (3.1) and (3.2) and rewriting them with indicial notation manner, we can obtain the so-called Reynolds-averaged Navier-Stokes (RANS) equations as

$$\frac{\partial \rho}{\partial t} + \frac{\partial}{\partial x_i}(\rho \overline{u_i}) = 0 \tag{3.5}$$

and

$$\frac{\partial (\rho \overline{u_i})}{\partial t} + \frac{\partial}{\partial x_j}\left(\rho \overline{u_i}\,\overline{u_j}\right) = -\frac{\partial P}{\partial x_i} + \frac{\partial}{\partial x_j}\left(\bar{\bar{\tau}}_{ij} - \rho \overline{u_i' u_j'}\right) + \rho g_i + S_i \tag{3.6}$$

Compared to Equation (3.2), there is one additional term $-\rho \overline{u_i' u_j'}$ added to the momentum conservation equation, which is known as Reynolds stress tensor. Reynolds stresses reflect the instantaneous convective transport due to turbulent velocity fluctuations which act to enhance mixing additional to that caused by thermal interactions at the molecular level. Several turbulence models are available in literature to model Reynolds stresses, including standard *k*-*ε* (Launder and Spalding, 1974), RNG (renormalization group) *k*-*ε* (Yakhot et al., 1992), standard *k*-*ω* (Wilcox, 1998), BSL (baseline) *k*-*ω* (Menter, 1994) and SST *k*-*ω* (Menter, 1994), among others. As recommended by ANSYS (2015), the SST *k*-*ω* two-equation turbulence model is applied here due to its ability of handling separation flow and resolving flow very close to walls. The Reynolds stress term $-\rho \overline{u_i' u_j'}$ is related to the mean velocity gradients based on the Boussinesq hypothesis,

$$\rho \overline{u_i' u_j'} = \mu_t \left(\frac{\partial u_i}{\partial x_j} + \frac{\partial u_j}{\partial x_i}\right) - \frac{2}{3}\delta_{ij}\left(\rho k + \mu_t \frac{\partial u_k}{\partial x_k}\right) \tag{3.7}$$

where μ_t is eddy viscosity or turbulent viscosity, which needs to be modeled further as function of *k* (turbulence kinetic energy) and *ε* (turbulence dissipation rate) or *k* and *ω* (specific dissipation rate). In this study, the SST turbulence model based on standard two-equation *k*-*ω* model is used since it incorporates the modifications for low Reynolds number effects, compressibility, and shear

flow spreading. Meanwhile, it also accounts for the transport of the turbulent shear stress and gives highly accurate predictions of the onset and the amount of flow separation under adverse pressure gradients (ANSYS, 2015). Thus, the turbulent viscosity,

$$\mu_t = \alpha^* \frac{\rho k}{\omega} \quad , \tag{3.8}$$

where α^* is an empirical coefficient to account for low Reynolds number effect, while it is equal to unity in high Reynolds number flow. To solve Equation (3.8) and compute μ_t, two additional transport equations for turbulence kinetic energy, k, and the specific dissipation rate, ω, are involved:

$$\frac{\partial(\rho k)}{\partial t} + \frac{\partial}{\partial x_j}\left(\rho k \overline{u_j}\right) = \frac{\partial}{\partial x_j}\left(\left(\mu + \frac{\mu_t}{\sigma_t}\right)\frac{\partial k}{\partial x_j}\right) + G_k - Y_k + S_k \tag{3.9}$$

and

$$\frac{\partial(\rho \omega)}{\partial t} + \frac{\partial}{\partial x_j}\left(\rho \omega \overline{u_j}\right) = \frac{\partial}{\partial x_j}\left(\left(\mu + \frac{\mu_t}{\sigma_\omega}\right)\frac{\partial \omega}{\partial x_j}\right) + G_\omega - Y_\omega + S_\omega \ , \tag{3.10}$$

where σ_t and σ_ω are turbulent Prandtl numbers for k and ω, respectively. G_k and G_ω are turbulence production terms. Y_k and Y_ω represent turbulence dissipation terms, D_ω represents the cross-diffusion term, and S_k and S_ω are user defined source terms. Equations 3.5 through 3.10 constitute the general form of SST k-ω turbulence model. More details regarding empirical correlations and coefficients in SST model can be found in ANSYS CFX-solver Theory Guide (2015).

3.1.3 Boundary Conditions and Numerical Scheme

Two types of interfaces are used in CFD simulation. The general connection interface model is employed in each pair of impeller and diffuser interfaces, which can apply a frame change and connect non-matching grids. Totally, 13 pairs of general connection interfaces are generated. 7 of them are within stages, and the remaining 6 pairs are located at inter-stages. Periodic interfaces

based on circumferential periodicity are set within each domain of impeller or diffuser, resulting in 14 pairs of periodic interfaces.

The frozen-rotor algorithm is used to simulate interactions across the interfaces of impellers and diffusers. This model treats each component of computational domain with an individual frame of reference, while it keeps the relative orientation of these components across the interface fixed. It requires the least amount of computational effort compared to other interface models. However, the frozen-rotor model is unable to capture transient effects at the frame change interface due to its steady state nature. In our simulation, the axisymmetric property of ESP geometries is used by assuming periodic flow characteristics if pump working condition is stable. The streamwise-designed blades and vanes inside ESP provide additional compensation that further weakens interactions across impeller-diffuser interfaces. Thus, the frozen-rotor algorithm is used as it offers an acceptable compromise between computational effort and numerical efficiency.

Due to the simplified geometries of impeller and diffuser, the grids at interface are non-conformal and mismatching with different pitch angles. In consideration of this, the GGI (general grid interface) mesh connections are employed, which permit non-matching of grids on either side of the two connected surfaces (ANSYS, 2015).

Boundary conditions are specified according to the corresponding experimental configurations from ESP inlet to outlet. For wetted walls, the no-slip velocity condition is imposed. As pointed out by Li (2014), the wall roughness is estimated by equivalent sand-grain roughness h_S. The dimensionless number h_S^+ is defined as

$$h_S^+ = h_S \frac{\sqrt{\tau_W/\rho}}{\nu} \tag{3.11}$$

The range $h_S^+ \leq 5$ corresponds to hydraulically smooth regime, $5 < h_S^+ \leq 70$ corresponds to transition regime, and $h_S^+ > 70$ for hydraulically rough regime. The standard wall function holds only within hydraulically smooth regime. Thus, special attention needs to be paid to near wall treatment in turbulence model with low-*Re* flow and rough walls. In this study, the near-wall treatment is automatic wall functions for omega-based turbulence models. It automatically switches from standard wall-functions to a low-*Re* near wall formulation as the mesh is refined. We apply a simple correlation of h_S with arithmetic average of absolute values of real roughness Ra by h_S = 6 Ra (Li, 2014). For a cast wall, Ra = 12.5 ~ 50 μm. Using Ra = 50 μm, one can obtain h_S = 300 μm, which is close to 250 μm, a sand equivalent roughness of the natural surface of cast iron recommended by Patankar et al. (1972).

The total pressure with zero gradient flow direction and turbulence intensity is set at the first stage inlet. A mass flowrate scaling down to 1/8 of inner cross-sectional area is imposed at the 7th stage outlet. This is a more robust configuration of boundary conditions for numerical convergence as recommended in ANSYS (2015), especially for part-load CFD simulation (Stel et al., 2015).

All simulation cases are conducted with the same numerical schemes. For discretization of advection terms and turbulence equations in space, the high resolution scheme is used, which is a second order algorithm in ANSYS CFX-solver. For steady-state simulation, a false time step as a means of under-relaxing governing equations is applied, which allows a relatively large time scale due to robust and fully implicit CFX-solver. A fixed physical timescale of $\frac{1}{2\Omega}$ is used with maximum 500 outer loop iterations to achieve convergence. The convergence criterion is satisfied if RMS (root mean square) residual drops below 10^{-4}.

3.1.4 Results and Discussions

In this part, the numerically simulated ESP boosting pressures are presented and compared with experiment results under different flow conditions. At first, CFD simulations is compared with experimental results for water flow to validate numerical methodology. Then, experimental conditions of viscous oil flows are incorporated into numerical simulations as inputs. The outputs from CFD-post include pump pressure increment, streamline, pressure and velocity fields etc. Four rotational speeds and four oil viscosities are used to conduct experiments and numerical simulations, namely, 3500, 3000, 2500, 2000 rpm and 56, 98, 180, 220 cP.

3.1.4.1 Mesh Independence Check and Turbulence Model Validation: The mesh quality depends on the dimensionless distance (y^+) at the first grid point near the wall. According to boundary layer theory, the viscous sublayer exists in the near-wall region. Within viscous sublayer, the dimensionless velocity (u^+) is a logarithmic function of y^+ away from the wall. This is also referred to as standard wall-function, which holds for $y^+ < 100$. Thus, the first grid layer should be sufficiently fine to meet wall function requirement.

The mesh number is counted on single-stage simplified fluid domains of impeller and diffuser. As shown in Figure 3.3, the simulated stage pressure increment becomes constant when the grid number reaches about 0.2 million, where the average value of y^+ on blade surface is below 30. Therefore, the grids used for simplified impeller and diffuser sections consist of 158,976 and 124,296 elements, respectively. Total grids for the complete seven-stage computational domain contain 1,982,904 elements, which are sufficient to guarantee grid independence.

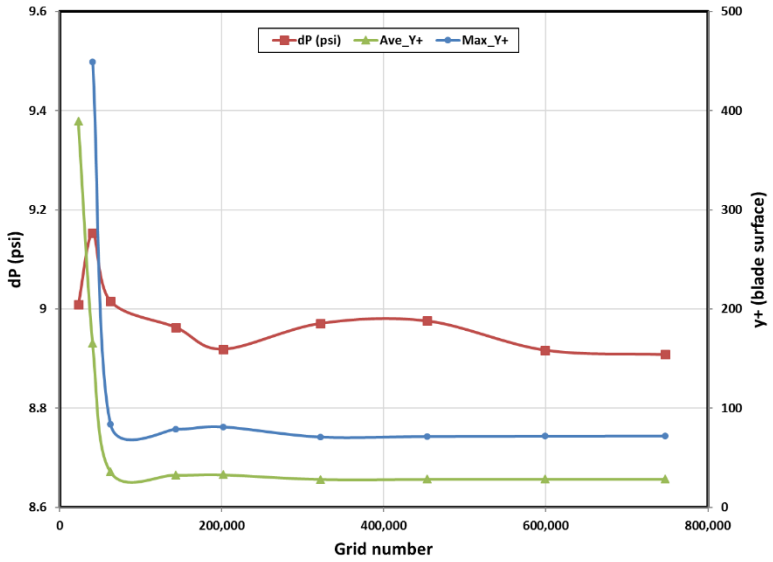

Figure 3.3 Mesh validation and wall function check for single-phase CFD simulation on DN-1750 ESP

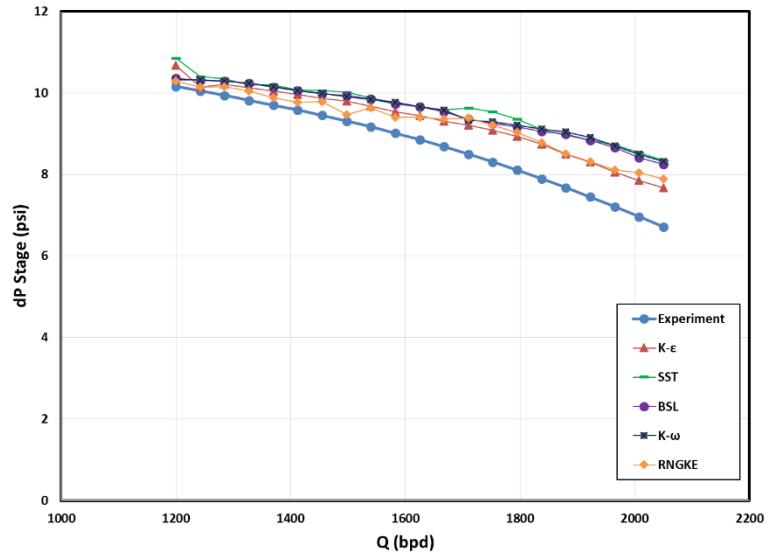

Figure 3.4 Influence of turbulence models on single-phase CFD simulation of DN-1750 ESP under water flow

Figure 3.4 shows the effect of turbulence models on simulated stage pressure increment and comparison with corresponding experimental results under water flow. The selection of turbulence model is a delicate task for CFD simulation, which is also a compromise of computational effort and numerical accuracy. As it can be seen in the figure, there is no prominent

variance among different turbulence model predictions. However, the aforementioned SST turbulence model is used due to its advantages in capturing shear flow spreading and separation at low Reynolds number flow.

3.1.4.2 Comparison with Catalog Curves: For comparison of simulated ESP boosting pressure with experimental data, the dimensionless variables: flow coefficient, head coefficient, and hydraulic efficiency are defined by Equations (3.12) through (3.14):

Flow coefficient:

$$\varphi = \frac{Q}{\Omega D_i^3} \tag{3.12}$$

Head coefficient:

$$\psi = \frac{gH}{\Omega^2 D_i^2} \tag{3.13}$$

Hydraulic coefficient:

$$\eta = \frac{Q\Delta P}{T\Omega} \tag{3.14}$$

where T is shaft torque, and Ω is ESP rotational speed.

Figure 3.5 shows the comparisons of single-phase simulation results of head coefficient (ψ), pump efficiency (η) as function of flow coefficients (φ) with the catalog curves within the pump operation range. A good agreement can be seen for ψ versus φ. However, the simulation results for η are slightly higher than the catalog curve, indicating that CFD simulation over predicts ESP single-phase efficiency. This may be due to the neglect of leakage flow through the radial clearance between impeller and diffuser, which causes additional boosting pressure loss in reality. Meanwhile, the smooth wall assumption also contributes to the deviation by underestimating wall shear stresses.

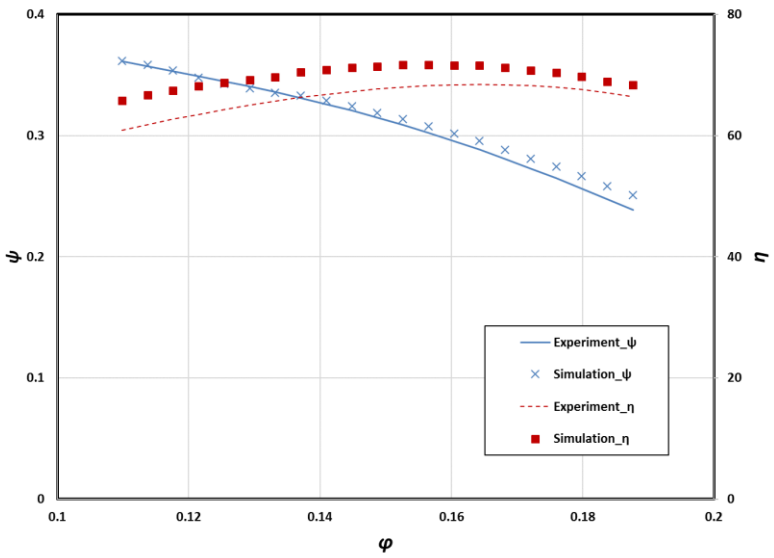

Figure 3.5 Comparison of numerical results with catalog curves

3.1.4.3 Comparison with Experimental Data: Figure 3.6 and Figure 3.7 show the comparison between experimental results and numerical simulations for ESP overall pressure increment over 7 stages. The experimental tests were conducted by Banjar (2013) and Zhu et al. (2016). The measurements were taken with the differential pressure transducer spanning from the inlet of the first impeller to the outlet of the 7th diffuser. The corresponding numerically simulated pressure increment is calculated as

$$\Delta P = P_{stat,2} - P_{stat,1} + \frac{1}{2}\rho\left(\vec{C}_2^2 - \vec{C}_1^2\right) \qquad (3.15)$$

where P_{stat} is static pressure, $\vec{C}$ is absolute velocity given by $\vec{C} = \vec{W} + \vec{U}$ according to velocity triangle. $\vec{W}$ and $\vec{U}$ are relative and peripheral velocities, respectively. Subscripts 1, 2 are for inlet and outlet.

In Figure 3.6, a good agreement can be found in the comparison for water. However, numerical simulation over predicts ESP boosting pressure of viscous oils with an error about 15% as shown in Figure 3.7. As viscosity increases, the pressure increment decreases. At higher

viscosity and lower flowrate, the trend becomes more linear, indicating that the flow regime changes from turbulent flow to laminar flow. Figure 3.8 shows the slight deviation of the simulated ESP boosting pressure from the experimental results and sometimes it reaches beyond 20%. The deviation may be partially due to pump's rusty and worn conditions after years of experimental tests.

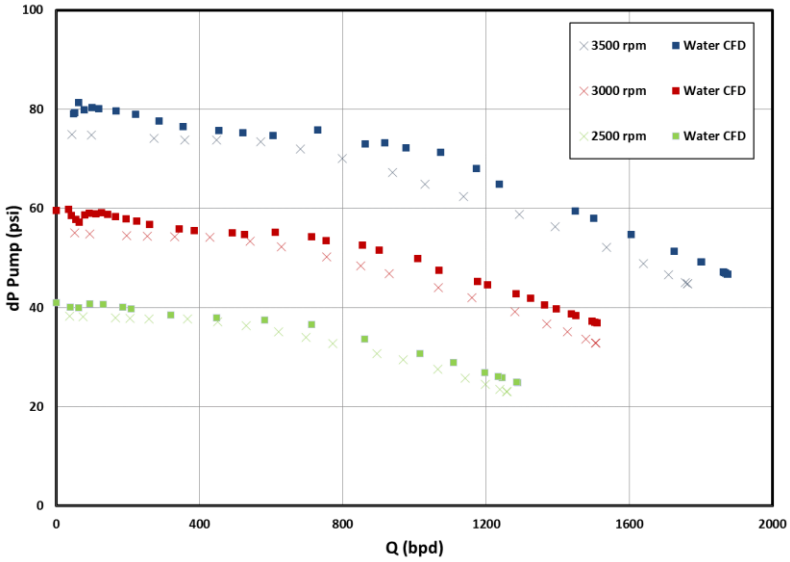

Figure 3.6 Comparison of CFD simulated ESP performance with water experimental results

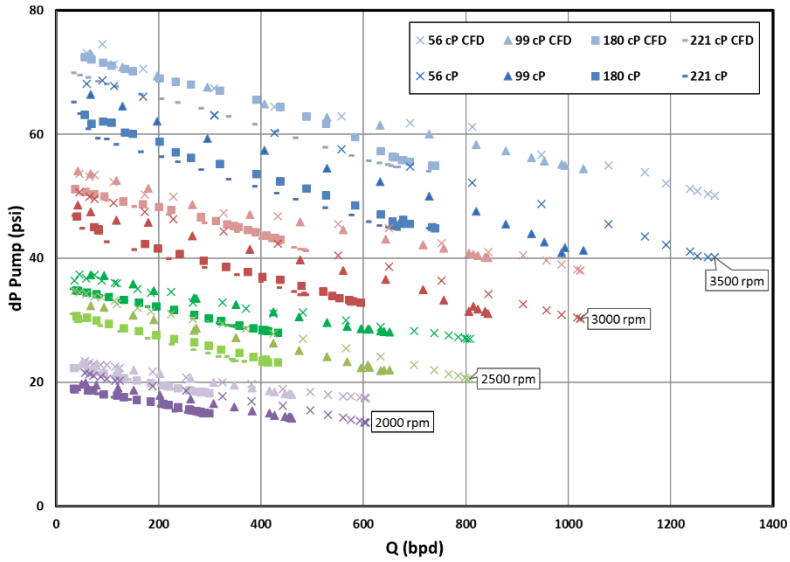

Figure 3.7 Comparison of CFD simulated ESP performance with oil experimental results

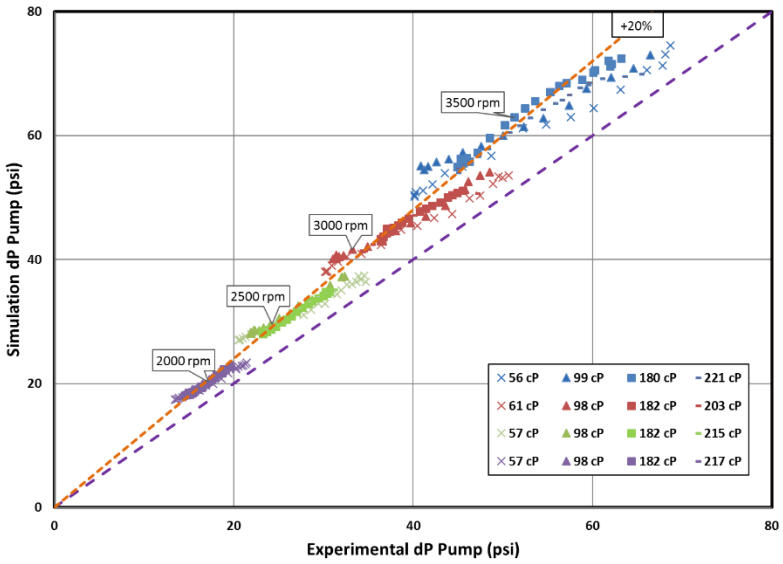

Figure 3.8 ESP dP simulation results deviation from experimental

3.1.4.4 Analysis of Flow and Pressure Fields: Figure 3.9 shows the streamline plots under different flow conditions in the 3rd stage. The recirculation flow that contributes to the pump hydraulic loss is observed near the trailing edges of impeller blades. Two hydraulic factors affect the recirculation flow from the comparison in Figure 3.9. First, due to high viscosity, the flow regime shifts from turbulent flow to laminar flow, causing changes of flow recirculation inside impeller (Figure 3.9(b), (d) and (f)). Second, under off-design operation conditions, the fluid velocities at the outlet of impeller deviate from blade angle increasingly. This in turn leads to additional departure of streamlines from the designed flow path. Therefore, further recirculation and pressure potential dissipation is induced (Figure 3.9(a) vs. (b), (c) vs. (d)).

For the simulated cases shown in Figure 3.9, the vortices exist near the pressure sides of diffuser vane due to highly curved vane geometry. The vortex shape inside diffuser channel is affected by several factors, including viscosities, rotational speeds and liquid flowrates. However, this vortex and recirculation contribute little to ESP pressure increment.

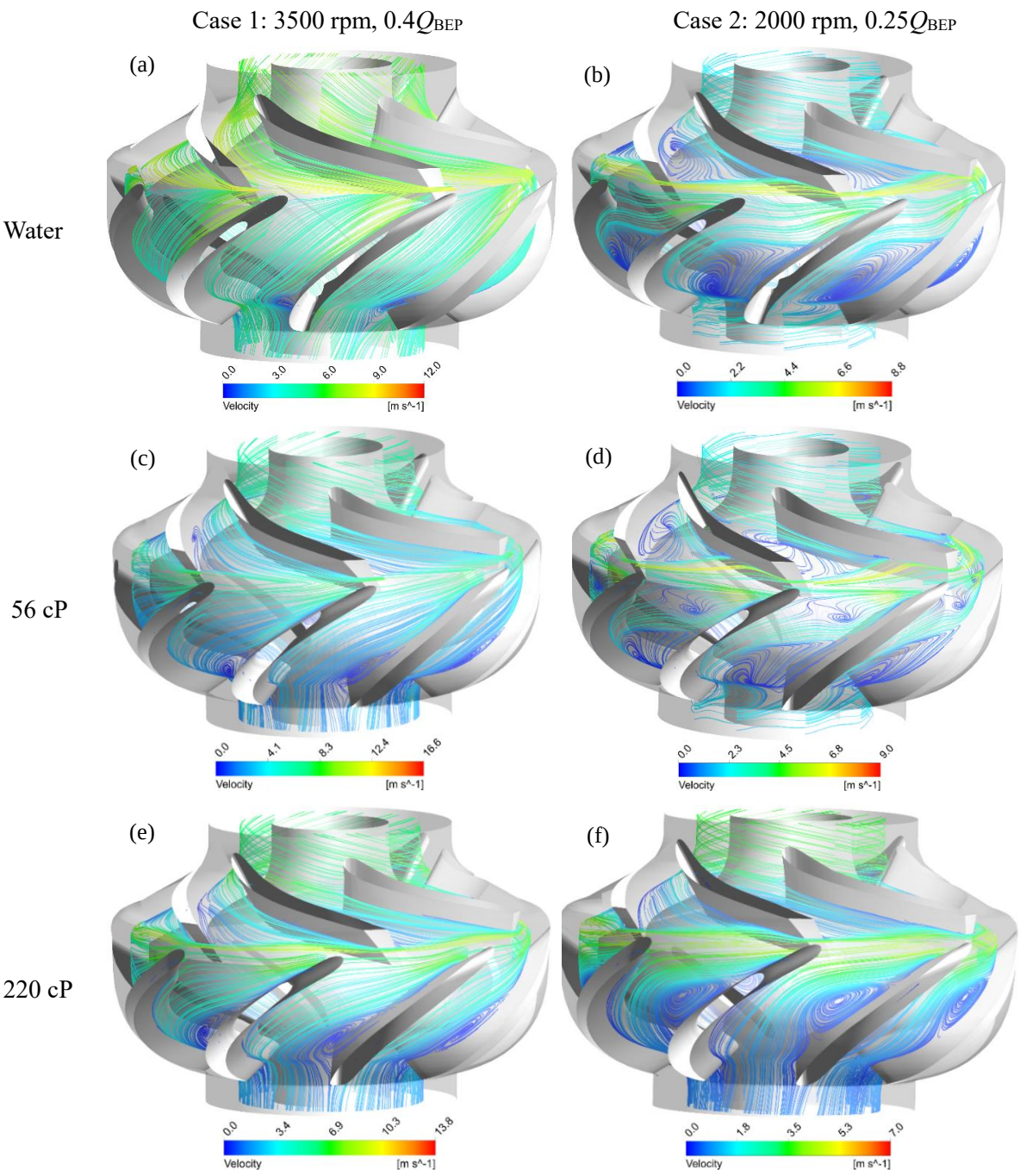

Figure 3.9 Streamline comparison under different flow conditions at half span of stage 3 in DN-1750 ESP

ESP boosts pressure by converting kinetic energy to pressure potential. The impeller-diffuser interaction guides fluid away from impeller, which causes additional energy dissipation and local hydraulic pressure loss, resulting in abrupt pressure reduction. Figure 3.10 shows the

averaged total pressure along streamwise location for the entire 7 stages at 2000 rpm and 0.4Q_{BEP}. The streamwise location is the dimensionless distance from the inlet to the outlet. It ranges from 0 to 1 for the first stage, 1 to 2 for the second one and so on. It can be seen in Figure 3.10 that ESP overall boosting pressure decreases with fluid viscosity increase. From inlet of stage 1 to the outlet of stage 7, the fluid pressure is boosted within the impeller of each stage. However, the pressure does not change much in diffusers. A pressure drop is observed at inter-stage due to the interaction of ESP rotating impeller and stationary diffuser. In order to improve pump hydraulic efficiency, the blade angles at impeller outlet and diffuser inlet need to be at around operation flowrate so that the pressure drop due to impeller-diffuser interaction can be minimized (Wu et al., 2015).

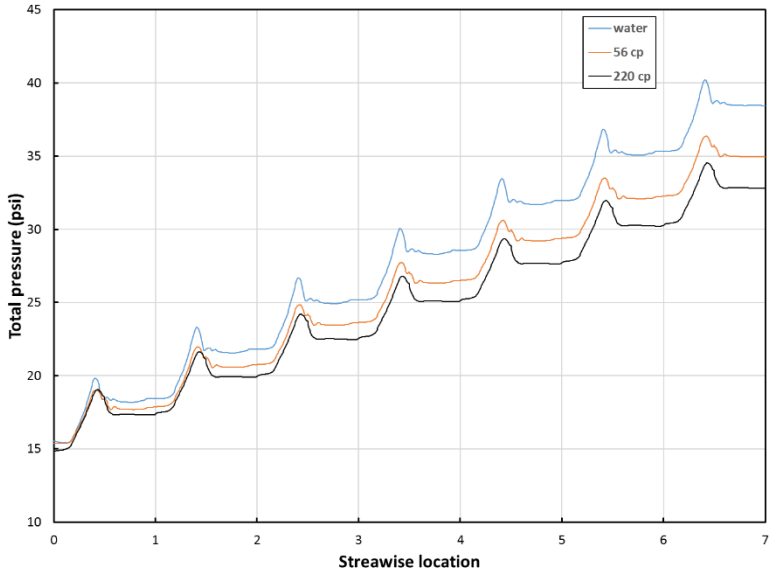

Figure 3.10 Total pressure averaged along streamwise location for 2500 rpm, $Q = 0.4Q_{BEP}$

3.2 CFD Simulation of Oil-Water Flow

3.2.1 DN-1750 ESP Mesh

For emulsion CFD simulation, full-stage is used in order to capture any physical phenomena that may exist between the two liquids. In this study, the ESP flow domain comprises of 3 stages which are assembled in series as shown in Figure 3.11a. The single-stage pressure increment is obtained by calculating the pressure difference between the inlet and outlet of stage 3.

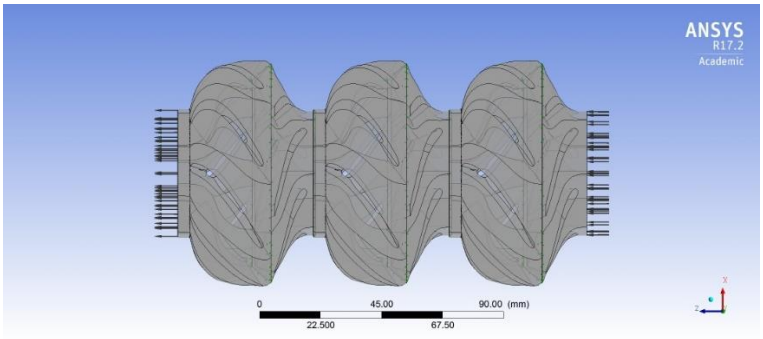

(a)

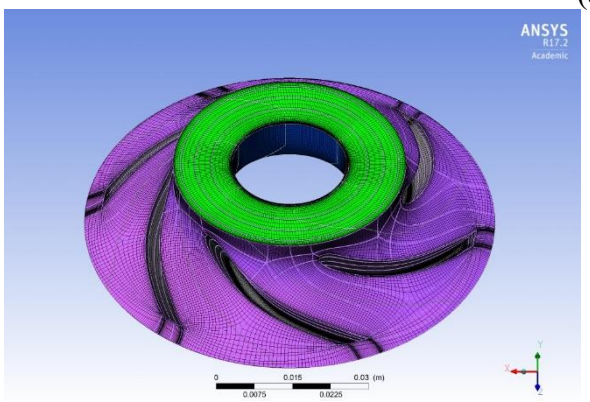

(b)

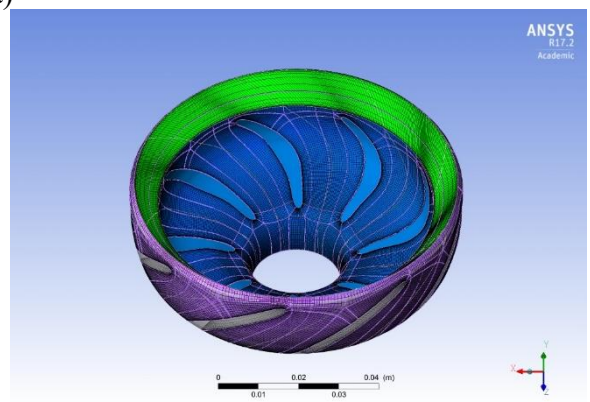

(c)

Figure 3.11 Grid generation on DN-1750 ESP, (a) multistage pump assembly, (b) grid for whole impeller and (c) grid for whole diffuser passage

Numerical studies regarding comparison and selection of grid has been conducted by researchers (Becker et al., 2010; Tomita et al., 2012). The structured grids made up of hexahedrons are generated with ANSYS Turbogrid 15. The structured hexahedral grids based on simplified multistage geometry are shown in Figure 3.11. As mentioned above, the complete fluid domain comprises of three domains of impeller Figure 3.11(b) and diffuser Figure 3.11(c). Each domain is meshed with structural hexahedrons with the refinement near blade surfaces. The frozen-rotor technique is used to calculate interactions between rotor and stator of each stage. All impeller domains are set to rotational reference frame while diffuser domains are set to stationary reference frame.

3.2.2 Eulerian-Eulerian Multiphase Model

This study employs Eulerian-Eulerian approach incorporated with standard k-ε turbulence model for solving the fully transient three-dimensional incompressible N-S equations as well as continuity equations for each phase. Interactions between phases can be modeled by interfacial momentum transfer terms. Assuming isothermal binary immiscible oil-water flow, the interfacial mass and energy transfer are not taken into account.

3.2.2.1 Eulerian-Eulerian Multiphase Model: For CFD simulation of multiphase flow, the Eulerian-Eulerian model may be more complex since it introduces additional phases together with n sets of conservation equations (Achouri et al., 2012), where n depends on phase number. It is recommended due to its general applicability for a wide range of volume fraction (Huang et al., 2014). Using this approach, the fields of velocity and volumetric fraction are calculated individually, while the pressure field is shared among phases (Zhu and Zhang, 2014). Assuming

no mass source or interfacial mass transfer, the continuity equation of oil-water two phase flow can be written as

$$\frac{\partial(\rho_i \alpha_i)}{\partial t} + \nabla \cdot (\rho_i \alpha_i \vec{u}_i) = 0 \quad (3.16)$$

where ρ_i, α_i, $\vec{u}_i$ are density, volumetric fraction, velocity vector of i^{th} phase, respectively. Subscript $i = o$ or w denotes oil or water. A simple constraint that volumetric fractions sum up to unity is expressed as

$$\sum_{i=1}^{n} \alpha_i = 1 \quad (3.17)$$

The momentum balance of phase i yields

$$\frac{\partial(\rho_i \alpha_i \vec{u}_i)}{\partial t} + \nabla \cdot (\rho_i \alpha_i \vec{u}_i \vec{u}_i) = -\alpha_i \nabla P + \alpha_i \nabla \cdot (\bar{\bar{\tau}}_i) + \alpha_i \rho_i \vec{g} + \vec{F}_i + \vec{F}_{lift,i} \quad (3.18)$$

where $\bar{\bar{\tau}}_i$ is the i^{th} phase stress-strain tensor given by Equation (3.19), $\vec{g}$ is the gravity acceleration vector. $\vec{F}_i$ and $\vec{F}_{lift,i}$, represent interfacial forces for the interfacial momentum transfer, including external body forces (e.g. buoyancy and centrifugal forces) and lift force, respectively.

$$\bar{\bar{\tau}}_i = \alpha_i \mu_i (\nabla \vec{u}_i + (\nabla \vec{u}_i)^T) + \alpha_i \left(\lambda_i - \frac{2}{3}\mu_i\right) \nabla \cdot \vec{u}_i \bar{\bar{I}} \quad (3.19)$$

Equations (3.16) to (3.19) above constitute the general form of Eulerian-Eulerian inhomogeneous multiphase model. In order to solve this model, the RANS equations are adopted, which statistically average turbulence fluctuations in above transport equations. The additional Reynolds stress term in RANS equations is modeled by the two-equation turbulence model.

3.2.2.2 Standard *k-ε* Turbulence Model: Due to the empirical nature of most turbulence models (Gulich, 2008; Zhou et al., 2012) which quantify Reynolds stress by correlations, a universally validated turbulence model yielding optimal results for all simulation seems to be unlikely (Zhu and Zhang, 2014). The standard *k-ε* two equation model offers a good compromise

between numerical effort and computational accuracy (ANSYS, 2015), which is widely used in industry (Maitelli et al., 2010; Qi et al., 2012). This model incorporates two transport equations for the turbulent kinetic energy (k) and energy dissipation rate (ε). Under multiphase flow condition, the standard k-ε model needs to be modified to consider turbulence within different phases. Therefore, the hypothesis of eddy viscosity is assumed to hold for each turbulent phase, which is given by

$$\mu_{eff,i} = \mu_i + \mu_{t,i} \tag{3.20}$$

where $\mu_{eff,i}$ is the effective viscosity, μ_i and $\mu_{t,i}$ are molecular viscosity and turbulent viscosity of i^{th} phase, respectively. For k-ε model, the turbulent viscosity is modeled as

$$\mu_{t,i} = \rho_i C_\mu \frac{k_i^2}{\varepsilon_i} \tag{3.21}$$

In Equation (3.21), turbulent kinetic energy (k) of i^{th} phase can be obtained by deriving exact transport equations (Xiang et al., 2011), while its dissipation rate (ε) is correlated by physical reasoning (Achouri et al., 2012). Similar to single-phase turbulent flow, the transport equations for k and ε in multiphase flow are

$$\frac{\partial(\rho_i \alpha_i k_i)}{\partial t} + \nabla \cdot (\rho_i \alpha_i \vec{u}_i k_i) = \nabla \cdot \left(\left(\mu_i + \frac{\mu_{t,i}}{\sigma_k} \right) \nabla k_i \right) + \alpha_i (P_i - \rho_i \varepsilon_i) + \vec{T}_{i,j}^{(k)} \tag{3.22}$$

and

$$\frac{\partial(\rho_i \alpha_i \varepsilon_i)}{\partial t} + \nabla \cdot (\rho_i \alpha_i \vec{u}_i \varepsilon_i) = \nabla \cdot \left(\left(\mu_i + \frac{\mu_{t,i}}{\sigma_\varepsilon} \right) \nabla \varepsilon_i \right) + \alpha_i \frac{\varepsilon_i}{k_i} \left(C_{\varepsilon,1} P_i - C_{\varepsilon,2} P_i \rho_i \varepsilon_i \right) + \vec{T}_{i,j}^{(\varepsilon)} \tag{3.23}$$

where $C_{\varepsilon,1}$ and $C_{\varepsilon,2}$ are constants, σ_k and σ_ε are turbulent Prandtl numbers for k and ε, respectively. P_i is the turbulence production term due to viscous forces in phase i. The additional terms $T_{i,j}^{(k)}$ and $T_{i,j}^{(\epsilon)}$ represent interphase transfer of k and ε, which usually are omitted but can be added by user.

3.2.3 Closure Relationships

For Eulerian-Eulerian multiphase model, the interactions between phases are effected via interfacial momentum transfer terms. Thus, additional models regarding interfacial forces are needed to make two-fluid multiphase model closed and solvable. As shown in Equation (3.18), the interfacial forces can be categorized into drag and lift forces, etc.

3.2.3.1 Drag Force: In liquid-liquid two-phase flow, the drag force represents interfacial momentum transfer due to velocity difference between the dispersed and the continuous liquid phases, which can be modeled by adding a source term in N-S equations:

$$F_{ow}^{drag} = \frac{3}{4} C_D \frac{\rho_o \alpha_w}{d_w} |\vec{u}_o - \vec{u}_w|(\vec{u}_o - \vec{u}_w) \quad (3.24)$$

where C_D is drag coefficient. In this study, due to high shear effect inside impeller, the dispersed phase is treated as monodispersed flow with all droplets of the same spherical shape and size. A drag force was suggested by Schiller and Naumann (1935):

$$C_{D_{sphere}} = max\left(\frac{24}{Re}(1 + 0.15Re^{0.687}), 0.44\right) \quad (3.25)$$

In Equation (3.25), the Reynolds number Re is defined by

$$Re = \frac{\rho_o |\vec{u}_o - \vec{u}_w| d_w}{\mu_o} \quad (3.26)$$

Droplet sizes in ESPs are consider small and can be assumed to be spherical. Therefore, Schiller Naumann drag model can be used although it is developed based on solid spherical particles.

3.2.3.2 Lift Force: In a multiphase shear flow, due to velocity gradients in the primary phase flow field, lift force exerts on dispersed particles, which is perpendicular to the direction of relative motion between phases. The force can be correlated to the relative velocity and the local liquid vorticity from Drew and Lahey (1979):

$$F_{ow}^{lift} = C_L \rho_o (\vec{u}_o - \vec{u}_w) \times (\nabla \times \vec{u}_o) \quad , \tag{3.27}$$

where C_L is lift coefficient. A lift force model proposed by Legendre and Magnaudet (1998) is adopted in this study, which is applicable mainly to the lift force of small diameter spherical fluid particles. The lift coefficient can then be estimated as

$$C_L = \sqrt{C_{L,low\ Re}^2 + C_{L,high\ Re}^2} \tag{3.28}$$

where

$$C_{L,low\ Re} = \frac{15.3}{\pi^2} Re_\omega^{-0.5} \left(1 + 0.2 \frac{Re_p^2}{Re_\omega}\right)^{-1.5} \tag{3.29}$$

$$C_{L,high\ Re} = \frac{1}{2} \frac{1+16Re_p^{-1}}{1+29Re_p^{-1}} \quad , \tag{3.30}$$

the particle Reynolds number Re_p and vorticity Reynolds number Re_ω are defined as

$$Re_p = \frac{\rho_o |\vec{u}_w - \vec{u}_o| d_w}{\mu_o} \quad , \tag{3.31}$$

and

$$Re_\omega = \frac{\rho_o |\nabla \times \vec{u}_o| d_w^2}{\mu_o} \quad . \tag{3.32}$$

As suggested by Legendre and Magnaudet (1998), the validity range of the above lift force model is $0.1 < Re_p < 500$ and $Re_\omega \leq 1$.

3.2.4 Boundary Conditions and Numerical Scheme

In this study, the complete computational domain comprises of three congruent stages, each of which contains a full impeller and a full diffuser. GGI interface type is used for each pair of rotor and stator interfaces to maintain strict conservation of fluxes across these interfaces. Thus, total five GGI pairs are generated, where three of them are within stages, and the other two pairs are at inter-stages.

From inlet to outlet, the boundary conditions are specified according to corresponding experimental configurations. As recommended by ANSYS CFX (2008), a mass flowrate is imposed with medium (5%) turbulence intensity at the inlet, while a static pressure of (0 psig) is imposed at the outlet.

For oil-water flow, water fraction is also specified at the inlet. For walls inside impellers, the rotating frame type is adopted. Correspondingly, all diffuser walls are set to stationary frame type. In addition, the no-slip condition at walls is used with volume fraction wall contact model. The near-wall treatment is based on the scalable wall functions.

All simulation cases under both single-phase and liquid-liquid two-phase flow conditions are conducted with the same numerical schemes. For spatial discretization of advection terms and turbulence equations, the high resolution scheme is used, which is a second order algorithm in CFX-solver. A fixed physical timescale of $\frac{1}{\Omega}$ is used with the maximum 100 outer loop iterations to achieve convergence. The convergence criterion is satisfied when RMS residual drops below 10^{-4} and convergence is achievable for all simulation cases.

3.2.5 Results and Discussions

3.2.5.1 Validations of Mesh Independence and Turbulence Model: Figure 3.12 shows the mesh validation with different grid numbers using a two full stages geometry by changing the boundary layer factor ratio. In this study, CFD simulation started with water flow in two ESP full stages at 3500 rpm. Results are compared in order to achieve the optimum grid number for the simulation. A comparison between the first and the second stage against the experiments are also shown in Figure 3.12. The first stage performance deviates more at high and at low flowrates for all cases. The second stage results are closer to the experimental results. This may be due to the entrance effect since the inlet condition of the first stage is perpendicular to the domain which may not represent the physical experiment. This effect is minimized for second stage and flow is closer to the reality. The 1.2 M mesh showed higher deviations at the extreme flowrates, indicating that the grids are too coarse for the solver to achieve accurate solution. The difference between 2.7 M and 5.2 M meshes are insignificant, so 2.7 M is acceptable for the two-phase simulations. Therefore, the final grids generated in simplified impeller and diffuser contain 555,636 and 806,752 elements, respectively.

Simulations are also run with 3 full ESP stages, to determine if there is any improvement over the two-stage simulation as shown in Figure 3.13. CFD results show that the second stage performance is less than 5% lower in the two-stage simulation compared to three-stage simulations. This indicates that computational results are less sensitive to the outlet effect as opposed to the inlet effect. Therefore, a four-stage simulation will not have significant effect on the computed performance of the third stage although it will be more time consuming. Total grids for the complete three-stage computational domain contain 4,087,164 elements, which are

sufficient to guarantee grid independence.

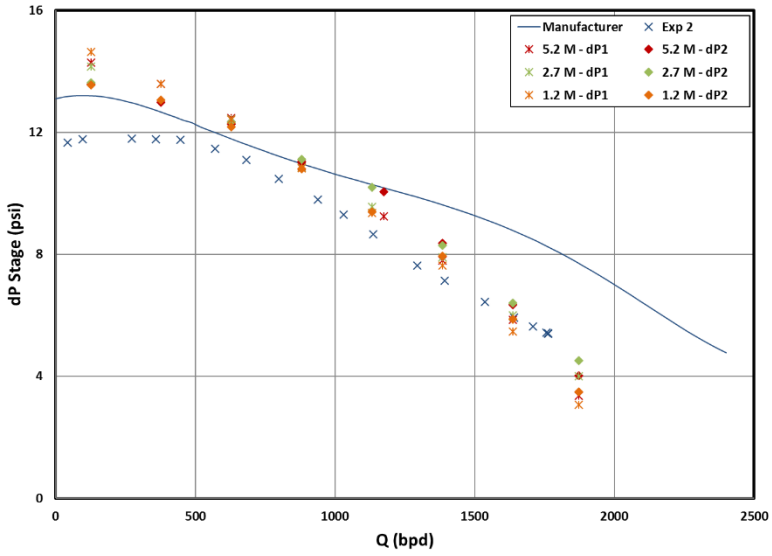

Figure 3.12 Mesh validation and number of grids check

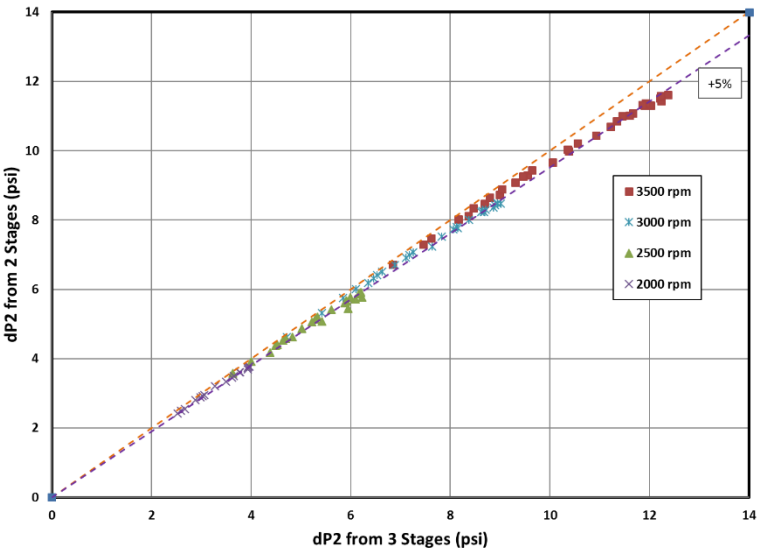

Figure 3.13 Comparison of second stage performance between 2 and 3 stages

The selection of turbulence model is a delicate task for CFD simulation as discussed by (Bradshaw, 1996; Asuaje et al., 2005), which is also a compromise of numerical effort and accuracy. There is no prominent variance among different turbulence model predictions. Due to relative less computational effort while providing high numerical accuracy, the *k*-ε two-equation

turbulence model is used in this study.

3.2.5.2 Single-Phase Simulation Results: As shown in Figure 3.14, it is noted that water simulation results for head are slightly higher than the experimental values at relatively low flowrates, indicating that CFD simulations over predict ESP single-phase performance. As qualitatively analyzed by Zhou et al. (2012), the overestimation could be ascribed to the neglect of leakage flow through the radial clearance between impeller and diffuser. The numerical results are consistent with the changing trends of experimental data. The head seems to agree with experimental data better at relatively higher flowrates.

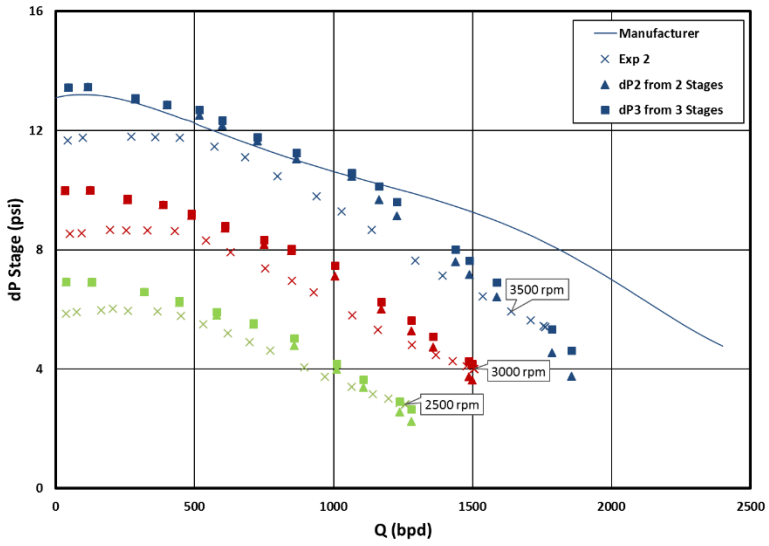

Figure 3.14 Influence of number of stages on simulation results for water

From Figure 3.15, the differences in the simulation results compared to experiments are much higher compared to water differences. This is probably due to stage ware out or probably due to roughness increase. Quantitatively, the simulation results are about 40% higher than the experimental results as shown in Figure 3.16 with less deviations for lower viscosities. Unfortunately it is not clear when the simulation curves intersect the experiment curves, but that

is most likely happening at higher flowrates, i.e. higher than 1600 bpd and 1500 bpd for 3500 and 3000 rpm, respectively. Compared to the differences shown in Figure 3.8 which is for the overall performance, the differences for the single stage is much higher. This may be due to the stage being rusty or worn out. In other words, the third stage may perform worse than some of the other stages. This is clearly observed for most of the 3500 and 3000 rpm experiments as shown in Figure 3.17 especially at lower flowrates. However, this does not agree completely with the observation found in Figure 2.13, which shows that the stage performs better than the average at low flowrate and worse than the average at high flowrate.

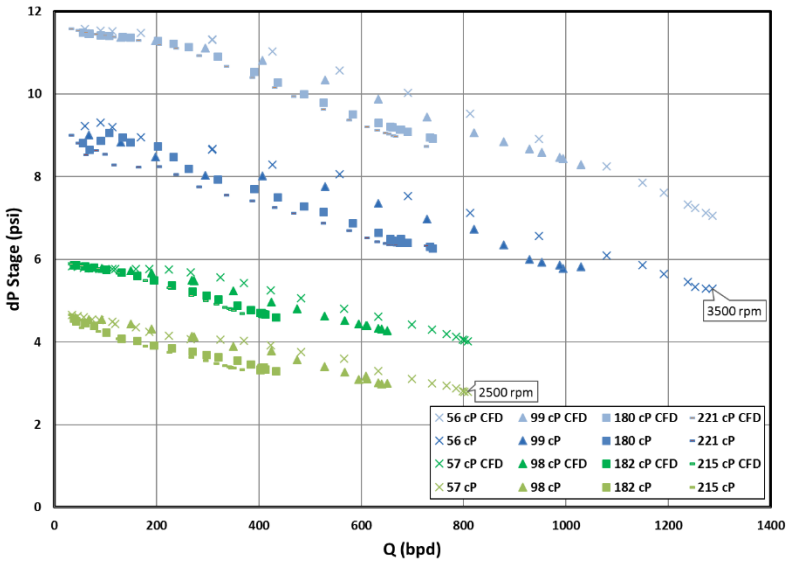

Figure 3.15 Comparison of CFD simulated stage performance

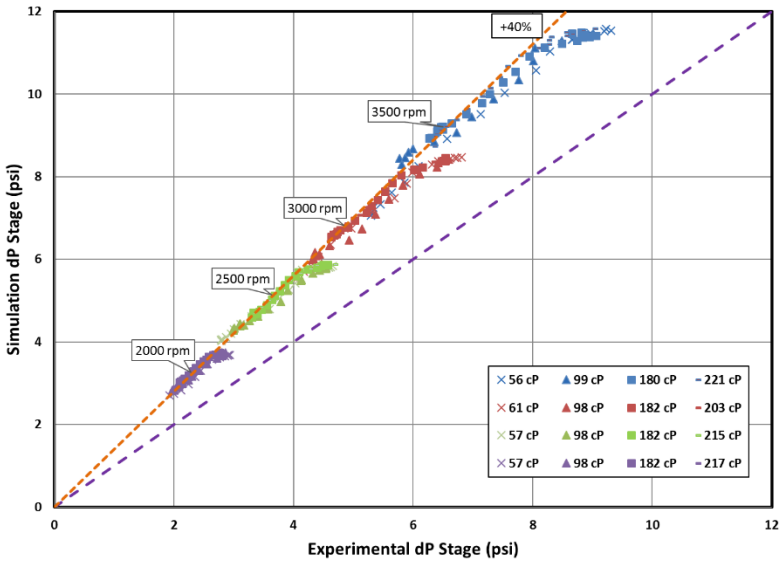

Figure 3.16 Stage dP simulation results deviation from experimental for oil

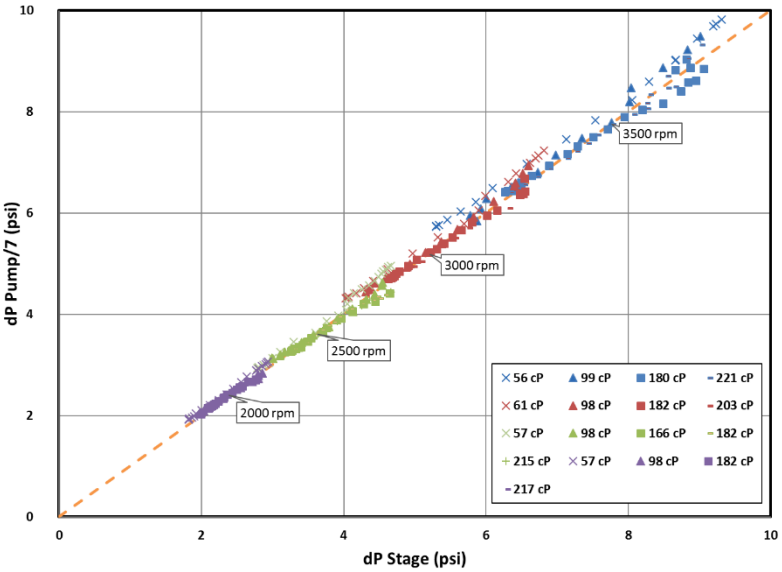

Figure 3.17 Comparison between stage and average ESP performance

3.2.5.3 Two-Phase Simulation Results: A preliminary two-phase simulation run was conducted in order to simulate two phase behavior in the stage. Several assumptions were considered, such as that the dispersed phase is monodispersed. As velocity decreases when emulsion passes through the diffuser, coalescence takes place but we assume this phenomenon negligible, so no coalescence model was considered. Since there is a density difference between

the two phases, drag force exists and we used particle drag model of Schiller and Naumann (1933). Flow direction in the stage is complicated and lift force is defined as force acting in direction perpendicular to flow. Therefore, we used lift force model of Legendre and Magnaudet. Since oil is the continuous phase in most experiments, turbulence model of k-ω was used. Droplet mean diameter for the base case was obtained from the FBRM feasibility test and was defined in the CFD simulation. Interfacial tension between oil and water was estimated using Peters (2013) correlation in Equation (3.33). In his experiments, air-oil interfacial tension was 21 mN/m while it is 27 mN/m for ND20 according to Brito (2014).

$$\sigma = 0.122T + 32.82 \tag{3.33}$$

where σ is the interfacial tension (mN/m) and T is temperature (°C).

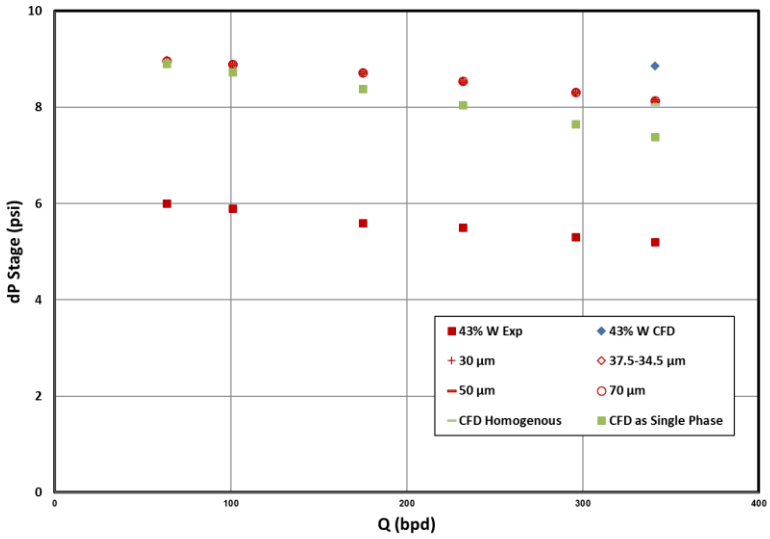

Figure 3.18 Old ND20 emulsion simulation result at 3000 rpm

Usually, a steady state two-phase simulation does not converge and switching to transient simulation will solve the problem. In our case, the solver was able to achieve a solution after a considerable number of iterations. From Figure 3.18, the preliminary result of a 2-phase simulation run shows that the stage boosting pressure is slightly higher than the single-phase oil CFD

simulation and significantly higher than the 2-phase experiment. Changing the dispersed droplet size did not affect the result and the data overlap with insignificant difference which is difficult to identify from the figure. We also assumed the two phases to be homogenous, at which both fluids share a common flow field as well as the turbulence field but that did not affect the result either. So, we believe the main reason is that CFX treats the 2-phase as a dispersion, not emulsion. This means the water droplets are dispersed in the continuous oil without affecting the mixture rheology, which does not represent the reality. Therefore, the last option is to assume both phases as a single phase with a modified effective viscosity. Thus, the average density is estimated based on the no slip mixture density while the viscosity is defined from the PV. Thermal properties for the single phase liquid are defined arbitrary since the system is assumed to be isothermal.

Results shown in Figure 3.19 are for the old and new batch of ND20 emulsions. In (a), the 60% experiment is dropped out since the water fraction is not stable and simulation cases are revisited to redefine the correct effective viscosity, based on the viscosity validation experiments. Similarly, water fractions higher than 20% are dropped out for (b) and (c). For all figures, any data point that does not maintain the same water fraction is dropped out. All simulation results are much higher than the experimental results and most of them are around +40% as shown in Figure 3.20. A small trend is observed at higher rotational speeds and low flowrates, the deviation becomes less which is around 30%.

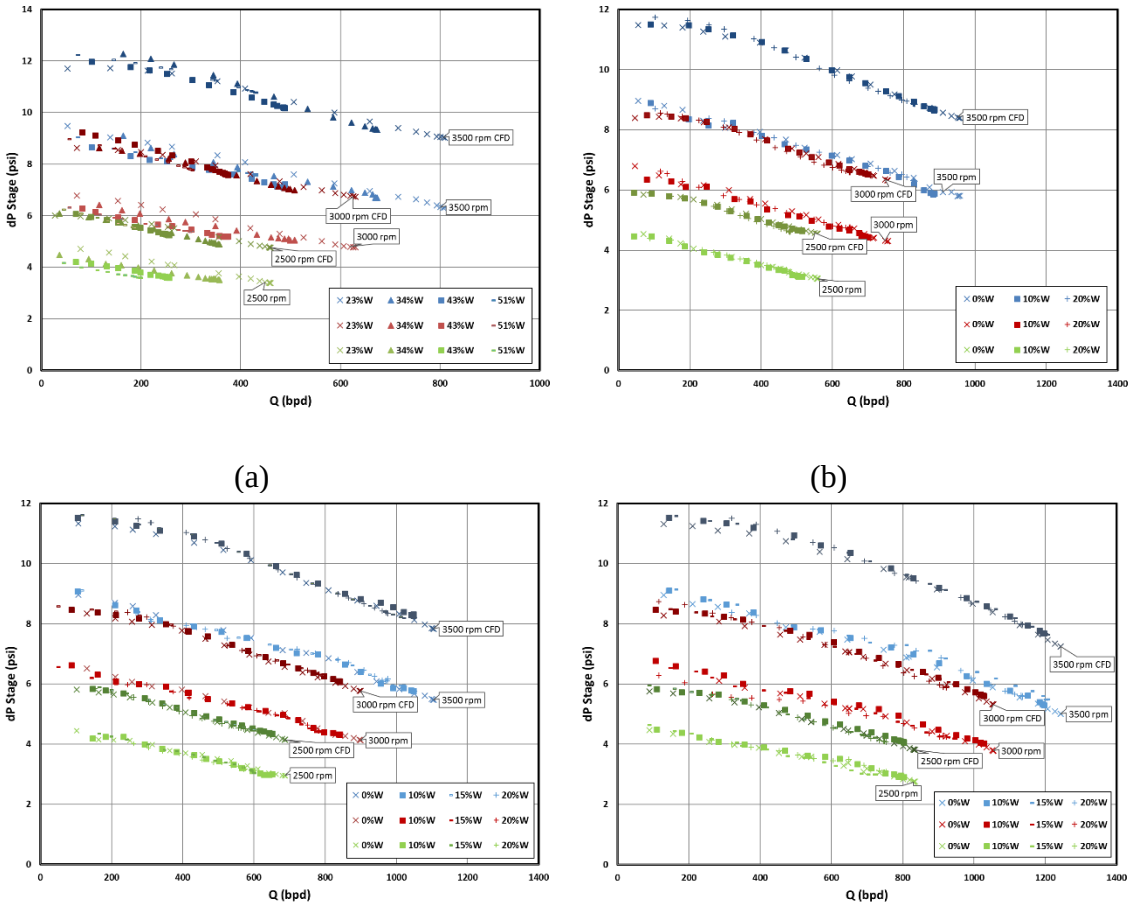

Figure 3.19 Emulsion simulation results, (a) Old ND20, (b) New ND20 at 80 °F, (c) New ND20 at 88 °F, (d) New ND20 at 100 °F

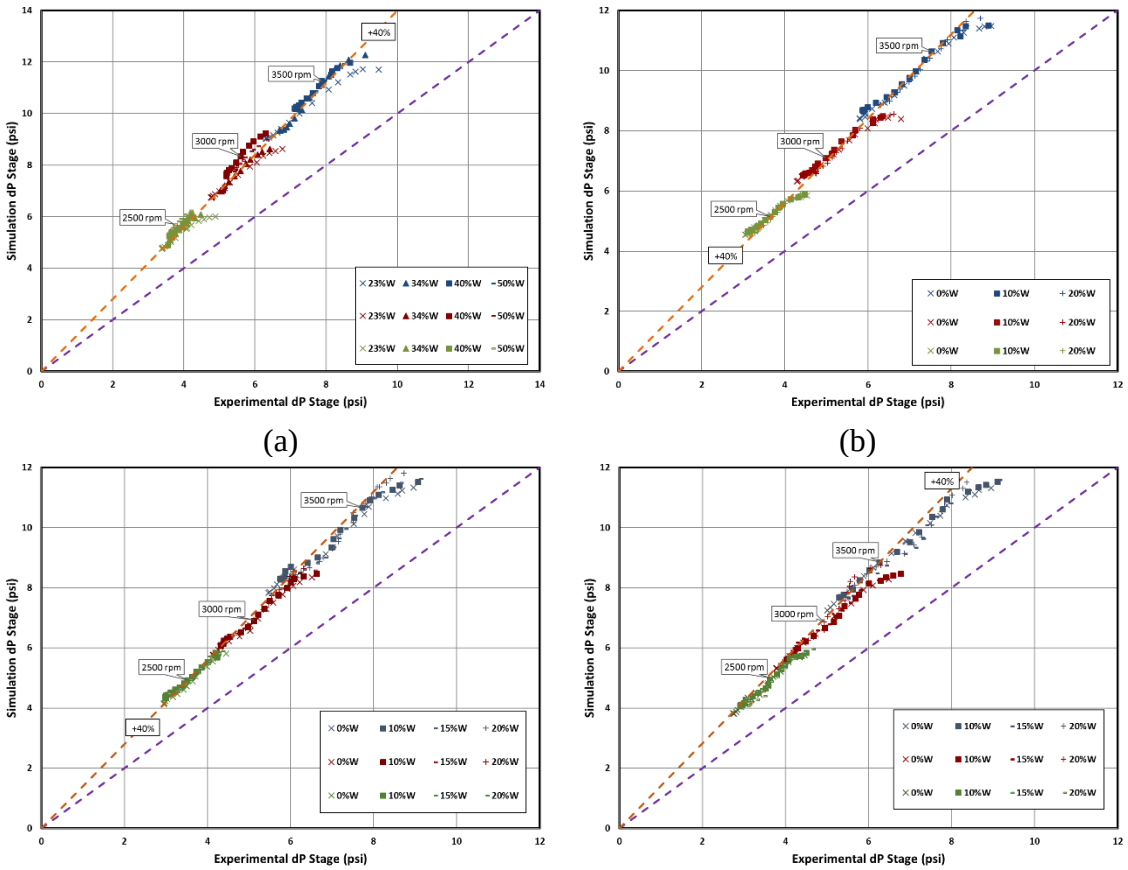

(a) (b)

(c) (d)

Figure 3.20 Simulation results deviation from experimental for emulsion with, (a) Old ND20, (b) New ND20 at 80 °F, (c) New ND20 at 88 °F, (d) New ND20 at 100 °F

On the other hand, emulsion simulation results for Isopar V show large deviations at high and low flowrates for 3500 and 3000 rpm which can be as high as +50% as shown in Figure 3.21 and Figure 3.22. For medium flowrates, the match is close for all rotational speeds which is around +25%. Low flowrates (below 400) at 2500 rpm were very unstable so comparison of simulation results to those data is invalid.

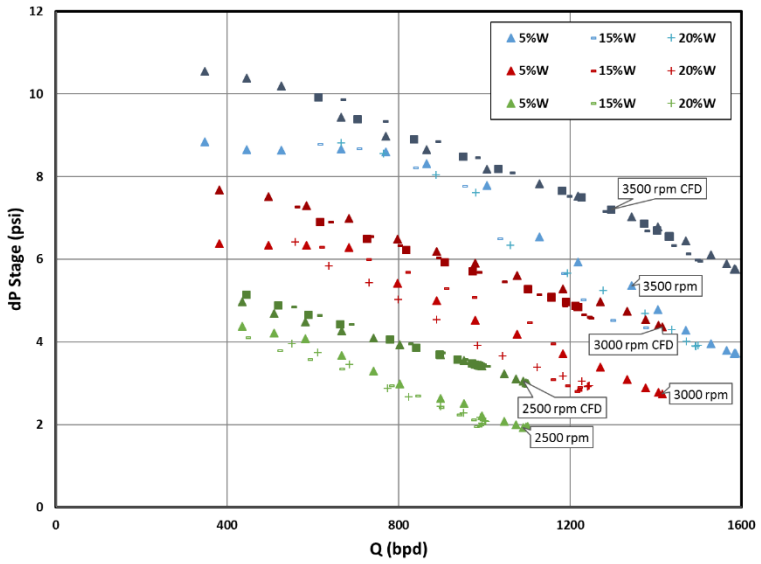

Figure 3.21 Isopar V emulsion simulation results

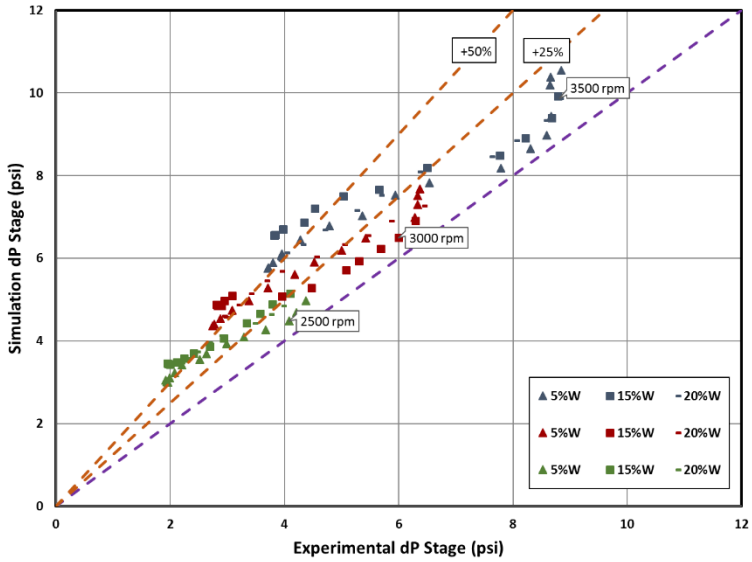

Figure 3.22 Simulation results deviation from experimental for emulsion with Isopar V

3.3 Numerical Simulation Summary

In this chapter, the numerical simulations on ESP performance under single-phase water or oil flow and oil-water two-phase flow conditions are conducted. Verified by experimental data, the CFD simulation is a powerful and reliable tool to study the complex flow structures and characteristics inside a rotating ESP.

In single-phase simulations, the simulated ESP pressure increment under water flow matches the experimental results, which validates the numerical methodology using a single channel for 7 stages. However, the match was acceptable only for water using the second approach which is conducted by simulating 3 full stages. For single phase oil the deviation was high which may be caused by the actual pressure loss through the leakage and possibly caused by the stage being rusty or worn out. Using SST turbulence model, the stage pressure increment under viscous fluid flow is over predicted by CFD simulation about 15%. The linear trend of *H*-*Q* curves at high liquid viscosity is captured by numerical simulations. From the numerically simulated flow structures as shown by the streamlines, the recirculation flow is observed at the trailing edges of impeller blades at high fluid viscosity or low liquid flowrate.

For two-phase simulation, a 3D CFD code is implemented to a three-stage ESP model to simulate the pump stage pressure increment with emulsion. Using the structured hexahedral grids and frozen-rotor techniques, the mesh independence and numerical accuracy are confirmed. For oil-water two-phase simulation, the Eulerian-Eulerian two-fluid model is used. The interfacial momentum transfer forces like drag and lift forces are incorporated. Unfortunately, the code was not able to identify the mixture as emulsion, and that was clear when the stage performed much

better with water-in-oil emulsion compared to the single phase oil. Therefore, the two phases were assumed as a single phase and results showed deviation of 40% higher than experimental results.

CHAPTER 4

EMULSION RHEOLOGY AND ESP PERFORMANCE MODELS

Developing a mechanistic model for ESP performance prediction under water/oil flow is one of the main objectives of this study and is discussed in this chapter. However, since emulsion is also the main focus in this study, its rheology needs to be estimated first at the stage conditions. Models are later validated with the available experimental data.

4.1 Emulsion Rheology Model

Emulsion rheology is affected by many factors, including but not limited to density, viscosity, volumetric fraction of each phase, the interfacial tension between the phases, droplet characteristics of the dispersed phase, shear rate, temperature, and amount of solids present as suggested by Kokal (2005). Our initial thought is to model the emulsion rheology by the means of the FBRM to obtain the average droplet size. Unfortunately, either the instrument or the flow loop setup was not suitable to use the FBRM and the preliminary results were inconsistence when rotational speed changed. Another issue is that visualization of the flow behavior at the stage condition is not valid due to the high rotational speeds which requires an extremely high speed camera. Viscous fluids are also another obstacle in case for the visualization approach. Appendix D is dedicated to the detailed dimensional analysis for the model approach.

The first step in the proposed model is to define the inversion point in order to determine the water fraction at which the dispersed phase becomes continuous, which then applies to the

effective viscosity model. To estimate the inversion point, we assume Brinkman (1952) model listed in Table 2.3 to be applicable before and after the inversion point with modified exponent (*E*):

$$\mu_E = \frac{\mu_C}{(1-\phi_D)^E} \quad , \tag{4.1}$$

where μ_C is continuous phase viscosity, ϕ_D is volume fraction of dispersed phase, and the exponent *E* is found from experiments. At the inversion point,

$$\mu_E = \frac{\mu_O}{(1-\phi_W)^E} \tag{4.2}$$

and $$\mu_E = \frac{\mu_W}{(1-\phi_O)^E} = \frac{\mu_W}{\phi_W^E} \quad . \tag{4.3}$$

Equating Equation (4.2) to (4.3) yields

$$\frac{\mu_O}{(1-\phi_W)^E} = \frac{\mu_W}{\phi_W^E} \Rightarrow \frac{\mu_O}{\mu_W} = \left(\frac{1-\phi_W}{\phi_W}\right)^E. \tag{4.4}$$

By letting $\tilde{\mu} = \frac{\mu_O}{\mu_W}$ and solving for ϕ_W, the inversion point with respect to water fraction becomes

$$\phi_W = \frac{1}{1+\tilde{\mu}^{1/E}} \quad . \tag{4.5}$$

Then, the emulsion effective viscosity models shown in Equations 4.1 and 4.2 are used for the continuous-oil range and for the continuous-water range, respectively. The average droplet size of the dispersed phase is strongly affecting the rheology of the emulsion. As shown earlier, FBRM results are inconsistent and may not represent the stage condition. Here, we propose to use the Weber number since it reflects the average droplet diameter:

$$We = \frac{\rho_A v^2 l}{\sigma} \cong \frac{\rho_A Q^2}{\sigma V} \quad , \tag{4.6}$$

where μ_C is the average density, *Q* is the volumetric flowrate, *V* is the pump channel volume in one stage, and σ is the interfacial tension obtained experimentally. Turbulence exists at the stage

condition which can affect the droplet size and consequently, emulsion viscosity. Turbulence can be taken care of by approximating a representative Reynolds number:

$$Re = \frac{\rho_A v l}{\mu_A} \cong \frac{\rho_A Q}{\mu_A d} \tag{4.7}$$

where μ_A is the modeled emulsion viscosity, d is pump diameter. This means the Reynold number can be found by several iterations of the modeled emulsion viscosity. This approach is physically reasonable rather than using the continuous phase viscosity, which can also cause a discontinuity at the inversion point, since the viscosity changes from oil viscosity to water viscosity.

Shearing due to impeller rotation is another important factor that needs to be considered. Increasing the rotational speed will increase the shear rate and lower the effective viscosity of emulsion. On the other hand, increasing rotational speed causes finer dispersed droplets to form after the blade tips, causing the emulsion effective viscosity to increase. In this study, only the first effect is considered since it seems to have more influence on emulsion rheology compared to the effect at the blade tips. The dimensionless Strouhal number can take the rotational speed into account:

$$St = \frac{fl}{v} \cong \frac{fV}{Q} \tag{4.8}$$

where f is ESP rotation speed. Now we propose the following relationship to estimate the final emulsion viscosity by including all previous factors:

$$\mu_A = C(\mu_E - \mu_M) + \mu_M \tag{4.9}$$

where μ_E is the effective viscosity obtained from either Equation 4.2 or 4.3. μ_M is the mixture base viscosity which is defined as:

$$\mu_M = \frac{\mu_W}{(1-\phi_O\phi_{OE})^E} \tag{4.10}$$

where ϕ_{OE} is defined as:

$$\phi_{OE} = 1 - \left(\frac{\mu_W}{\mu_O}\right)^{1/E} \quad (4.11)$$

Finally, *C* is the factor combining the other parameters affecting the emulsion rheology. The objective is to find the relationship between the dimensionless numbers *We*, *Re*, and *St* with *C*. Therefore, we need to examine the following equation, obtain C within the targeted range, and obtain the exponents by validating results with experimental data:

$$C = \frac{(NWeRe)^n}{bSt^m} \quad (4.12)$$

Since the old ND20 emulsion experimental data seems to be less reliable in terms of the inversion point expectation, those data will not be used in the emulsion rheology model evaluation. After examining the parameters using the new ND20 emulsion experiment data, the exponent *E* in Equations (4.1) to (4.5) equals to 3.2 for ND20 oil emulsion and *C* equation can be written as:

$$C = \frac{(3WeRe)^{0.1}}{10St^{0.2}} \quad (4.13)$$

4.1.1 Model Validation

Figure 4.1 shows the approach of modeling the emulsion rheology at the stage condition. From the figure, we can see μ_E which is the modified Brinkman (1952) model has the highest trend, while the mixture base viscosity μ_M has the lowest trend, indicating the modeled effective viscosity cannot drop below the base viscosity. By applying *C* factor on the proposed Equation (4.9), the model is able to obtain the effective viscosity in the expected range.

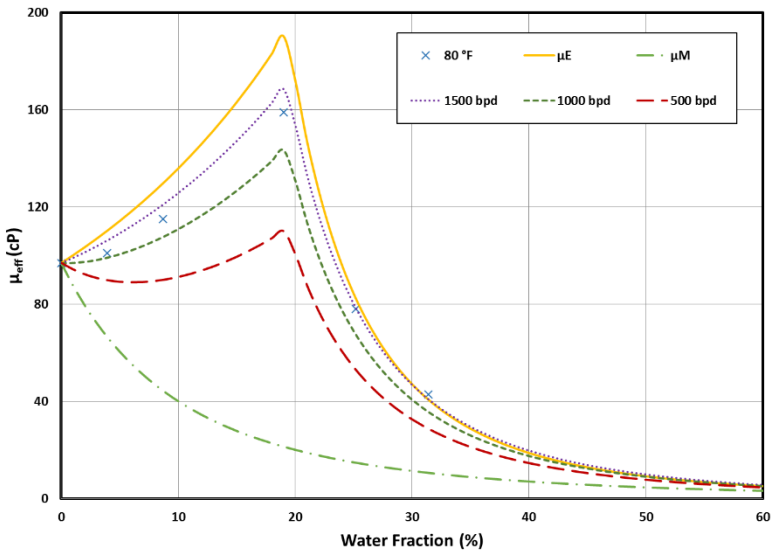

Figure 4.1 Emulsion rheology modeling principle

Figure 4.2 shows the expected behavior of the emulsion rheology model at different flowrates and different viscosities of ND20 oil at 3500 rpm of rotation. This cannot be validated with our current experimental data which shows that the emulsion effective viscosity is independent of flowrate, but that may be true only at the PV condition. In other words, the effective viscosity at the stage condition may change with flowrate. Validating emulsion effective viscosity with a known oil viscosity by matching the stage boosting pressure may not capture the difference since it is within the noise range. Similarly, Figure 4.3 shows the expected change of emulsion effective viscosity when the stage rotational speed changes for 1500 bpd flowrate. Although it is observed that the rotational speed does not affect the emulsion rheology based on the experimental PV results, it might have an effect at the stage condition which cannot be observed in our emulsion data neither with the new ND20 nor with Isopar V. However, Figure 2.38 shows that the rotational effect is observable at effective viscosities higher than 200 cP, and it increases as rotational speed decreases which validate the proposed relationship between the rotational speed and the effective viscosity.

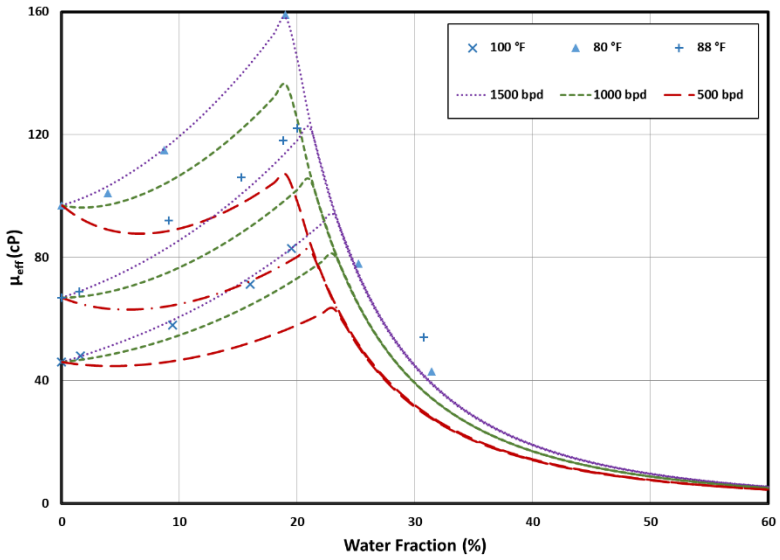

Figure 4.2 Expected emulsion rheology model behavior with ND20 oil at different flowrates and viscosities

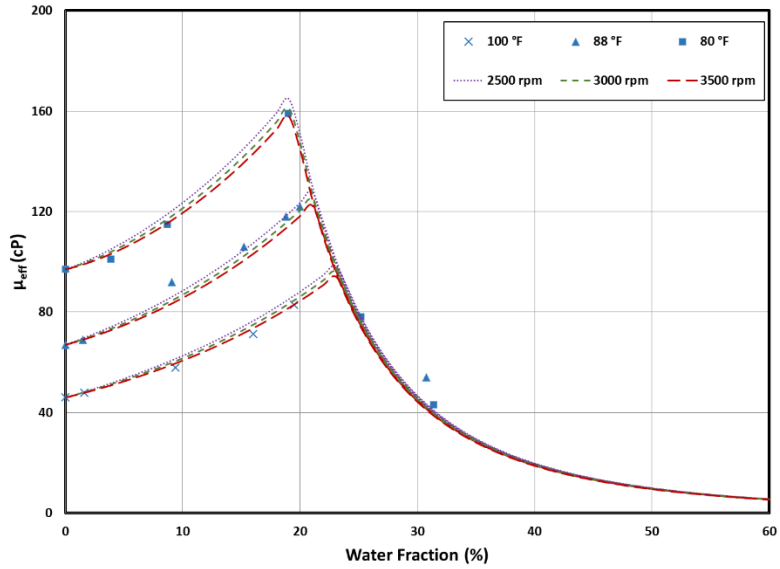

Figure 4.3 Expected emulsion rheology model behavior with ND20 oil at different rotational speeds

Figure 4.4 shows the effect of oil viscosity change on the inversion point. Although it is almost impossible to obtain the inversion point precisely from our experiment, it generally shifts to a higher water fraction as oil viscosity increases. The figure also shows that the maximum emulsion relative viscosity which corresponds to the inversion point, becomes higher as the oil

viscosity decreases. This is expected due to turbulence increase with viscosity decrease and hence, higher relative viscosity is expected.

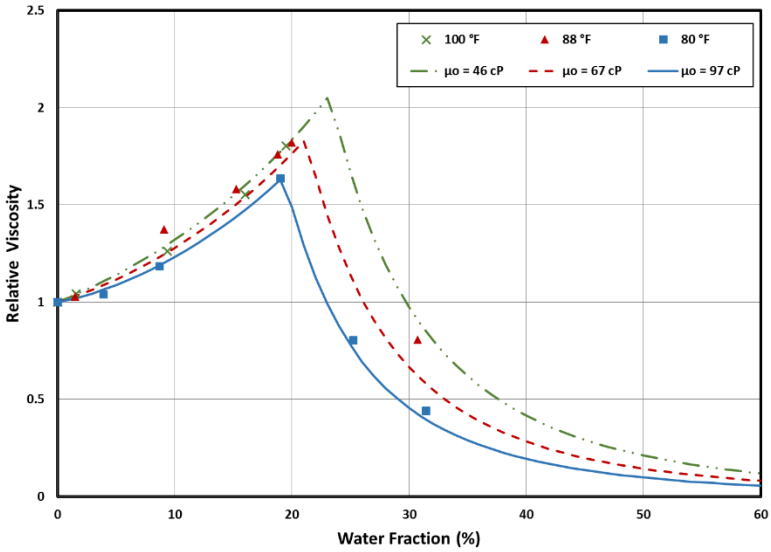

Figure 4.4 Emulsion rheology model validation with ND20 oil experimental data for different oil viscosities

For Isopar V emulsion shown in Figure 4.5, the model has reasonable prediction until the experimentally obtained inversion point. Afterwards, the model over-predicts the inversion point and over-predicts the effective viscosity in the oil-in-water region. Overall, most of the predicted effective viscosity values are within 5% deviation from the experimental data, except for low oil viscosities which shows higher deviation as shown in Figure 4.6.

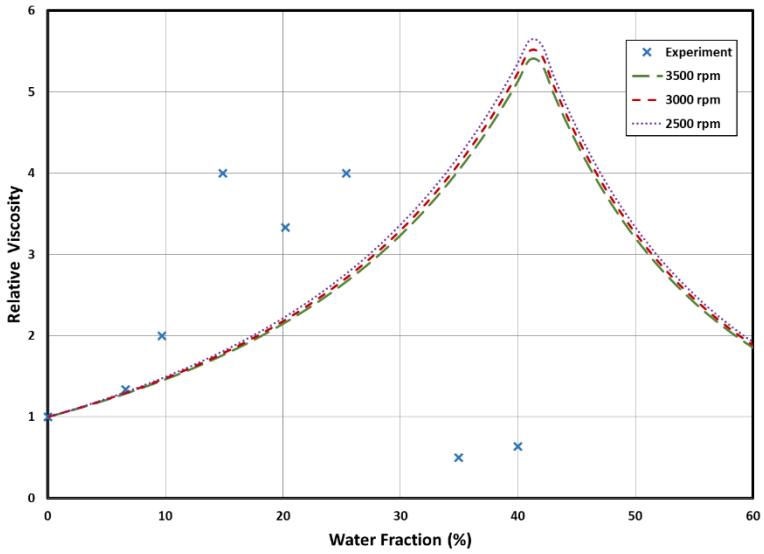

Figure 4.5 Emulsion rheology model validation with Isopar V oil experimental data at different flowrates

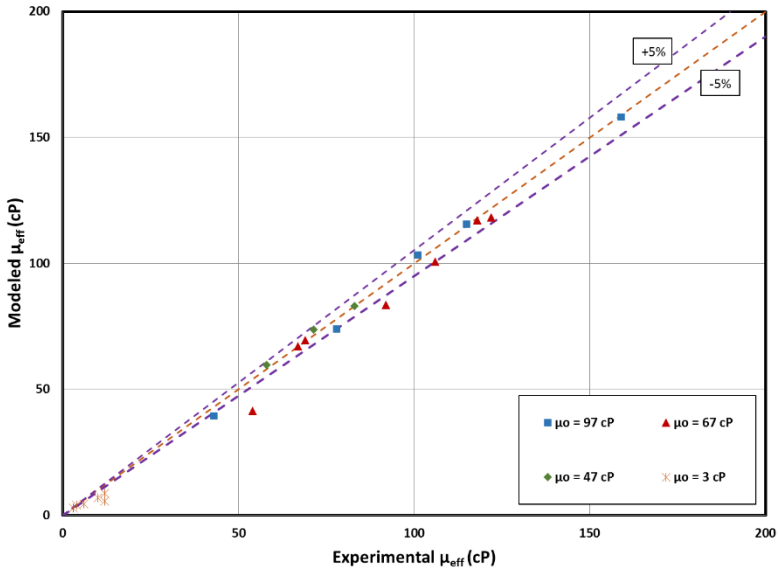

Figure 4.6 Emulsion rheology overall deviation from experimental data

4.2 ESP Performance Model

This model accounts for all losses, including friction, shock, recirculation, and leakage losses as discussed in the first section. The second section discusses the emulsion rheology under the stage condition. The mechanistic model starts from Euler's equation for centrifugal pump, which was derived from the conservation of the angular momentum. The Euler's equation is applicable to a two-dimensional (radial and tangential direction) system with the passages completely filled with fluid in the impeller. The streamlines are assumed to be similar to the blade's shape, with axisymmetric velocity profile. The equation is also limited to single-phase, incompressible, ideal fluids. Velocity triangles at the impeller inlet and outlet are shown in Figure 4.7.

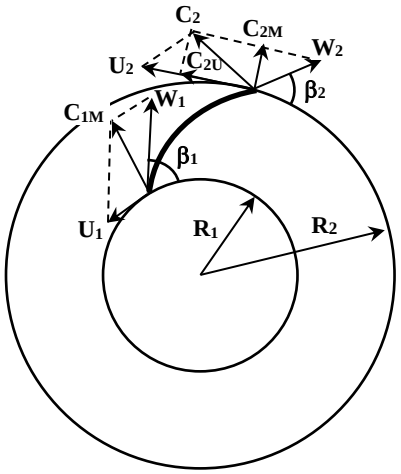

Figure 4.7 Velocity triangles at impeller inlet and outlet

In turbomachinery, in order for fluid to flow between blades there should be an external torque acting on it, which can be derived from Newton's second law of motion:

$$\tau = \dot{m}(R_2 C_{2U} - R_1 C_{1U}) \tag{4.13}$$

where R_1 and R_2 are the radii of the impeller inlet and outlet, respectively. Similarly, C_{2U} and C_{1U} are the fluid tangential velocity at the outlet and inlet, respectively. This is also called Euler's turbomachine equation. The tangential velocity of the impeller at inlet and outlet are respectively:

$$U_1 = R_1\Omega \text{ and } U_2 = R_2\Omega \tag{4.14}$$

where Ω is the angular velocity of the impeller which can be derived from the impeller rotational speed N in rpm:

$$\Omega = \frac{2\pi N}{60} \tag{4.15}$$

The shaft power required to maintain the fluid flow to flow can be obtained by multiplying the torque by the angular velocity as follows:

$$P_2 = \tau\Omega \tag{4.16}$$

$$\Rightarrow P_2 = \dot{m}(R_2C_{2U} - R_1C_{1U})\Omega = \rho Q(U_2C_{2U} - U_1C_{1U}) \tag{4.17}$$

According to the energy equation, the hydraulic power P_{hyd} added to the fluid can be written as the increase in pressure across the impeller multiplied by the volumetric flowrate:

$$P_{hyd} = \Delta P_{tot} Q \tag{4.18}$$

which can be rewritten as:

$$P_{hyd} = H_E \rho g Q \tag{4.19}$$

If the flow is assumed to be loss free, then the hydraulic and mechanical power can be equated:

$$P_{hyd} = P_2 \tag{4.20}$$

$$\Rightarrow H_E g = U_2C_{2U} - U_1C_{1U} \tag{4.21}$$

Finally, Euler's equation for a centrifugal pump impeller head is obtained:

$$H_E = \frac{U_2C_{2U} - U_1C_{1U}}{g} \tag{4.22}$$

which is also called the theoretical head since losses are not considered. From the velocity triangles, Euler's equation can also be re-written as follows:

$$H_E = \frac{U_2^2 - U_1^2}{2g} + \frac{W_2^2 - W_1^2}{2g} + \frac{C_2^2 - C_1^2}{2g} \quad (4.23)$$

where W_1 and W_2 are the fluid relative inlet and outlet velocities along the impeller surface, respectively. C_1 and C_2 are the inlet and outlet absolute fluid velocities, respectively. The first term is the static head as consequence of the centrifugal force, while the second term is the static head as consequence of the velocity change through the impeller, and the third term is the dynamic head.

The meridional velocity is the fluid absolute velocity in impeller channels. It is the combination of radial velocity and axial velocity. If the pump is a 100% radial type, the meridional velocity is fluid radial velocity. The meridional velocity at the impeller inlet and outlet are

$$C_{1M} = \frac{Q + Q_{LK}}{(2\pi R_1 - Z_1 T_B) y_{I1}} \text{ and } C_{2M} = \frac{Q + Q_{LK}}{(2\pi R_2 - Z_1 T_B) y_{I2}} \quad (4.24)$$

respectively, where Q is the flowrate, Q_{LK} is the leakage flowrate, Z_1 is the impeller blade number, T_B is the blade thickness projected to the radial direction, and y_{I1} and y_{I2} are the impeller inlet and outlet heights, respectively. From the velocity triangles, the relative velocity with respect to the impeller at the inlet and outlet are

$$W_1 = \frac{C_{1M}}{\sin \beta_1} \text{ and } W_2 = \frac{C_{2M}}{\sin \beta_2} \quad (4.25)$$

respectively, where β_1 and β_2 are the blade angle from tangential at impeller inlet and outlet, respectively. The absolute fluid velocity at the impeller inlet and outlet respectively are

$$C_1 = \sqrt{C_{1M}^2 + \left(U_1 - \frac{C_{1M}}{\tan \beta_1}\right)^2} \text{ and } C_2 = \sqrt{C_{2M}^2 + \left(U_2 - \frac{C_{2M}}{\tan \beta_2}\right)^2} \quad (4.26)$$

Tangential fluid velocity at impeller inlet, depending on pump design, is normally small. If we assume no tangential fluid velocity at impeller inlet, C_{1U} =0 and $C_1 = C_{1M}$, as shown in Figure 4.8. Euler's equation becomes

$$H_E = \frac{U_2^2}{g} - \frac{U_2 C_{2M}}{\tan \beta_2} \quad (4.27)$$

4.2.1 Effective Velocity at Impeller Outlet

Best Match Point flowrate (Q_{BMP}), is when the direction of the fluid absolute velocity at the impeller outlet matches the designed flow direction. Mismatches in both the flow direction and amplitude will happen at flowrates below or above the Q_{BMP}. Therefore, an effective velocity should be used to replace C_2 at flowrate lower or higher than the flowrate corresponding to the Q_{BMP}.

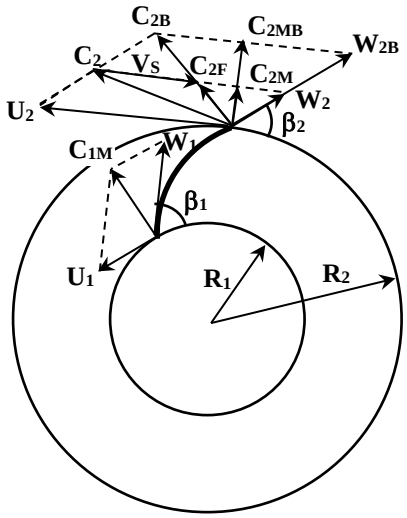

Figure 4.8 Velocity triangles at impeller outlet for $Q < Q_{BMP}$

As shown in Figure 4.8, when $Q < Q_{BMP}$, the fluid flow velocity outside the impeller is

$$C_{2F} = C_{2B}\frac{Q}{Q_{BMP}} \tag{4.28}$$

where C_{2B} is the absolute fluid velocity at the impeller outlet corresponding to the Q_{BMP}. The theoretical fluid velocity at the blade tip, C_2, is higher than C_{2F} where velocity difference causes a shear. The shear velocity can be calculated as

$$V_S = U_2\frac{Q_{BMP}-Q}{Q_{BMP}} \tag{4.29}$$

The projected velocity C_{2P}, is the projection of C_2 in the direction of C_{2B} which is the designed flow direction corresponding to the Q_{BMP}:

$$C_2^2 - C_{2P}^2 = V_S^2 - (C_{2P} - C_{2F})^2 \Rightarrow C_{2P} = \frac{C_2^2 + C_{2F}^2 - V_S^2}{2C_{2F}^2} \quad (4.30)$$

As shown in Figure 4.9, a recirculation occurs due to the shear rate. As a result, the theoretical kinetic energy will be reduced and only partially converted to static pressure. The recirculation is dependent on the shear velocity, the channel size, and the fluid viscosity, which can be estimated with a representative Reynolds number:

$$Re_C = \frac{\rho V_S D_C}{\mu} \quad (4.31)$$

where D_C is the representative impeller channel width at the outlet in flow direction which can be estimated as:

$$D_C = \frac{2\pi R_2}{Z_I} \sin \beta_2 - T_B \quad (4.32)$$

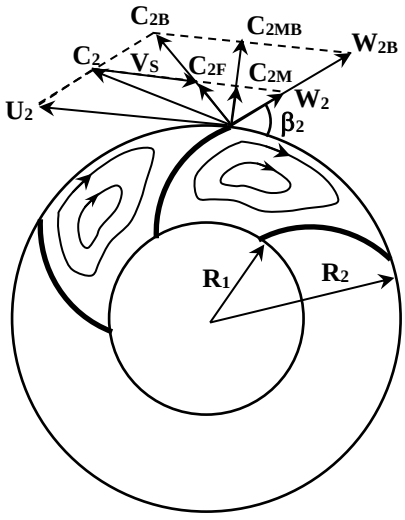

Figure 4.9 Recirculation in impeller channels for $Q < Q_{BMP}$

The shear effect is also dependent on the fluid viscosity. Therefore, the following correlation is proposed to estimate the effective velocity based on comparisons with experimental results

$$C_{2E} = C_{2F} + \sigma(C_{2P} - C_{2F}) \quad (4.33)$$

where σ is the slip factor proposed by Wiesner (1967) to account for the mismatch of the real outlet velocity with the ideal velocity. We propose the following correlation to better account for the mismatch:

$$\sigma = \frac{\left(\frac{\mu_W}{\mu_O}\right)^{0.5}}{1+0.02Re_C^{0.2}} \tag{4.34}$$

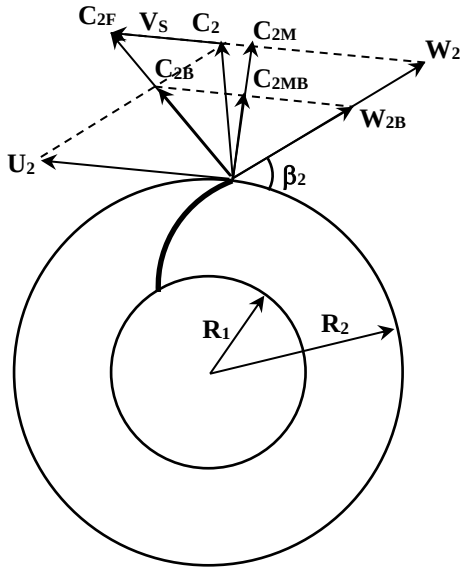

Figure 4.10 Velocity triangles at impeller outlet for $Q > Q_{BMP}$

As shown in Figure 4.10, when $Q > Q_{BMP}$, the fluid velocity outside of the impeller C_{2F} is identical to Equation (4.28), while the shear velocity is redefined as:

$$V_S = U_2 \frac{Q-Q_{BMP}}{Q_{BMP}} \tag{4.35}$$

The effective velocity, C_{2E}, is the projection of C_2 in the direction of C_{2B} which can be derived as:

$$C_2^2 - C_{2E}^2 = V_S^2 - (C_{2F} - C_{2E})^2 \Rightarrow C_{2E} = \frac{C_2^2+C_{2F}^2-V_S^2}{2C_{2F}^2} \tag{4.36}$$

Finally, the effective head of Euler equation when $Q > Q_{BMP}$ or $Q < Q_{BMP}$ becomes:

$$H_{EE} = H_E + \frac{C_{2E}^2-C_2^2}{2g} \tag{4.37}$$

4.2.2 Friction Losses

Flows in the impeller and diffuser are treated as channel flows. Similar as in a pipe flow, the friction loss in the impeller can be expressed as

$$H_{FI} = f_{FI} \frac{V_I^2 L_I}{2gD_I} \tag{4.38}$$

where f_{FI} is the friction factor, V_I is the representative fluid velocity, L_I is the channel length, and D_I is the representative hydraulic diameter of the channel. Likewise, the friction loss in the diffuser can be estimated as

$$H_{FD} = f_{FD} \frac{V_I^2 L_D}{2gD_D} \tag{4.39}$$

where f_{FD} is the friction factor, V_D is the representative fluid velocity, L_D is the channel length, and D_D is the representative hydraulic diameter of the channel. The Moody friction factors are functions of Reynolds number and relative roughness of the walls. Churchill's (1977) equations are used to calculate the friction factors across the transition from laminar flow to turbulent flow. The representative Reynolds numbers in the impeller and diffuser respectively are

$$Re_I = \frac{\rho V_I D_I}{\mu} \text{ and } Re_D = \frac{\rho V_D D_D}{\mu} \tag{4.40}$$

The representative diameter of the impeller channel is defined as

$$D_I = \frac{4Vol_I}{A_{SI}} \tag{4.41}$$

where Vol_I is the volume of an impeller channel and A_{SI} is the total wall area of an impeller channel. Similarly, the representative diameter of the diffuser channel is

$$D_D = \frac{4Vol_D}{A_{SD}} \tag{4.42}$$

where Vol_D is the volume of an impeller channel and A_{SD} is the total wall area of an impeller channel. The representative fluid velocity in the impeller channel is

$$V_I = \frac{Q+Q_{LK}}{A_I Z_I} \tag{4.43}$$

where Q_{LK} is the leakage flowrate which circulates through the impeller in addition to the ESP throughput, A_I is the representative impeller channel cross sectional area and Z_I is the impeller blade number. However, the representative fluid velocity in the diffuser channel is

$$V_D = \frac{Q}{A_I Z_I} \tag{4.44}$$

where A_D is the representative diffuser channel cross sectional area and Z_D is the diffuser vane number. A_I and A_D can be respectively defined as:

$$A_I = \frac{Vol_I}{L_I} \text{ and } A_D = \frac{Vol_D}{L_D} \tag{4.45}$$

4.2.3 Head Losses due to Turns

When fluid flows from impeller to diffuser and from diffuser back to the inlet of the next impeller, pressure head losses are caused due to the changes of flow directions. The head loss for the turn from the impeller to the diffuser (H_{TI}) and the head loss for the turn from the diffuser to the impeller (H_{TD}) can be respectively estimated as:

$$H_{TI} = f_{TI} \frac{V_I^2}{2g} \text{ and } H_{TD} = f_{TD} \frac{V_D^2}{2g} \tag{4.46}$$

where f_{TI} and f_{TD} are the local drag coefficients, and a value of 1.0 is used.

4.2.4 Leakage Losses

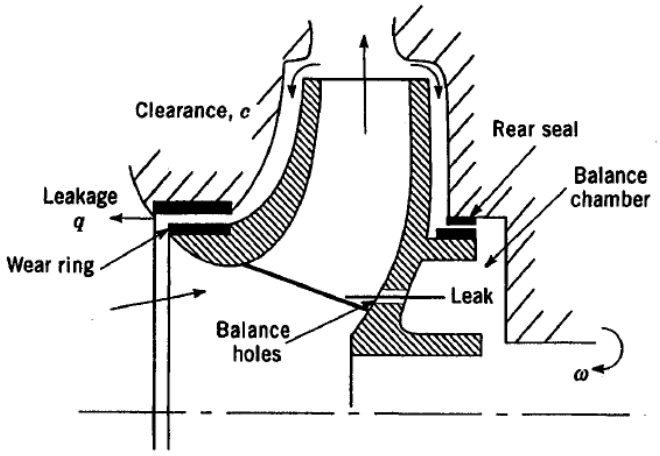

Figure 4.11 Balancing on axial thrust on impeller and leakage flow (from Tuzson "Centrifugal Pump Design", page 85)

Figure 4.11 describes locations of the leakage flow in an ESP. The pressure head difference across the leakage can be estimated as

$$H_{LK} = H_{IO} - \frac{U_2^2 - U_{LK}^2}{8g} \quad , \tag{4.47}$$

where H_{IO} is the head increase across the impeller and U_{LK} is the tangential velocity due to the impeller rotation at the leakage which is defined as

$$U_{LK} = R_{LK}\Omega \quad , \tag{4.48}$$

and R_{LK} is the radius corresponding to the leakage. The centrifugal force field on the front or back surface of the impeller acts against the pressure between the impeller and diffuser. Since the fluid rotation is caused by only one side, half of the tangential velocity of the impeller rotation may be counted. The head increase by the impeller can be estimated as

$$H_{IO} = H_{EE} - H_{FI} - H_{TI} \quad . \tag{4.49}$$

The head loss across the leakage consists of contraction, expansion, and friction components:

$$H_{LK} = 0.5\frac{V_L^2}{2g} + 1.0\frac{V_L^2}{2g} + f_{LK}\frac{V_L^2 L_G}{2gS_I} \quad (4.50)$$

where L_G is the leakage channel length and S_L is the leakage width. Therefore, the fluid velocity through the leakage can be considered as:

$$V_L = \sqrt{\frac{2gH_{LK}}{f_{LK}\frac{L_G}{S_I}+1.5}} \quad (4.51)$$

Assuming smooth leakage channel, the friction factor f_{LK} can be estimated based on Reynolds number:

$$Re_L = \frac{\rho V_L D_L}{\mu} \quad (4.52)$$

Then, the leakage flowrate can be calculated as

$$Q_{Lk} = 2\pi R_{LK} S_L V_L \quad (4.53)$$

4.2.5 Model Comparison with Single-Phase Tests

The model is coded using VBA. After inputting all needed parameters, namely the fluid properties and the pump geometry, as well as the pump rotation speed as shown in Figure 4.12. While the fluid properties may be obtained from the lab, most of the pump geometry parameters can be obtained from the manufacturer, except the leakage parameters which may be estimated. To consider the wearing, the impeller outside radius is shortened by about 1.9 mm. In addition, roughness assumed to alter from 300 μm to 500 μm. The user has to guess the BMP to match the resulted curve to the manufacturer curve, preferably from water experiments. If there is a deviation, the user needs to change the BMP until the best match is achieved. In this study, results for the model with water is compared to the experimental data in Figure 4.13. Since our pump has deteriorated as shown earlier in Figure 2.13 it is not meaningful to compare the model with the manufacturer's curve. Moreover, the ESP average boosting pressure seems deviating consistently

compared to the stage pressure variation. Therefore, the mechanistic model is compared to the ESP average boosting pressure. After several attempts, the BMP is set to be 3400 bpd and the model was able to match water curves as shown in Figure 4.13.

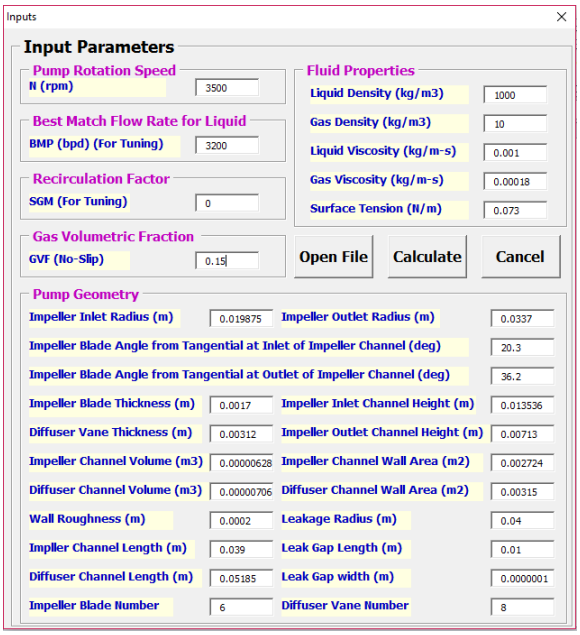

Figure 4.12 ESP model GUI

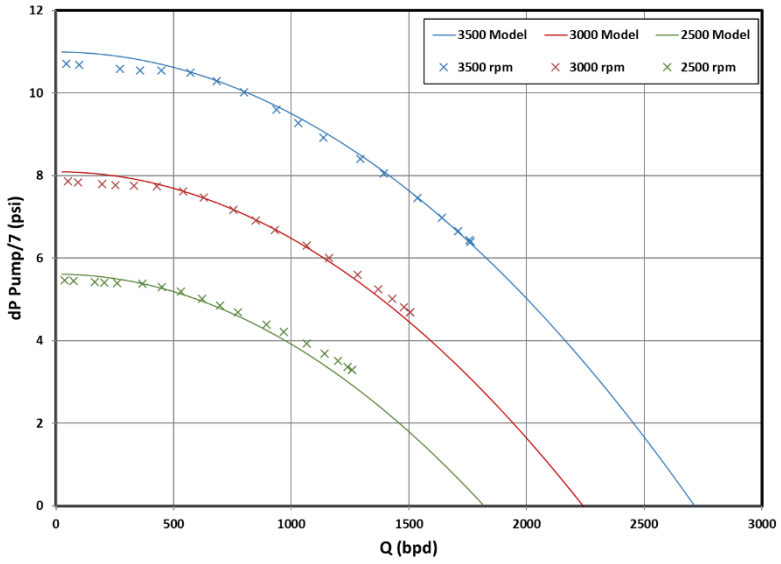

Figure 4.13 Tuning ESP model to match water experiments

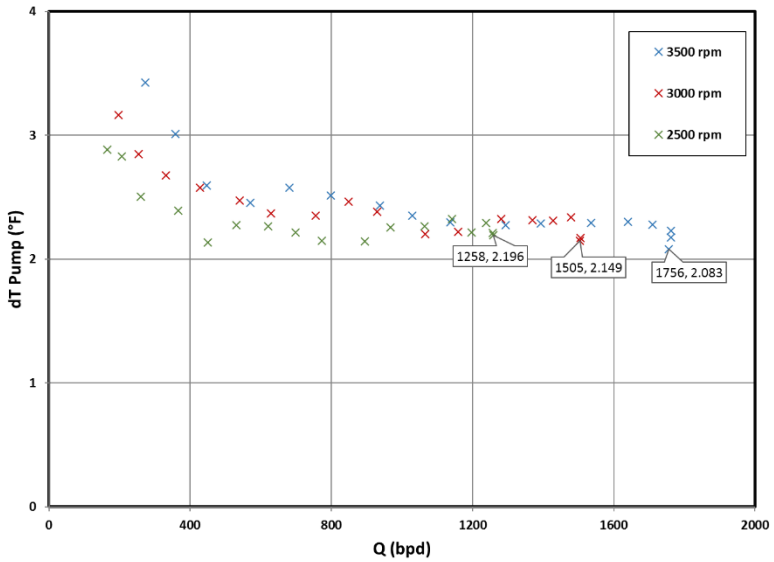

Figure 4.14 Temperature rise across the ESP with water

Next, we compared the model predictions for ND20 oil with the correspondent experiment results. Correction factors of Stepanoff (1949) and Turzo et al. (2000) are examined and compared to our proposed model. Unfortunately, Ippen (1946) correlations cannot be used in our study since the value of R_D is out of the range of his charts, and extrapolation is not recommended when dealing with empirical correlations. To use the applicable correlations, we may need to redefine the BEP since the water performance curve does not match the manufacturer curve. Originally, the BEP corresponds to a flowrate of 1750 bpd and a head of 19.15 ft, which results in a specific speed of 2731. We used the analogy from Stepanoff's (1949) principle for specific speed with viscous flow, we assume that the head decreases as a result of deterioration such that its specific speed at the BEP remains constant. Using Equation 1.4 and experimental results for water at 3500 rpm, a flowrate of 1565.4 bpd and a head of 17.8 ft correspond to our new BEP. However, a better approach is to find the lowest temperature rise across the ESP and that should correspond to the current BEP as shown in Figure 4.14. The current BEP matches the original value for almost all rotational speeds using affinity laws. For 3500 and 3000 rpm, the BEPs are clearly 1756 and 1505

bpd, respectively. However, that is not clear for 2500 rpm, since many points share the same temperature rise with differences as small as 0.06 °F, but since the BEPs for the other rotational speed are the identical to the manufacture's curve, we can extend that to the BEP at 2500 which is 1254 bpd. Next, we redefined the N_s at the BEP from our experiments, which is around 3307.

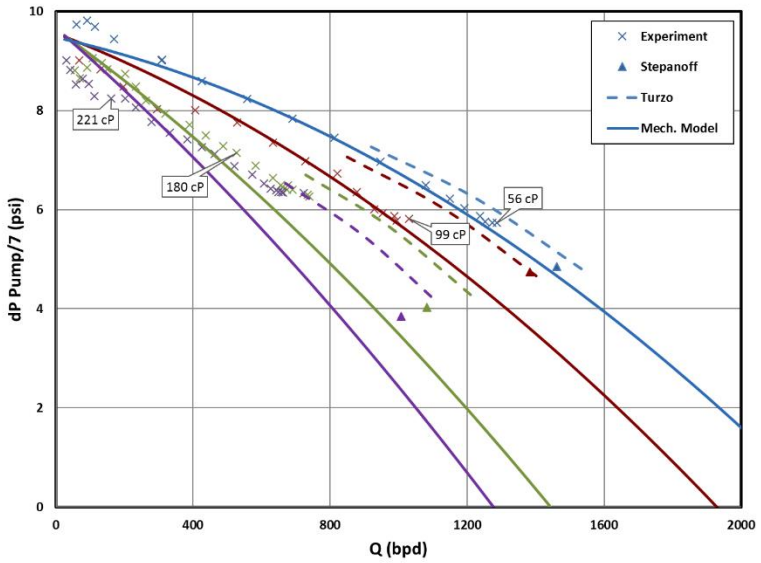

Figure 4.15 Model comparison with available correlations and with experimental data for old ND20 oil at 3500 rpm

Comparison to experiments for 4 viscosities at 3 different rotational speeds with the old batch of ND20 oil are shown in Figure 4.15 through Figure 4.17. Turzo's correlation is for 4 points as discussed earlier while Stepanoff's correction factor is at the BEP only. On the other hand, our newly developed model covers the whole range of the performance curve which is a great advantage. Turzo's curves always over-predict the performance but the gap becomes smaller at higher viscosities. On the other, hand, Staponoff's correlation cannot be evaluated since the predicted points were not achievable experimentally. However, compared to Turzo, Stepanoff's model prediction is always lower. Our mechanistic model predicts the performance very well for low and medium viscosities. As oil viscosity increases beyond 100 cP, deviation is clearer

especially at high flowrates. In general, 3500 rpm predictions are better compared to the other rotational speeds.

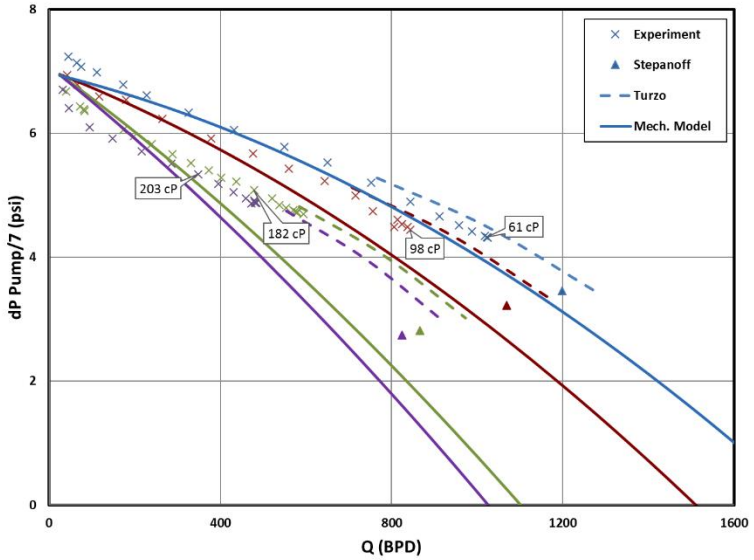

Figure 4.16 Model comparison with available correlations and with experimental data for old ND20 oil at 3000 rpm

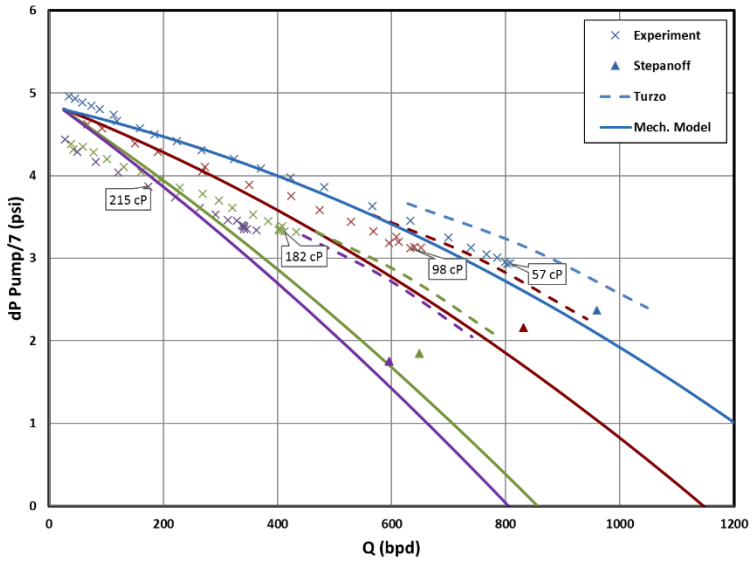

Figure 4.17 Model comparison with available correlations and with experimental data for old ND20 oil at 2500 rpm

4.2.6 Model Comparison with Emulsion Tests

Emulsion rheology is predicted first using the proposed model, then the resulted effective viscosity is used in the ESP performance mechanistic model as a single phase oil. For density, the no-slip density is assumed. Since the old ND20 emulsion results are dropped out in the rheology modeling part, then those results are also dropped out in the comparison. Therefore, the ND20 and Isopar V oils' results are used to compare the ESP performance model results. We can observes in Figure 4.18 that for relatively low viscosities, the proposed model almost matches the experimental results. As viscosity increases higher than 60 cP, the model deviates at high flowrates. In all cases, the model prediction is perfect for low flowrates. A clear observation in Figure 4.19 for 30% water fraction, the experimental performance is clearly higher than the prediction model. This is possibly due to the higher shear rate at the stage condition compared to the PV, and the actual effective viscosity is much lower than 54 cP. The deviation for all rotational speeds at low flowrates is also obvious. Figure 4.20 shows minor deviation for high viscosities at 3500 rpm, but the deviation is severe as rotation speed decreases. When viscosity drops after the inversion point, the model starts to match the results with a similar trend but also with a clear gap. Since 88 °F experiments set is an intermediate, it is not showing to validate the proposed ESP performance model in this section.

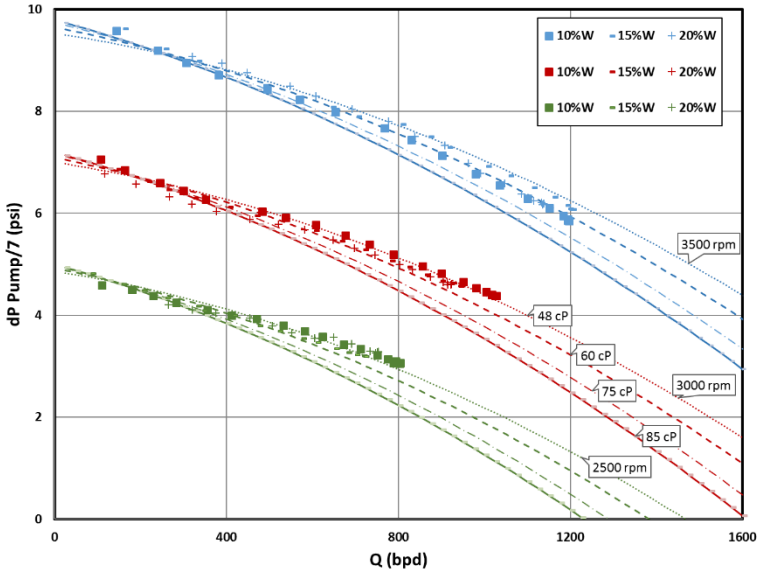

Figure 4.18 Model comparison with experimental data for the new ND20 oil emulsion at 100 °F

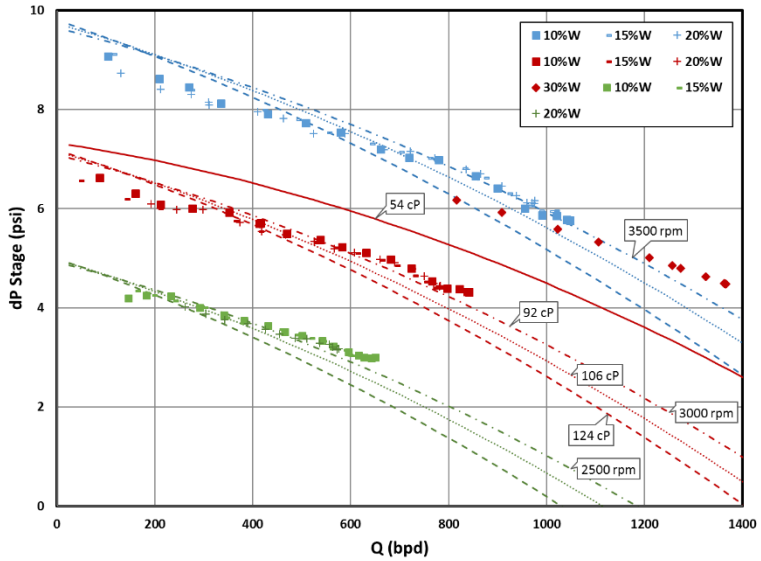

Figure 4.19 Model comparison with experimental data for the new ND20 oil emulsion at 88 °F

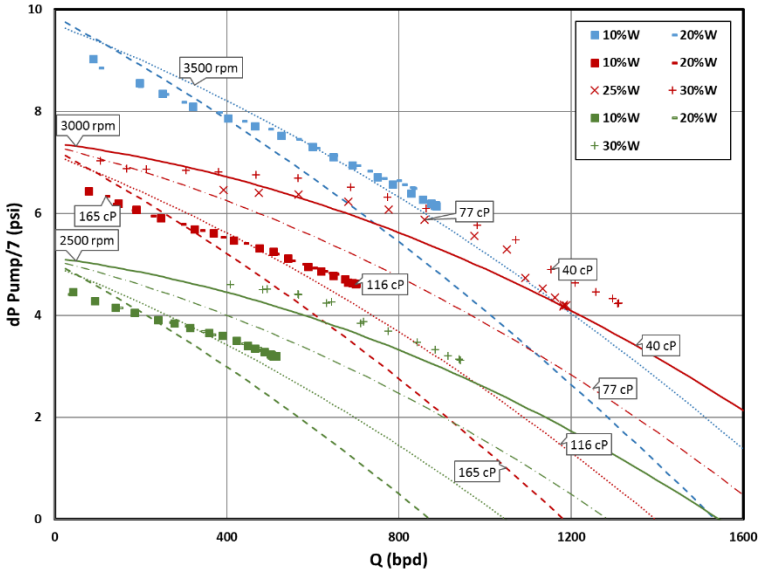

Figure 4.20 Model comparison with experimental data for the new ND20 oil emulsion at 80 °F

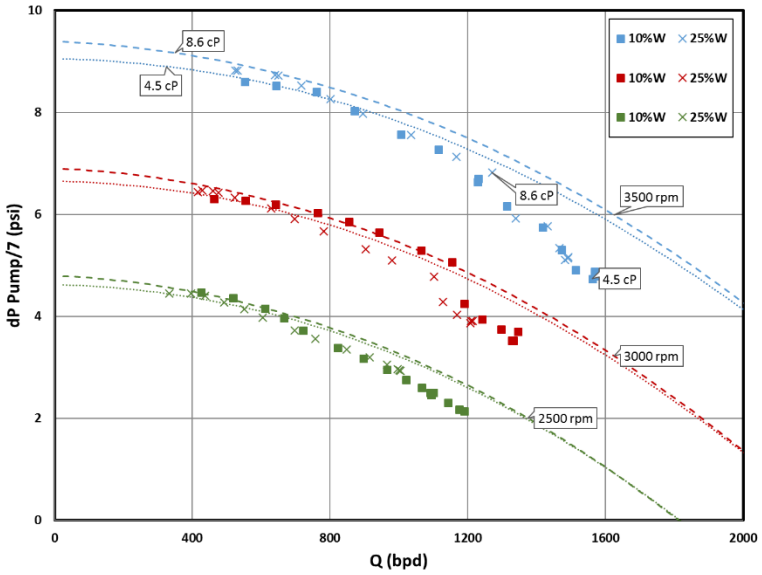

Figure 4.21 Model comparison with experimental data for Isopar V emulsion at 95 °F

Since the predicted effective viscosity for Isopar V emulsion has a narrow range, two points of are selected to distinguish the differences between any two curves. A unique observation can be seen in Figure 4.21, which is the performance curve for 8.6 cP is better than that for 4.5 cP, corresponding to 25% and 10% water fractions, respectively. This is possibly due to the increase in the emulsion density causes the pump boosting pressure to increase while the viscosity increase

effect is insignificant compared to density. Since the match was perfect with water, Isopar V emulsion behaves worse than the proposed model. This may indicate that the viscosity is much higher than the ones derived from the PV. This also agrees with our emulsion rheology model principle, which suggests that the effective viscosity increases with flowrate increase.

CHAPTER 5

CONCLUSIONS AND RECOMMENDATIONS

In this study, three research approaches, experimental measurement, numerical simulation, and mechanistic modeling, are utilized to perform a comprehensive study of ESP performance under viscous flow for both single-liquid and liquid-liquid conditions. The following are the conclusions and recommendations for future researches.

5.1 Conclusions

5.1.1 Experimental Study

1. The measured ESP stage pressure increment with tap water flow matches the previous study results of Croce (2014) which validates the experimental setup used in this study. On the other hand, the match to catalog performance curves are close at medium flowrates but lower at high and low flowrates. This may be due to the ESP wearing after a long-time use. The third stage also seems to suffer from rust and wear out.
2. ESP stage performance degrades clearly with viscosity increase, due to higher mechanical energy loss into heat as a result of shear stress increase.
3. Emulsion stability is affected by flowrate, oil properties, flow loop setup, ESP rotation speed, etc. Once the emulsion becomes water continuous, it loses its rheology stability especially at low flowrates.
4. Viscosities derived from the PV are acceptable for single phase compared to the lab

rheometer and the match is perfect for water. For emulsion, the effective viscosity from the PV matches the estimated viscosity very well at the stage condition by conducting the effective viscosity validation experiments. However, when moving closer to the inversion point and when the measured effective viscosity is beyond 300 cP, the validated effective viscosity values are lower by up to 40% at the stage condition. This may be due to high shear rates delivered to emulsion causing shear thinning effect and the effective viscosity to be lower.

5. Non-Newtonian behavior was not significant in our experiment. However, slight deviations were observed but that can be due to emulsion instability within the flow loop. Another possible reason is that the shear rate was not high enough to cause significant shear thinning effect on emulsion.
6. FBRM and PVM were utilized to quantitatively measure the droplets of the dispersed phase, in order to find the relationship between the emulsion effective viscosity and droplet sizes. However, the PVM failed to perform due to sticking of the emulsion on the probe surface. On the other hand, the FBRM was able to capture the average chord lengths of the dispersed phase, but the results are inconsistent in terms of the average dispersed phase droplet size change with rotational speed. This can be due to the probe position at which the droplet coalescence rate is higher as water fractions approach the inversion point.

5.1.2 CFD Simulation

CFD simulations are conducted on ESP performance under single-phase viscous fluid flow using two approaches. The 3D, steady-state RANS equations with standard SST turbulence models are solved in ANSYS CFX using the frozen-rotor technique.

1. For the first approach, single-phase flow in a single channel of 7 consecutive ESP stages was modeled and results were comparable to corresponding experimental data. Flow structures inside ESP impeller and diffuser channels were analyzed. At pump BEP, the boosting pressure decreases 30-40% when oil viscosity increases from 10 cP to 100 cP. ESP becomes ineffective when oil viscosity is higher than 200 cP. With oil viscosity increase, pump *H-Q* performance curve becomes more linear. CFD simulation reveals that the recirculation flow at impeller blade trailing edge is more prominent at lower liquid flowrates. Simulation results are about 20% higher than experiments.
2. For the second approach, a 3D CFD scheme was implemented on a complete three-stage ESP geometry to simulate the pressure increment under various flow conditions of single-phase and two-phase fluids. By use of structured hexahedral grids and the frozen-rotor technique, the mesh independence and numerical accuracy were verified. Then, for oil-water simulations, the solver was not able to reflect the emulsion rheology. Therefore, both liquids are assumed to be a single-phase mixture with appropriately defined physical properties. Simulation results are mostly 40% higher than experiments especially for high oil viscosities which can be partially due to stage wear out.

5.1.3 Modeling

1. A new approach is proposed which is composed of a factor and a set of equations are proposed, based on dimensionless numbers that reflect several effects on the emulsion rheology at the ESP stage condition, including Reynolds number for turbulence effect, Weber number for mixing effect, and Strouhal number for shearing effect.
2. A comprehensive mechanistic model for predicting ESP stage pressure increment is developed based on Euler's equation for centrifugal pumps. For single-phase liquid and for oil-water emulsion, the effects of fluid viscosity and emulsion effective viscosity on ESP boosting pressure is incorporated.
3. Based on the best match flowrate concept, Euler equation for centrifugal pump is modified at the ESP impeller outlet. Losses such as friction, recirculation and flow turns are considered in the model.

5.2 Recommendations

The following recommendations may be considered in future studies:

1. For experimental facility, disassemble the ESP and check its condition. Then, replace the stages if the wear out is significant. Find a better heat exchanger to maintain the fluid temperature so that the effect of the ambient temperature is minimized and having it should be positioned horizontally. Replace all carbon steel pipes with stainless steel pipes to minimize rusty particles. Use new oil for each experiment to minimize contamination. Set the mass flowmeter horizontally to minimize emulsion instability effect. Use shorter temperature probes for more

accurate measurements. Since PV may not represent the effective viscosity at the stage condition, a feasibility study of an online viscometer can show if that is a better way to estimate the effective viscosity. Although the shear rate is obviously different, online viscometer does not require a development section and can be placed close to the ESP discharge.

2. For single phase, utilize the conservation of energy equations by selecting the heat transfer model as non-isothermal. Oil viscosity is a strong function of temperature and the actual temperature and the corresponding viscosity at the stage condition may be unknown. Conducting transient CFD simulations may improve the single phase results. Steady state simulation ignores many terms related to time. Better results may be achieved by considering the transient terms.
3. In CFD simulation for emulsion, incorporate a user defined model such as Cross model to account for the shear rate effect on the effective viscosity of emulsion (Chochua et al. 2018).
4. More data are required to validate the emulsion rheology model and to improve the coefficients, by changing the interfacial tension, oil viscosity, rotational speed, and other variables. If the effective viscosity is higher than 200 cP, the PV deviates considerably from the stage condition viscosity. Therefore, viscosity validation experiment is a good method to estimate the effective viscosity, by matching the head of known oil viscosity to the emulsion head at the same flowrate. Conduct experiments for viscosities higher than 200 cP so the effect of shearing may be observed.

NOMENCLATURE

BEP	best efficiency point
BMP	best match point
CFD	Computational Fluid Dynamics
DAQ	data acquisition system
ESP	electric submersible pump
GUI	graphical user interface
GVF	gas volumetric fraction
PV	pipe viscometer
rpm	revolution per minute
VSD	variable speed drive
A_{SD}	diffuser channel total wall area
A_{SI}	impeller channel total wall area
C_1	absolute fluid velocity at impeller inlet
C_{1M}	meridional velocity at impeller inlet
C_{1U}	fluid tangential velocity at impeller inlet
C_2	absolute fluid velocity at impeller outlet
C_{2B}	absolute fluid velocity at impeller outlet corresponding to BMP
C_{2E}	effective velocity at impeller outlet
C_{2F}	fluid velocity outside impeller
C_{2M}	meridional velocity at impeller outlet

C_{2P}	projected velocity
C_{2U}	fluid tangential velocity at impeller outlet
C_D	drag coefficient
C_H	head correction factor
C_L	lift coefficient
C_q	flowrate correction factor
C_η	efficiency correction factor
$\overline{d}$	average droplet sizes
d	impeller diameter
D	mixer blade length
D_C	representative impeller channel width at outlet
D_D	diffuser representative (hydraulic) diameter
D_I	impeller representative (hydraulic) diameter
D_L	leakage diameter
dP	differential pressure
f	friction factor
$\vec{F}$	interfacial force vector
f_{FD}	friction factor in diffuser
f_{FI}	friction factor in impeller
f_{LK}	leakage friction factor
f_{TD}	local drag coefficient in diffuser
f_{TI}	local drag coefficient in impeller
$\vec{g}$	gravity acceleration vector

h	channel height
H	pump head
H_{BEP}	head at BEP
H_E	Euler's head
H_{EE}	effective Euler's head
H_{FD}	head loss due to friction in diffuser
H_{FI}	head loss due to friction in impeller
H_{IO}	head increase across impeller
H_{LK}	pressure head difference across leakage
H_{oil}	pump head with oil
H_{TD}	head loss due to turn from diffuser to impeller
H_{TI}	head loss due to turn from impeller to diffuser
H_{vis}	pump head with viscous fluid
H_{water}	pump head with water
$\bar{\bar{I}}$	identity matrix
k	turbulent kinetic energy
L_D	diffuser channel length
L_G	leakage channel length
L_I	impeller channel length
$\dot{m}$	mass flowrate
n	phase number
N	rotational speed
N_s	specific speed

P	pressure
P_2	shaft power
P_{hyd}	hydraulic power
Q	volumetric flowrate
q_{BEP}	flowrate at BEP
Q_{BMP}	volumetric flowrate at BMP
Q_{LK}	leakage volumetric flowrate
q_{vis}	viscous fluid flowrate
q_{water}	water flowrate
R_1	radius of impeller inlet
R_2	radius of impeller outlet
R_D	Reynolds number by Ippen
Re	Reynolds number
Re_C	recirculation effect Reynolds number
Re_D	Reynolds numbers in diffuser
Re_I	Reynolds numbers in impeller
Re_L	leakage Reynolds number
$Re_{Stepanoff}$	Reynolds number by Stepanoff
Re_{Tank}	Reynolds number for mixing in tank
R_{LK}	radius corresponding to leakage
S_L	leakage width
St	Strouhal number
t	time

T	temperature or torque
T_B	blade thickness projected to radial direction
$\vec{u}_i$	phase velocity vector
U_1	impeller tangential velocity at inlet
U_2	impeller tangential velocity at outlet
U_{LK}	tangential velocity due to impeller rotation at leakage
v	velocity
V	volume
V_D	representative fluid velocity in diffuser
V_I	representative fluid velocity in impeller
V_L	fluid velocity at leakage
Vol_D	diffuser channel volume
Vol_I	impeller channel volume
V_S	shear velocity
W_1	relative velocity with respect to impeller at inlet
W_2	relative velocity with respect to impeller at outlet
We	Weber number
We_{Tank}	Weber number for mixing in tank
y_{I1}	impeller inlet height
y_{I2}	impeller outlet height
Z_1	impeller blade number
Δp_{oil}	boosting pressure with oil
Δp_{total}	boosting pressure across impeller

Δp_{water}	boosting pressure with water
η	efficiency
μ	dynamic viscosity
μ_{eff}	effective viscosity
μ_o	oil dynamic viscosity
μ_t	turbulent viscosity
μ_w	water dynamic viscosity
β_1	blade angle from tangential at impeller inlet
β_2	blade angle from tangential at impeller outlet
γ_{oil}	oil specific gravity
γ_{water}	water specific gravity
η_{vis}	efficiency with viscous fluid
η_{water}	efficiency with water
ν	kinematic viscosity
ρ	density
σ	interfacial tension or dimensionless number
τ	torque
ω	angular velocity
Ω	angular speed
φ	flow coefficient
ψ	head coefficient
$\bar{\bar{\tau}}$	stress-strain tensor

ε	turbulent energy dissipation rate per unit mass

BIBLIOGRAPHY

1. Amaral, G., Estevam, V., Franca, F. A. (2009, May 1). On the Influence of Viscosity on ESP Performance. Society of Petroleum Engineers. https://doi.org/10.2118/110661-PA
2. Ansys, 2015. CFX-Solver Modeling Guide, ANSYS Inc., Canonsburg, PA.
3. Asuaje, M., Bakir, F., Kouidri, S. et al. 2005. Numerical modelization of the flow in centrifugal pump: volute influence in velocity and pressure fields. *International journal of rotating machinery* 2005(3): 244-255.
4. Banjar, H. 2012. Experimental Study of Liquid Viscosity Effect on Two-Phase Stage Performance of Electric Submersible Pumps. MSc Thesis. The University of Tulsa.
5. Boxall, J., Koh, C., Sloan, E., et al. 2012. Droplet Size Scaling of Water-In-Oil Emulsions under Turbulent Flow. *Langmuir* 28: 104–110.
6. Bradshaw, P. 1996. Turbulence modeling with application to turbomachinery. *Progress in Aerospace Sciences* 32(6): 575–624.
7. Brito, R., Pereyra, E., Sarica, C. 2014. Experimental Study to Characterize Slug Flow for Medium Oil Viscosities in Horizontal Pipes. BHR Group.
8. Cardle North America Inc. 2014. Computational Fluid Dynamics, Introductory Seminar. Online Course.
9. Chochua, G and Shirazi, S. 2018. Advances in erosion wear life prediction using CFD. ASME 5th Joint US-European Fluids Engineering Summer Conference.
10. Churchill, S.W. 1977. Friction-factor equation spans all fluid-flow regimes. *Chemical engineering* 84(24): 91-92.

11. Croce, D. 2014. Study of Oil/Water Flow and Emulsion Formation in Electrical Submersible Pumps. MS Thesis, The University of Tulsa.
12. Dang, N. 2014. Prediction of Transition Bands for Oil/Water Pipe Flow. MS Thesis, The University of Tulsa.
13. Drew, D.A. and Lahey, R.T. 1979. Application of general constitutive principles to the derivation of multidimensional two-phase flow equations. *International Journal Multiphase Flow* 5(4): 243–264.
14. Gülich, J. 1999. Pumping highly viscous fluids with centrifugal pumps. *World Pumps* (395): 30-34.
15. Gulich. J. 2007. *Centrifugal Pumps.* Springer.
16. Hydraulic Institute. 1955. *Determination of Pump Performance when Handling Viscous Liquid,* tenth edition.
17. Ippen, A. 1946. The Influence of Viscosity on Centrifugal Pump Performance. Trans. ASME 68: 823-848.
18. Kokal, S. L. 2005. Crude Oil Emulsions: A State-Of-The-Art Review. Society of Petroleum Engineers. https://doi.org/10.2118/77497-PA
19. Kolmogorov, A. 1949. On the Disintegration of Drops in a Turbulent Flow. *Dok. Akad. Nauk* (66): 825–828.
20. Launder, B.E. and Spalding, D.B. 1974. The numerical computation of turbulent flows. *Computer Methods in Applied Mechanics and Engineering* 3(2): 269-289.
21. Legendre, D. and Magnaudet, J. 1998. The lift force on a spherical bubble in a viscous linear shear flow. *Journal of Fluid Mechanics* 368: 81–126.

22. Li, W., Su, F., Xue, J., et al. 2002. Experimental Investigations of Performance of a Commercial Centrifugal Oil Pump. *World Pumps* 2002 (425): 26-28.
23. Li, W.G. 2014. Mechanism for onset of sudden-rising head effect in centrifugal pump when handling viscous oils. *Journal of Fluids Engineering* 136 (7): 074501.
24. Menter, F.R. 1994. Two-equation eddy-viscosity turbulence models for engineering applications. *AIAA Journal* 32(8):1598-1605.
25. Mohan, R. 2014. *ME 7053 Oil-Water Dispersion.* Lecture Notes, The University of Tulsa.
26. Ngan, K. 2010. Phase Inversion in Dispersed Liquid-liquid Pipe Flow. MS Thesis, University College London.
27. Patankar, S.V. and Spalding, D.B. 1972. A calculation procedure for heat and mass transfer in three dimensional parabolic flows. *International Journal of Heat and Mass Transfer* 15(10): 1787-1806.
28. Peters, F. and Arabali, D. 2013. Interfacial Tension between Oil and Water Measured with a Modified Contour Method. *Colloids and Surfaces A: Physicochemical and Engineering Aspects*. 426: 1–5.
29. Prado, M. 2014. *PE 7003 - Artificial Lift Methods.* Lecture Notes, The University of Tulsa.
30. Schiller, L. and Naumann, A. 1933. Fundamental calculations in gravitational processing. *Zeitschrift Des Vereines Deutscher Ingenieure* 77: 318-320.
31. Shinnar, R. 1961. On the behaviour of liquid dispersions in mixing vessel. *Journal of Fluid Mechanics*. (10):259-268
32. Solano, E. 2007. ESP Performance for Viscous Fluids –Literature Review. Internal Technical Report. Tulsa University Artificial Lift Project (TUALP). The University of Tulsa.

33. Solano, E. 2009. Viscous Effects on the Performance of Electro Submersible Pumps (ESP's). MS Thesis, The University of Tulsa.

34. Stepanoff, A.J. 1949. How centrifugals perform when pumping viscous oils. *Power.* 85-87.

35. Stepanoff, A.J. 1957. *Centrifugal and Axial Flow Pump: Theory, Design, and Application,* second edition. New York: John Wiley & Sons.

36. Turzo, Z., Takacs, G. and Zsuga, J. 2000. A Computerized Model for Viscosity Correction of Centrifugal Pump Performance Curves. 47th Southwestern Petroleum Short Course, Texas.

37. White, F.M. 1998. Internal Versus External Viscous Flows. In Fluid Mechanics. Rhode Island: McGraw-Hill.

38. Wiesner, F.J. 1967. A review of slip factors for centrifugal impellers. *ASME Journal of Engineering for Power* 89(4):558-566.

39. Wilcox, D.C. 1998. *Turbulence modeling for CFD,* second edition. La Cañada, California: A DCW Industries Inc.

40. Wu, D., Yan, P., Chen, X., et al. 2015. Effect of trailing-edge modification of a mixed-flow pump. ASME Journal of Fluids Engineering, 137(10): 101205.

41. Yakhot, V., Orszag, S.A., Thangam, S. et al. 1992. Development of turbulence models for shear flows by a double expansion technique. *Physics of Fluids A: Fluid Dynamics* 4(7): 1510-1520.

42. Yaron, I., Gal-Or, B. 1972. On viscous flow and effective viscosity of concentrated suspensions and emulsions. *Rheologica Acta.* 11(3–4): 241–252.

43. Zande, V., Muntinga, J. and Broek, W. 1999 The effects of production rate and choke size on emulsion stability." *EXPL-6-MZ, INGEPET '99*.

44. Zhou, L., Shi, W., Lu, W. et al. 2012. Numerical investigations and performance experiments of a deep-well centrifugal pump with different diffusers. *Journal of Fluids Engineering* 134: 071102.

APPENDIX A

EQUIPMENT AND INSTRUMENT SPECIFICATIONS

Table A.1 TUALP viscous liquid flow loop equipment specifications

Equipment	Model	Capacity	Purpose
ESP pump	REDA DN-1750	BEP:1750 bpd, 3500 rpm	Testing bench
Electric motor	Baldor Reliance	100 hp	Drive motor
Air compressor	KOBALT	2.6 cfm, 90 psi	Pressurizing loop
Variable speed drive	Centrilift 2250-3VT	–	Altering rotational speed
ESP thrust chamber	–	–	Thrust bearing box
Choke valve	Cyclonic Valve TDC2050	–	Flowrate control
Plate Heat Exchanger	Paul Mueller Company AT10G F-20	10 gpm hot side 14.4 gpm cold side	Controlling fluid temperature

Table A.2 TUALP viscous flow loop instrumentation specifications

Transducer	Model	Range
Temperature transmitter	Emerson Rosemount 3144	-50℃ – 85℃
Absolute pressure transmitter	Emerson Rosemount 2051S	0 to 500 psig
Differential pressure transmitter	Emerson Rosemount 3051SD	0 to 50 psig
Coriolis liquid flowmeter 1	Micro Motion DS300	0 to 7000 lb/min
Coriolis liquid flowmeter 2	Micro Motion CMF100	0 to 1000 lb/min
Flowmeter 1 transmitter	Micro Motion 2700C	
Torque/rotary speed sensor and monitor	Sensor: Lebow model 1805-5K Monitor: Lebow model 7541	0 to 22000 rpm 0 to 5000 lbf-in

Table A.3 TUALP viscous flow loop DAQ specifications

Device	Features
Data processing computer	Dell OptiPlex 980 i5- 650 CPU @ 3.2 GHz, RAM: 4GB, HD: 500GB
National Instruments cFP-AI-111	• 16 single-ended analog current input channels • Three input ranges: ±20, 0–20, and 4–20 mA • 16-bit resolution • Three filter settings: 50, 60, and 500 Hz • Hot swappable • 2300 V_{rms} transient overvoltage protection • -40 to 70 °C operation
National Instruments cFP-AO-200	• Eight 0–20 or 4–20 mA outputs • 0.5 mA over ranging • 12-bit resolution • Up to 1 kΩ load impedance (with 24 V loop supply) • Indicators for open current loops • Short-circuit protection • 2300 V_{rms} transient overvoltage protection between the inter-module communication bus and the I/O channels • -40 to 70 °C operation • Hot plug-and-play
National Instruments cFP-1804	• Network interface: 10 BaseT and 100 BaseTX Ethernet, IEEE802.3, 10/100 Mbps • One RS-232 (DCE) serial port, 300 to 115200 bps • 11 to 30 VDC, 20W • 2300 Vrms transient overvoltage protection • -40 to 70 °C operation

Figure A.1 through

Figure A.12 are the equipment used in this study. Some were used by Solano (2009) or Banjar (2012) while others are obtained for this study.

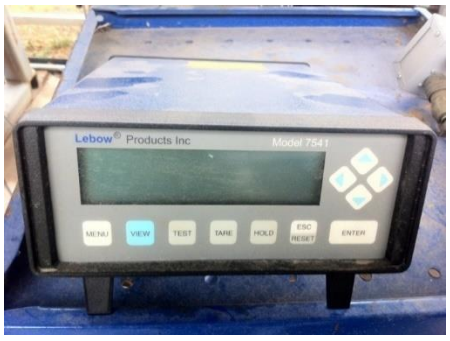

Figure A.1 Signal conditioner

Figure A.2 Electric motor

Figure A.3 Variable speed drive

Figure A.4 Choke valve

Figure A.5 Heat exchanger

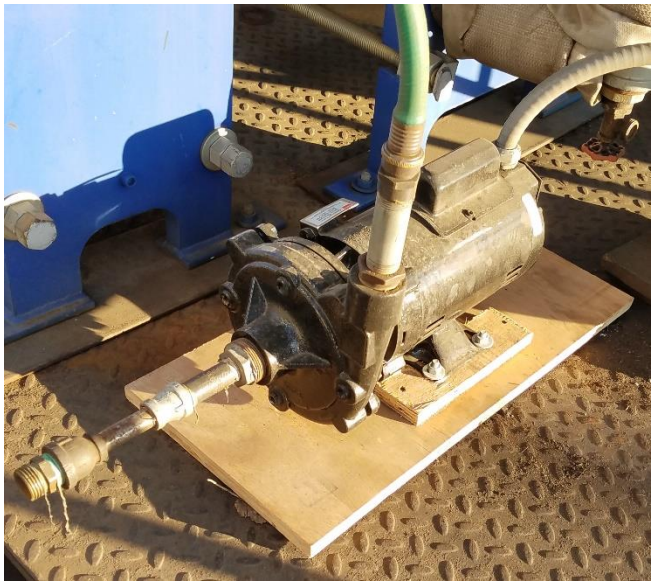

Figure A.6 Heat exchanger pump

Figure A.7 Mass flowmeter

Figure A.8 Densitometer

Figure A.9 Rotational viscometer

Figure A.10 Thermostatic bath and circulator for rotational viscometer

Figure A.11 Du Noüy ring tensiometer

Figure A.12 Thermostatic bath and circulator for

Figure A.13 Capillary surface tension apparatus

APPENDIX B

MASS FLOWMETER SELECTION AND CALIBRATION

There are two models of Micro Motion mass flowmeters. CMF100 is for low flowrate range and DS300 is for higher flowrate applications. In fact, the range of the smaller flowmeter is sufficient for our application with a higher accuracy (± 0.10%) as opposed to the larger flowmeter accuracy (± 0.15%). However, its density measurement deviates significantly from the expected value of water as shown in Figure B.1. Therefore, the sensor measurement error is beyond acceptable. The large flowmeter shows satisfactory density measurements compared to the lab results with small discrepancy. Density lower than water is because of the residual of mineral oil used in the loop before water experiments, such as Isopar V or ND20. Therefore, the large flowmeter is used throughout the rest of the experiments.

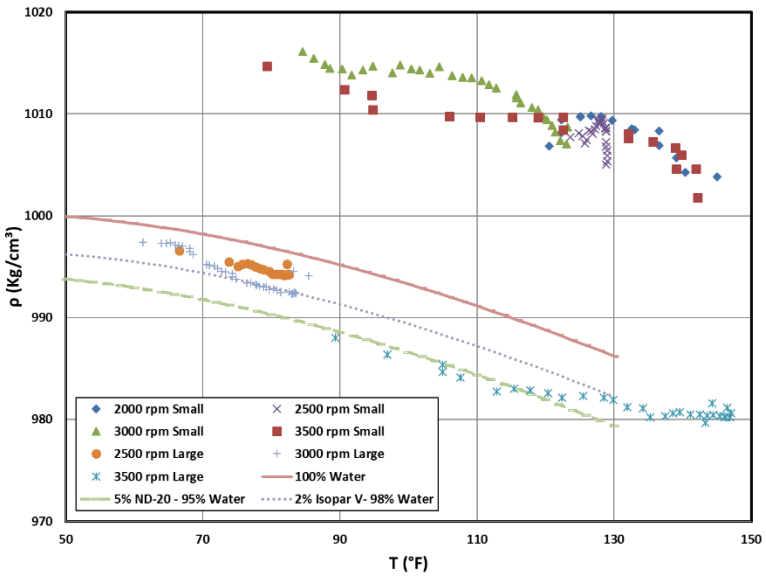

Figure B.1 Large and small flowmeter density measurements vs. lab densitometer readings

It is difficult to validate the mass flowrate measurements directly, but by means of the PV differential pressure measurements, we were able to find an indirect way using Equation (2.6). The validation approach was performed by running fluid through the large flowmeter then diverting flow to the small flowmeter and readings are recorded for both runs. Since the small flowmeter has a smaller inner diameter (less than 2 inch), it is expected that the mass flowrate to be lower once the flow passes through it. The same is true for the pressure drop across the PV, assuming the fluid is Newtonian. On the other hand, viscosity and density should not change, provided that fluid passing both flowmeters have the same temperature. Therefore, the following relation should be satisfied, and results are shown in Table B.1:

$$\left.\frac{dP}{\dot{m}}\right|_{Flowmeter\ 1} = \left.\frac{dP}{\dot{m}}\right|_{Flowmeter\ 2} \tag{B.1}$$

Table B.1 Mass flowmeter readings validation

Parameter	**Case 1**		**Case 2**	
	Large Flowmeter	**Small Flowmeter**	**Large Flowmeter**	**Small Flowmeter**
Temperature (°F)	84.1	83.9	83.3	83.7
Mass Flowrate (lb/min)	54.5	37.9	36.5	26.0
Pressure Drop (Pa)	2798.0	1965.0	1855.0	1310.0
$\frac{dP}{\dot{m}}$ **(Pa·min/lb)**	51.3	51.9	50.8	50.3

APPENDIX C

ERROR ANALYSIS

For single-phase and two-phase measurement, the experimental error originates from instrument measurement errors, including pressure transducers, flowmeters, and temperature sensors etc. For differential pressure measurement, the instrument accuracy is ±0.25%. Thus, the uncertainty for differential pressure measurement is around ±0.25%. Table C.1 lists all the instruments and their measurement accuracies.

Table C.1 Instrument specifications

Transducer	Model	Range	Accuracy
Coriolis liquid mass flowmeter	Micro Motion DS300	0 to 7000 lb/min	0.15%
Coriolis liquid density		0 to 5 Kg/m^3	0.05%
Coriolis liquid temperature		-400 to 400 °F	0.5%
Differential pressure transmitter	Emerson Rosemount 3051S	0 to 50 psig	0.1%

For viscosity calculation through PV, the error analysis should consider several factors since calculations need the pressure drop across the pipe and the volumetric flowrate which is composed of mass flowrate and density. Other factors such as absolute pressure and temperature do not affect viscosity measurement so they are not included. Equations (2.6) and (2.9) which are the derived viscosity for laminar and turbulent flows, respectively. Based on the error propagation theory, the error of viscosity (μ) or effective viscosity ($\mu_{effective}$) at the PV is calculated by

$$\frac{\delta\mu}{\mu} = \sqrt{\left(\frac{\delta\dot{m}}{\dot{m}}\right)^2 + \left(\frac{\delta\rho}{\rho}\right)^2 + \left(\frac{\delta\Delta P}{\Delta P}\right)^2} \qquad \text{(C.1)}$$

In the equations above, $\dot{m}$ is mass flowrate of liquid and ρ is the density which are

measured by Coriolis flowmeters while ΔP is the differential pressure across the PV which is measured by the transmitter. Substitute all the measurement errors listed in Table C.1 into Equation (C.1), one can obtain the final error of calculated μ is ±0.1871%.

Equation (2.22), which is the no slip mixture density, is used to back calculate the fraction of each phase. Since each phase density is a function of the sensor temperature,

$$\frac{\delta f_w}{f_w} = \sqrt{\left(\frac{\delta \rho_m}{\rho_m}\right)^2 + 2\left(\frac{\delta T}{T}\right)^2} \tag{C.2}$$

where ρ_m is the mixture density and T is the temperature measurements from the mass flowmeter. Substitute the corresponding measurement errors listed in Table C.1 into Equation (C.3), the final error of calculated f_w is ±0.71%.

CFD simulation errors contain modeling error and numerical error. Modeling errors, originated from mathematical representation of physical problem, are usually negligible in CFD simulation error analysis compared with numerical errors (Stern et al., 2011). In this study, the Richardson extrapolation (RE) is employed to analyze numerical error caused by coarse grids (Wilson et al., 2001).

Suppose coarse, medium and fine grids corresponding to numerical solutions: S_1, S_2 and S_3, respectively. Variances between medium-fine $\varepsilon_{21} = S_2 - S_1$, and coarse-medium $\varepsilon_{32} = S_3 - S_2$ are used to define the convergence ratio:

$$R = \frac{\varepsilon_{21}}{\varepsilon_{32}} \tag{C.3}$$

R corresponds to three different convergence conditions. $0 < R < 1$ is monotonic convergence condition. Simulation uncertainties can be analyzed by generalized RE. $R < 0$ is oscillatory convergence condition. The oscillation maximum/minimum boundary is adopted to quantify numerical errors. $R > 1$ corresponds to divergence, whose errors and uncertainties cannot be estimated. Based on RE, the numerical solution with the first n terms of series expansion can be

expressed as

$$S = S_C + \delta^* = S_C + \sum_{i=1}^{n} (\Delta x)^{P^{(i)}} g^{(i)} \quad \text{(C.4)}$$

where Δx is the thickness of grid layer, $P^{(i)}$ is the order of accuracy, and $g^{(i)}$ is series coefficient. For simplicity, $n = 1$ is analyzed in this study; thus, δ^* can be estimated by

$$p = \frac{\ln(\varepsilon_{32}/\varepsilon_{21})}{\ln(r)} \quad \text{(C.5)}$$

and $$\delta^* = \frac{\varepsilon_{21}}{r^P - 1} \quad , \quad \text{(C.6)}$$

where r is the ratio of grid layer thickness. To account for effects of higher-order terms and provide a quantitative metric to determine proximity of the solutions to the asymptotic range, the multiplication factor C is introduced:

$$\mathrm{C} = \frac{r^P - 1}{r^{Pest} - 1} \quad , \quad \text{(C.7)}$$

where p_{est} is an estimate for the limiting order of accuracy. C approaches 1 as spacing size goes to zero and asymptotic range is reached. Thus, the numerical uncertainty due to grid size can be obtained from

$$\delta_C^* = C\left(\frac{\varepsilon_{21}}{r^P - 1}\right). \quad \text{(C.8)}$$

From the mesh independence check in Chapter 3, an estimation of the numerical error by Equation (C.8) based on grid number of 62,755, 143,440 and 201,833 is below 3%. As mentioned above, the grids used in this study for performing CFD simulation contain more than 201,833 elements, which are sufficient to ensure the numerical accuracy.

APPENDIX D

DIMENSIONAL ANALYSIS

Emulsion rheology at the ESP stage is affected by at least these basic dimensional factors: volumetric flowrate (Q), interfacial tension (σ), viscosity (μ), density (ρ), ESP's frequency (f), and stage diameter (D). The table below shows the basic dimensions for each parameter:

Table D.1 Dimensional analysis variables

Variables	ρ	Q	D	μ	σ	f
Basic dimensions	$\frac{M}{L^3}$	$\frac{L^3}{T}$	L	$\frac{M}{L \cdot T}$	$\frac{M}{T^2}$	$\frac{1}{T}$

Now we have 6 variables with 3 basic dimensions. Therefore, we should derive 3 dimensionless groups. By selecting the first 3 variables from the table, namely ρ, ṁ, and D as the repeated variables in each group, we have:

$$\Pi_1 = \rho \left[\frac{M}{L^3}\right]^a Q \left[\frac{L^3}{T}\right]^b D[L]^c \mu \left[\frac{M}{L \cdot T}\right] = M^0 L^0 T^0 \quad \text{(D.1)}$$

$$\Pi_2 = \rho \left[\frac{M}{L^3}\right]^a Q \left[\frac{L^3}{T}\right]^b D[L]^c \sigma \left[\frac{M}{T^2}\right] = M^0 L^0 T^0 \quad \text{(D.2)}$$

$$\Pi_3 = \rho \left[\frac{M}{L^3}\right]^a Q \left[\frac{L^3}{T}\right]^b D[L]^c f \left[\frac{1}{T}\right] = M^0 L^0 T^0 \quad \text{(D.3)}$$

Solving for the exponents *a*, *b*, and *c* for each group yields a=-1, b=-1 and c=1 for Π_1, a=-1, b=-2 and c=3 for Π_2, a=0, b=-1 and c=3. Substituting these exponents to the equations yields:

$$\Pi_1 = \frac{D\mu}{\rho Q} = \frac{D\mu}{\rho v A} = \frac{D\mu}{\rho v D^2} = Re^{-1} \Rightarrow \frac{1}{\Pi_1} = Re \quad \text{(D.4)}$$

$$\Pi_2 = \frac{D^3\sigma}{\rho Q^2} = \frac{V\sigma}{\rho Q^2} = \frac{V\sigma}{\rho v^2 A^2} \cong \frac{\sigma}{\rho v^2 l} = We^{-1} \Rightarrow \frac{1}{\Pi_2} = We \quad \text{(D.5)}$$

$$\Pi_3 = \frac{D^3 f}{Q} = \frac{Vf}{Q} \cong \frac{lAf}{vA} = \frac{fl}{v} \Rightarrow \Pi_3 = St \quad \text{(D.6)}$$

Therefore, Reynolds number, Weber number, and Strouhal number are the dimensionless numbers considered in estimating the emulsion rheology at the ESP stage. Other factors affecting the emulsion rheology cannot be derived with this analysis since they are already dimensionless, such as the fraction of the dispersed phase and the stage number.